

UNIVERSIDADE DE SÃO PAULO  
ESCOLA DE ENGENHARIA DE SÃO CARLOS

**FELIPE RENDEIRO FLOR**

**Monitoramento do dano em estruturas de material compósito através de métodos baseados em vibrações: juntas coladas metal-compósito e estruturas sanduíche**

São Carlos  
2016



**FELIPE RENDEIRO FLOR**

**Monitoramento do dano em estruturas de material compósito através de métodos baseados em vibrações: juntas coladas metal-compósito e estruturas sanduíche**

Dissertação apresentada à Escola de Engenharia de São Carlos, da Universidade de São Paulo, como parte dos requisitos para obtenção do título de Mestre em Engenharia Mecânica.

Área de concentração: Aeronaves.

Orientador: Prof. Assoc. Volnei Tita

São Carlos  
2016

ESTE EXEMPLAR TRATA-SE  
DA VERSÃO CORRIGIDA.  
A VERSÃO ORIGINAL  
ENCONTRA-SE DISPONÍVEL  
JUNTO AO DEPARTAMENTO DE  
ENGENHARIA MECÂNICA DA  
EESC-SP.

AUTORIZO A REPRODUÇÃO TOTAL OU PARCIAL DESTE TRABALHO, POR QUALQUER MEIO CONVENCIONAL OU ELETRÔNICO, PARA FINS DE ESTUDO E PESQUISA, DESDE QUE CITADA A FONTE.

F632m Flor, Felipe Rendeiro  
Monitoramento do dano em estruturas de material compósito através de métodos baseados em vibrações: juntas coladas metal-compósito e estruturas sanduíche / Felipe Rendeiro Flor; orientador Volnei Tita. São Carlos, 2015.

Dissertação (Mestrado) - Programa de Pós-Graduação em Engenharia Mecânica e Área de Concentração em Aeronaves -- Escola de Engenharia de São Carlos da Universidade de São Paulo, 2015.

1. Monitoramento da integridade estrutural. 2. Estruturas inteligentes. 3. Juntas Coladas Metal-Compósito. 4. Estruturas Sanduíche. 5. Análise via Elementos Finitos. 6. Análise Experimental. I. Título.

## FOLHA DE JULGAMENTO

Candidato: Engenheiro **FELIPE RENDEIRO FLÔR**.

Título da dissertação: "Monitoramento do dano em estruturas de material compósito através de métodos baseados em vibrações: juntas coladas metal-compósito e estruturas sanduíche".

Data da defesa: 18/01/2016

### Comissão Julgadora:

Prof. Associado **Volnei Tita**  
**(Orientador)**  
(Escola de Engenharia de São Carlos/EESC)

Prof. Dr. **Sergio Henrique Evangelista**  
(Universidade Federal de São Carlos/UFSCar)

Prof. Dr. **Fred Nitzsche**  
(Carleton University)

### Resultado:

APROVADO

APROVADO

APROVADO

Coordenador do Programa de Pós-Graduação em Engenharia Mecânica:  
Prof. Associado **Gherhardt Ribatski**

Presidente da Comissão de Pós-Graduação:  
Prof. Associado **Paulo César Lima Segantine**



*"I dedicate this work to my dear  
Fernanda."*



## ACKNOWLEDGMENT

---

---

I would like to thank Professor Volnei Tita, for providing orientations that helped me beyond aspects of the research. None of this would be possible without his encouragement, guidance and sympathetic attitude. For that and much more, I'll always be thankful.

My gratitude also lies with Professor Fred Nietzsche for giving me the opportunity to work in his Rotorcraft Laboratory at Carleton University (Canada).

I'm thankful for Professor Marcelo Leite and other colleagues from USP, who were always available to answer my questions and offer suggestions.

I'm grateful for all the support my beloved girlfriend Fernanda has given me throughout the months I had to stay away due to the research.

Sincere thanks for my mom and dad, Ana and Genival, who are always by my side whenever I need. I have deep love and appreciation for both of them.

Lastly, deep thanks for the support of the National Council of Scientific and Technological Development (CNPq process number: 139806/2013-0), for funding this research.



## RESUMO

---

---

FLOR, F. R. Monitoramento do dano em estruturas de material compósito através de métodos baseados em vibrações: juntas coladas metal-compósito e estruturas sanduíche. 2016,120p. Dissertação (Mestrado) - Escola de Engenharia de São Carlos, Universidade de São Paulo, São Carlos, SP, Brasil, 2016.

Esta dissertação aborda os estudos realizados no campo de Sistemas de Monitoramento da Integridade Estrutural por meio de métodos baseados em vibrações. O tópico abordado é organizado em dois estudos paralelos. O primeiro é relativo ao monitoramento da integridade de juntas coladas metal-compósito. O segundo versa sobre análises semelhantes em estruturas sanduíche. O monitoramento foi executado através das análises das assinaturas dinâmicas das estruturas, tanto computacionalmente quanto experimentalmente, visando avaliar a capacidade de metodologias vibracionais de SHM em detectar dano de descolamento. As respostas dinâmicas foram obtidas por meio de acelerômetros e sensores piezelétricos dispostos sobre a superfície das estruturas avaliadas. Os acelerômetros fornecem dados de referência para as análises realizadas com base nas respostas do sensor piezelétrico. Diferentes métricas de identificação de dano são abordadas, sendo que todas estão baseadas em análise no domínio da frequência, utilizando parâmetros de magnitude ou ângulo de fase das estruturas danificadas e intactas. O presente trabalho propôs alterações em algumas das metodologias encontradas na literatura e comparou os resultados das métricas originais com as modificadas. As métricas modificadas apresentaram resultados mais consistentes em vários cenários de análise. Constatou-se também que as métricas abordadas mostram-se válidas para os casos observados no presente estudo. As análises experimentais também evidenciaram a influência na assinatura dinâmica da estrutura sanduíche causada pelo posicionamento de pequenos elementos elastoméricos. Com relação às análises via elementos finitos, os modelos computacionais apresentaram resultados similares aos obtidos experimentalmente, sendo os da junta colada os mais precisos. Tais modelos computacionais podem ser melhorados no futuro por meio de uma modelagem mais detalhada dos elementos piezelétricos (por exemplo: por meio de novas formulações), como também da região de descolamento (por exemplo: por meio da implementação de algoritmos de contato). Deve-se ressaltar também que as propriedades elásticas das lâminas externas da estrutura sanduíche foram obtidas da literatura, assim sendo, o modelo poderá ser melhorado em estudos futuros por meio do emprego de propriedades obtidas experimentalmente.

**Palavras-chave:** Monitoramento da Integridade Estrutural. Estruturas Inteligentes. Juntas Coladas Metal-Compósito. Estruturas Sanduíche. Análise via Elementos Finitos. Análise Experimental.



## ABSTRACT

---

---

FLOR, F. R. *Damage monitoring in composite structures via vibration based method: metal-composite bonded joints and sandwich structures*. 2016,120p. Dissertation (Master of Science) - São Carlos School of Engineering , University of São Paulo, São Carlos, SP, Brazil, 2016

The present document covers the studies over Structural Health Monitoring systems via vibration based methods. The topic is organized in two parallel studies. The first one analyzes the integrity of metal-composite single lap bonded joints. The second one approaches similar analyses for sandwich structures. The monitoring was made by investigating the dynamic response both computationally and experimentally to verify the reliability of applying vibration based SHM procedures, specifically with the objective of identifying the presence of debonding damage. The dynamic responses were obtained via accelerometers and piezoelectric sensors placed on top of the investigated structures (on the outward surface). The purpose for the accelerometers is to provide reference data for the analyses involving the piezoelectric sensors. Different metrics of damage identification were investigated, all working over a determined frequency range. They quantify the damage by analyzing either the magnitudes or phase angles of the dynamic responses among the undamaged and damage structures. This present work proposed modifications to some methodologies of damage quantification found in the literature and compared the results. The new metrics offered more reliable values for the damage quantification on several of the analyses. It was verified that the metrics are valid for the scenarios observed in the present study. The experimental analyses showed also the influence on the dynamic response due to the position of small elastomeric elements. In regards to the finite element analyses, the computational models showed similar results to the experimental data, the more accurate ones being the models for the bonded joints. For the computational models, improvements can be applied into the piezoelectric sensor (e.g. by using new finite element formulations), as well as the region of debonding (e.g. by using contact algorithms). It is important to highlight that the elastic properties of the skins for the sandwich structure were obtained by the literature, so the model can be improved in the future by applying properties obtained experimentally.

**Keywords:** Structural Health Monitoring. Smart structures. Metal-Composite Joints, Sandwich Structures. Finite Element Analysis. Experimental Analysis.



## LIST OF FIGURES

---



---

<i>Figure 1. Laminate coordinates.</i> _____	38
<i>Figure 2. 3D stress state.</i> _____	38
<i>Figure 3. Membrane Loadings [N], Shear Forces [Q] and Moments [M] actuating in the laminate.</i> _____	42
<i>Figure 4. Metal-composite bonded joint specimens.</i> _____	48
<i>Figure 5. Experimental set-up for the free-free condition.</i> _____	51
<i>Figure 6. Experimental set-up for biclamped condition.</i> _____	52
<i>Figure 7. Disposition of (output) sensors and input point for the specimens.</i> _____	53
<i>Figure 8. Mickens Damage Quantification (Magnitude) - Bonded Joint – Free-Free - S1P0[A2] vs. S2P0[A2] (Low value divisions)</i> _____	56
<i>Figure 9. Mickens Damage Quantification (Magnitude) - Bonded Joint – Free-Free - S1P0[A2] vs. S2P0[A2]. (Tendentious contributions)</i> _____	56
<i>Figure 10. Mickens Damage Quantification (Phase) - Bonded Joint – Free-Free - S1P0[A2] vs. S2P0[A2].</i> _____	57
<i>Figure 11. Filtering of specific frequency ranges of the Data</i> _____	58
<i>Figure 12. Modified Damage Quantification (Magnitude) - Bonded Joint – Free-Free - S1P0[A2] vs. S2P0[A2].</i> _____	58
<i>Figure 13. Modified Damage Quantification (Phase) - Bonded Joint – Free-Free - S1P0[A2] vs. S2P0[A2].</i> _____	59
<i>Figure 14. Finite Element model for the undamaged bonded joint without Piezoelectric Element (S1P0)/</i> _____	61
<i>Figure 15. Finite Element model for the damaged joint without the Piezoelectric Element (S2P0).</i> _____	61
<i>Figure 16. Boundary conditions and prescribed displacement for the biclamped model.</i> _____	62
<i>Figure 17. Finite Element model for the damaged joint with Piezoelectric Element (S2P1).</i> _____	62
<i>Figure 18. Step procedures for the numerical Modal Analysis via ABAQUS™ v6.12.</i> _____	64
<i>Figure 19. The first non-rigid mode shapes for the undamaged bonded joint - free-free.</i> _____	67
<i>Figure 20. Experimental: Influence of the PZT sensor - Bonded Joint – free-free - A1.</i> _____	68
<i>Figure 21. Computational: Influence of the PZT sensor - Bonded Joint - free-free - A1.</i> _____	68
<i>Figure 22. Experimental: Influence of the PZT sensor - Bonded Joint - free-free - A2.</i> _____	69
<i>Figure 23. Computational: Influence of the PZT sensor - Bonded Joint - free-free - A2.</i> _____	69
<i>Figure 24. Comparison: Computational vs. Experimental FRF <math>H_{12}</math> S1P0 (free-free condition).</i> _____	70
<i>Figure 25. Comparison: Computational vs. Experimental FRF <math>H_{12}</math> S1P1 (free-free condition).</i> _____	70
<i>Figure 26. 1st Flexural Modal Shape: Undamaged vs. Damaged.</i> _____	71
<i>Figure 27. 2nd Flexural Modal Shape: Undamaged vs. Damaged.</i> _____	72
<i>Figure 28. 3rd Flexural Modal Shape: Undamaged vs. Damaged.</i> _____	72
<i>Figure 29. 4th Flexural Modal Shape: Undamaged vs. Damaged.</i> _____	72
<i>Figure 30. Experimental: Influence of Debonding Damage - Bonded Joint - free-free - A1.</i> _____	73
<i>Figure 31. Computational: Influence of Debonding Damage - Bonded Joint - free-free - A1.</i> _____	73

Figure 32. Experimental: Influence of Debonding Damage - Bonded Joint - free-free - A2.	74
Figure 33. Computational: Influence of Debonding Damage - Bonded Joint - free-free - A2.	74
Figure 34. Experimental: Influence of the Damage - Bonded Joint - free-free - P1.	76
Figure 35. Computational: Influence of the Damage - Bonded Joint - free-free - P1.	76
Figure 36. Comparison: Computational vs. Experimental FRF $H_{14}$ S1P1 ( free-free condition).	78
Figure 37. Comparison: Computational vs. Experimental FRF $H_{14}$ S2P1 (free-free condition).	79
Figure 38. The first non-rigid mode shapes for the undamaged bonded joint - biclamped.	81
Figure 39. Experimental: Influence of the PZT sensor - Bonded Joint - biclamped - A1.	82
Figure 40. Computational: Influence of the PZT sensor - Bonded Joint - biclamped - A1.	82
Figure 41. Experimental: Influence of the PZT sensor - Bonded Joint - biclamped - A2.	83
Figure 42. Computational: Influence of the PZT sensor - Bonded Joint - biclamped - A2.	83
Figure 43. Experimental: Influence of Damage - Bonded Joint - biclamped - A1.	84
Figure 44. Computational: Influence of Damage - Bonded Joint - biclamped - A1.	84
Figure 45. Experimental: Influence of Damage - Bonded Joint - biclamped - A2.	85
Figure 46. Computational: Influence of Damage - Bonded Joint - biclamped - A2.	85
Figure 47. Experimental: Influence of the Damage - Bonded Joint - biclamped - P1.	87
Figure 48. Computational: Influence of the Damage - Bonded Joint - biclamped - P1.	87
Figure 49. Comparison: Computational vs. Experimental FRF $H_{14}$ S1P1 (biclamped condition).	89
Figure 50. Comparison: Computational vs. Experimental FRF $H_{14}$ S2P1 (biclamped condition).	90
Figure 51. Sandwich structure specimens.	94
Figure 52. Lay-up of dry fibers for the Skins of the Sandwich Structure.	95
Figure 53. Manufacturing process of the Skins	96
Figure 54. Fabrication Process of the Sandwich Structure	98
Figure 55. Experimental set-up for the free-free condition of sandwich structures.	99
Figure 56. Details of the experimental set-up for free-free condition of sandwich structure: input and output points.	100
Figure 57. Finite Element model for the sandwich structure S2P2.	102
Figure 58. First non-rigid modal shapes for the undamaged sandwich structure.	104
Figure 59. Experimental: Influence of the PZT sensor – Sandwich Structure - A3.	105
Figure 60. Computational: Influence of the PZT sensor - Sandwich Structure - A3.	106
Figure 61. Comparison: Computational vs. Experimental FRF $H_{14}$ S1P2 (Sandwich Structure).	106
Figure 62. Comparison: Computational vs. Experimental FRF $H_{14}$ S1P2 (Sandwich Structure).	107
Figure 63. Experimental: Influence of Debonding Damage - Sandwich Structure - A1 and A2.	107
Figure 64. Computational: Influence of Debonding Damage - Sandwich Structure - A1 and A2.	108
Figure 65. Experimental: Influence of Debonding Damage - Sandwich Structure - A3.	108
Figure 66. Computational: Influence of Debonding Damage - Sandwich Structure- A3.	109
Figure 67. Experimental: Influence of the Damage - Sandwich Structure - P1 and P2.	110
Figure 68. Computational: Influence of the Damage - Sandwich Structure - P1 and P2.	110

<i>Figure 69. Comparison: Computational vs. Experimental FRF <math>H_{13}</math> SIP2 (Sandwich Structure).</i>	111
<i>Figure 70. Comparison: Computational vs. Experimental FRF <math>H_{13}</math> S2P2 (Sandwich Structure).</i>	111
<i>Figure 71. Test set-up of undamaged sandwich structure including elastomeric patches.</i>	124
<i>Figure 72. Elastomeric patches influence – measurements by Accelerometer 1 (Specimen SIP0).</i>	125
<i>Figure 73. Elastomeric patches influence – measurements by Accelerometer 2 (Specimen SIP0).</i>	126
<i>Figure 74. Elastomeric patches influence – measurements by Accelerometer 3 (Specimen SIP0).</i>	126



## LIST OF TABLES

<i>Table 1. CFRP properties.</i>	49
<i>Table 2. Titanium Alloy - Ti6Al4V – properties.</i>	49
<i>Table 3. Adhesive's properties.</i>	49
<i>Table 4. Piezoelectric sensor properties (Mide QP10n).</i>	50
<i>Table 5. Specimen identification.</i>	50
<i>Table 6. Critical Damping Factors for SIP0 – free-free.</i>	65
<i>Table 7. Critical Damping Factors for S2P0 – free-free.</i>	65
<i>Table 8. Critical Damping Factors for SIP1 – free-free.</i>	65
<i>Table 9. Critical Damping Factors for S2P1 – free-free.</i>	65
<i>Table 10. Modal Analysis for bonded joints – Numerical natural frequencies of SIP0 – free-free.</i>	66
<i>Table 11. Comparison: Computational vs. Experimental FRF <math>H_{12}</math> – free-free.</i>	71
<i>Table 12. Mickens Damage Factors for Specimens without PZT - Bonded Joint - free-free.</i>	75
<i>Table 13. Modified Damage Factors for Specimens without PZT - Bonded Joint - free-free.</i>	75
<i>Table 14. Mickens Damage Factors for Specimens with PZT - Bonded Joint - free-free.</i>	77
<i>Table 15. Modified Damage Factors for Specimens with PZT - Bonded Joint - free-free.</i>	77
<i>Table 16. Relative Difference between Damage Factors - free-free – Mickens.</i>	78
<i>Table 17. Relative Difference between Damage Factors - free-free – Modified.</i>	78
<i>Table 18. Critical Damping Factors for Specimen 1 – biclamped.</i>	79
<i>Table 19. Critical Damping Factors for Specimen 2 – biclamped.</i>	80
<i>Table 20. Critical Damping Factors for Specimen 3 – biclamped.</i>	80
<i>Table 21. Critical Damping Factors for Specimen 4 – biclamped.</i>	80
<i>Table 22. Modal Analysis for bonded joints - Numerical Modal frequencies for SIP0 - biclamped.</i>	81
<i>Table 23. Comparison: Computational vs. Experimental FRF <math>H_{13}</math> – biclamped.</i>	81
<i>Table 24. Mickens Damage Factors for specimens without PZT - Bonded Joint – biclamped.</i>	86
<i>Table 25. Modified Damage Factors for specimens without PZT - Bonded Joint – biclamped.</i>	86
<i>Table 26. Mickens Damage Factors for Specimens with PZT - Bonded Joint – biclamped.</i>	88
<i>Table 27. Modified Damage Factors for Specimens with PZT - Bonded Joint – biclamped.</i>	88
<i>Table 28. Relative Difference between Damage Factors - biclamped – Mickens.</i>	88
<i>Table 29. Relative Difference between Damage Factors - biclamped – Modified.</i>	89
<i>Table 30. Skin properties.</i>	96
<i>Table 31. PVC foam core elastic properties.</i>	97
<i>Table 32. Piezoelectric sensor properties (M2814-P1).</i>	98
<i>Table 33. Critical Damping Factors for SIP0 – Sandwich Structure.</i>	103

---

<i>Table 34. Critical Damping Factors for SIP1 – Sandwich Structure.</i>	<u>103</u>
<i>Table 35. Critical Damping Factors for SIP2 – Sandwich Structure.</i>	<u>103</u>
<i>Table 36. Critical Damping Factors for S2P0 – Sandwich Structure.</i>	<u>103</u>
<i>Table 37. Critical Damping Factors for S2P1 – Sandwich Structure.</i>	<u>103</u>
<i>Table 38. Critical Damping Factors for S2P2 – Sandwich Structure.</i>	<u>103</u>
<i>Table 39. Modal Analysis for Sandwich Structures - Numerical natural frequencies for specimen SIP0.</i>	<u>104</u>
<i>Table 40. Mickens Damage Factors for the Sandwich Structure.</i>	<u>112</u>
<i>Table 41. Modified Damage Factors for the Sandwich Structure.</i>	<u>112</u>
<i>Table 42. Specimen ID considering the orientation of elastomeric patch.</i>	<u>125</u>

## LIST OF ACRONYMS AND ABBREVIATIONS

---

---

ASTM	American Society for Testing and Materials
CFRP	Composite Fiber Reinforced Polymer
DOF	Degree of Freedom
FEA	Finite Element Analysis
FEm	Finite Element Model
FFT	Fast Fourier Transform
FRF	Frequency Response Function
GEA	Group of Aeronautical Structures
MFC	Macro Fiber Composite
MIL-HDBK	Military Handbook
NDI	Non-Destructive Inspection
PVC	Polyvinyl Chloride
PZT	Lead-Zirkonate-Titanate
SHM	Structural Health Monitoring
UEL	User Element Subroutine (ABAQUS)
USP	University of São Paulo



## LIST OF SYMBOLS

---



---

$E_{11}$	Young's modulus in longitudinal direction (fiber direction)	$N/m^2$
$E_{22}$	Young's modulus in transverse direction over the axis 2 (normal to fiber)	$N/m^2$
$G_{12}$	Shear modulus in ply plane	$N/m^2$
$\nu_{12}$	Poisson's ratio in ply plane	-
$X_T$	Longitudinal direction tensile strength	-
$X_c$	Longitudinal direction compressive strength	-
$Y_T$	Transverse direction tensile strength	-
$Y_c$	Transverse direction compressive strength	-
$S_{12}$	Shear strength value in ply plane	Pa
$S_{23}$	Shear strength value out of plane	Pa
$c_{33}$	Modulus of elasticity in the longitudinal direction (Piezoelectric Equations)	Pa
$e_{33}$	Piezoelectric Coupling Coefficient in the longitudinal direction	$C/m^2$
$\epsilon_{33}$	Dielectric Constant in the longitudinal direction (Piezoelectric Equations)	$nF/m$
$\rho$	Density	$Kg/m^3$
$H_{12}$	Frequency Response Function's Magnitude; Input on point 1, Output on point 2	
$H^i$	Magnitude for Undamaged Model	
$H^d$	Magnitude for Damaged Model	

$f_1$	Starting frequency for the Damage Factor calculation	Hz
$f_2$	Ending frequency for the Damage Factor calculation	Hz
$\Delta f$	Frequency increment for Damage Factor calculation	Hz
V	Voltage	V

# TABLE OF CONTENTS

---

---

<b>ACKNOWLEDGMENT</b>	<b>IX</b>
<b>RESUMO</b>	<b>XI</b>
<b>ABSTRACT</b>	<b>XIII</b>
<b>LIST OF FIGURES</b>	<b>XV</b>
<b>LIST OF TABLES</b>	<b>XIX</b>
<b>LIST OF ACRONYMS AND ABBREVIATIONS</b>	<b>XXI</b>
<b>LIST OF SYMBOLS</b>	<b>XXIII</b>
<b>TABLE OF CONTENTS</b>	<b>XXV</b>
<b>1. INTRODUCTION</b>	<b>29</b>
1.1. GENERAL OBJECTIVES	31
1.2. ORGANIZATION OF CHAPTERS	31
<b>2. THEORETICAL BASIS</b>	<b>33</b>
2.1. STRUCTURAL DYNAMICS	33
2.2. COMPOSITE STRUCTURES	37
<b>3. SHM FOR METAL-COMPOSITE JOINTS</b>	<b>45</b>
3.2. REVIEW	45
3.3. SPECIFIC OBJECTIVES	46

---

<b>3.4. EXPERIMENTS</b>	<b>47</b>
3.4.1. MATERIALS AND SPECIMENS	47
3.4.2. EXPERIMENTAL SET-UPS AND INSTRUMENTATION	51
3.4.3. EXPERIMENTAL PROCEDURES	53
3.4.4. DAMAGE METRICS	54
3.4.5. PROPOSED DAMAGE METRICS	55
<b>3.5. FINITE ELEMENT ANALYSIS</b>	<b>59</b>
<b>3.6. RESULTS</b>	<b>64</b>
3.6.1. FREE-FREE BOUNDARY CONDITION	64
3.6.1.1. CASE STUDY 1: INFLUENCE OF THE PZT SENSOR	67
3.6.1.2. CASE STUDY 2: INFLUENCE OF THE DAMAGE	71
3.6.1.3. CASE STUDY 3: DAMAGE IDENTIFICATION	75
3.6.2. BICLAMPED BOUNDARY CONDITION	79
3.6.2.1. CASE STUDY 1: INFLUENCE OF THE PZT SENSOR	82
3.6.2.2. CASE STUDY 2: INFLUENCE OF THE DAMAGE	84
3.6.2.3. CASE STUDY 3: DAMAGE IDENTIFICATION	86
<b>3.7. CONSIDERATIONS</b>	<b>90</b>
<b><u>4. SHM FOR SANDWICH STRUCTURES</u></b>	<b><u>91</u></b>
<b>4.2. REVIEW</b>	<b>91</b>
<b>4.3. SPECIFIC OBJECTIVES</b>	<b>92</b>
<b>4.4. EXPERIMENTS</b>	<b>94</b>
4.4.1. MATERIALS AND SPECIMENS	94
4.4.2. EXPERIMENTAL SET-UPS AND INSTRUMENTATION	99
4.4.3. EXPERIMENTAL PROCEDURES	100
<b>4.5. FINITE ELEMENT ANALYSIS</b>	<b>101</b>
<b>4.6. RESULTS</b>	<b>102</b>
4.6.1. CASE STUDY 1: INFLUENCE OF THE PZT SENSOR	105
4.6.2. CASE STUDY 2: INFLUENCE OF THE DAMAGE	107
4.6.3. CASE STUDY 3: DAMAGE IDENTIFICATION	109
<b>4.7. CONSIDERATIONS</b>	<b>113</b>
<b><u>5. CONCLUSION AND FUTURE PERSPECTIVES</u></b>	<b><u>115</u></b>

---

<b>5.1. METAL-COMPOSITE BONDED JOINT</b>	<b>115</b>
<b>5.2. SANDWICH STRUCTURE</b>	<b>116</b>
<b>6. REFERENCES</b>	<b>117</b>
<hr/>	
<b>7. ATTACHMENTS</b>	<b>121</b>
<b>7.1. ATTACHMENT 1 - RELATED PUBLICATIONS</b>	<b>121</b>
<b>7.2. ATTACHMENT 2 - PYTHON CODE OF THE METRICS</b>	<b>122</b>
<b>7.3. ATTACHMENT 3 – ELASTOMER INFLUENCE</b>	<b>124</b>



# 1. INTRODUCTION

---

---

The aeronautical industry has intensified the use of composite materials on its structures over the latest decades. This change is justified by several reasons, for example, when compared to metallic alloys, composite materials have lower density, greater corrosion resistance and higher potential of designing specific properties according to the application purposes.

However, composite materials present a complex behavior of failure, which can also be hard to detect depending on the placement of the damage. Traditional non-destructive inspection procedures currently used are either visual, which is often unreliable, or specific experimental methods such as ultrasonic, eddy-current and thermography (Guyott et al, 1986), which may require extended downtime, are expensive and have limited applicability. Alternatively, the integrity of composite structures can be monitored via Structural Health Monitoring (SHM) systems.

According to Hall (1999), Structural Health Monitoring consists in the acquisition, validation and analysis of technical data to facilitate life-cycle management decisions. Hafiychuk et al (2011) stated that among the most commonly used SHM methodologies, there is the Vibration Based Method (VBM), which allows constant real-time monitoring of structures with considerable reliability and low cost. VBM for Structural Health Monitoring is commonly divided into two categories: the traditional-methods and the modern-methods. The traditional-methods are the most commonly used and are usually simpler to implement. They rely on dynamic structural characteristics of the structure, such as mode shapes, modal damping and natural frequencies to perform the diagnosis. The modern methods apply different criteria such as Curvature Mode Shapes (which are calculated based on the second derivative of the displacement field of the mode shapes), Wavelet Analysis and Neural Networks to perform the diagnosis. On the topic of modern methodologies of VBM for Structural Health Monitoring, a growing branch started when Pandey et. al (1991) proposed the use of a new parameter entitled Curvature Mode Shape to detect damage, as opposed to the traditional methods of analyzing frequency shifts and damping. In that study, the researchers demonstrated the technique by detecting crack damage on a cantilever beam. Hamley et al. (2004) applied the curvature mode shape technique to identify damage on

carbon/epoxy composite beams, the authors used smart piezoelectric sensors bonded to the surface of the beam as actuators and sensors, and alternatively input signal via impulse hammer was also used for comparing the data. The authors concluded that the methodology was limited and inconclusive for detecting delamination damage. It is also relevant to mention that Curvature Mode Shape requires multiple sensors positioned throughout the length of the structure, or a single sensor, which moves along the structure. Since weight is a key factor in the aeronautical industry, it was decided in this work to focus on a more simplistic and traditional approach for damage identification, which is based on the FRFs (Frequency Response Functions) with the aid of metrics for damage quantification.

One part of the present Master's Dissertation approaches bonded joints, which is one of the possible ways for assembling structural components. Among different methods, the most common are fastened or bonded joints. The potential of generating smooth surfaces makes the bonded joints an attractive alternative for the aeronautical industry, as well as other benefits such as weight reduction and the homogeneous distribution of stress (Higgins, 2000). This is opposed to the concentrated distribution present in fastened joints, which accelerate failure under fatigue. However, the proper integrity of these bonded joints is often critical for the aeronautical industry. Considering that reason, the academy has performed studies on the topic of Structural Health Monitoring of bonded joints, but investigations in this field are still scarce, even rarer on the subject of metal-composite bonded joints, which are investigated in the present manuscript.

Another part of the present Master's Dissertation approaches sandwich structures. Mendonça (2005) describes those structures as the assembly of two or more materials at macroscopic scale to work as a unity with the purpose to obtain mechanical properties apart from the ones of either material. It must be highlighted that the literature is still short on studies regarding SHM on sandwich structures, mainly with PVC foam core (Dawood et al, 2003). Therefore, the present Master's Dissertation collaborates in the expansion of the research over a lacking field of study.

## 1.1. GENERAL OBJECTIVES

The present work approaches the applicability of Vibration Based Method for SHM over two common arranges for composite materials in the aeronautical industry: Metal-composite bonded joints and sandwich structures. The analyses also compares different metrics of damage quantification and proposes modifications for the purpose of stabilizing the results. This is a continuation of previous studies performed by the Group of Aeronautical Structures of the University of São Paulo, which will be mentioned in more details in this manuscript.

To achieve this purpose, experimental data of vibration tests are confronted to computational analyses results for two different boundary conditions: free-free and/or biclamped. The dynamic behavior of the structures is analyzed via the dynamic signature of piezoelectric sensors and accelerometers placed on the specimens. The change of the dynamic behavior of the composite structures is captured by the sensors, characterizing the presence of damage. Therefore, it is used the Frequency Response Function (FRF) of the piezoelectric sensors combined to metrics for damage identification in order to obtain a reliable diagnostic of the structural integrity. Moreover, the study also proposes modifications to existing metrics of damage quantification seeking more stable results for the conditions analyzed.

## 1.2. ORGANIZATION OF CHAPTERS

This Master's Dissertation consists of eight chapters, organized as follows:

- ☑ **Chapter 1 – Introduction:** this chapter offers a quick insight on the purposes of the study, motivations and current developments of the academy on the SHM, giving a focus on the topics of metal-composite bonded joints and sandwich structures.
- ☑ **Chapter 2 – Theoretical Basis:** this chapter portrays briefly theoretical fundamentals of topics covered in this work. The Literature Review of this work has been distributed along the chapters. This chapter covers the reviews pertained to the general aspects related to this work, which are structural dynamics and composite structures.
- ☑ **Chapter 3 – SHM for Metal-Composite Joints:** this chapter contains an introduction and literature review, objectives, methodologies, results and conclusions on the topics of SHM for metal-composite bonded joints.

- ☑ **Chapter 4 – SHM for Sandwich Structures:** similarly to the format adopted on Chapter 3, this chapter approaches on sandwich structures. Proposals of future experimental procedures and computational analyses are also discussed.
- ☑ **Chapter 5 – Conclusions and Future Perspectives:** considerations related to the methodologies and results are presented in this chapter. Offering a summary of the work and overall observations.
- ☑ **Chapter 6 – References:** Scientific publications, which aided the development of the present work.
- ☑ **Attachments:**
  - Attachment 1 - List of publications related to the present work.
  - Attachment 2 - Python Code of the metrics used
  - Attachment 3 - Elastomer Influence

## 2. THEORETICAL BASIS

---

---

### 2.1. STRUCTURAL DYNAMICS

The damage quantification analyses used in this work are all based on the dynamic signature of the structures. For that reason, it is important to introduce the concepts of Frequency Response Functions, Damped Natural Frequencies, Stiffness and Damping.

Rao (1995) states that the vibration of a system involves the exchange of potential energy into kinetic energy and vice-versa whilst, in the case of damped systems, energy is dissipated at each cycle of vibration.

The study of vibration is classified in two categories. Free Vibration happens when the system is left to vibrate on its own after an initial disturbance, while Forced Vibration happens when the system is under the influence of an external force.

Natural Frequency, according to Rao (1995), can be understood as the frequency in which a system oscillates after being subjected to an initial disturbance and left to vibrate on its own.

A Frequency Response Function consists in a response model defined by the quotient between the Output function and the Input function for a given system.

As explained by Ewins (2000), the simplest form of a dynamic system consists of a concentrated point of mass ( $m$ ) that is connected to a stationary reference by elements with mass ( $m$ ) and stiffness ( $k$ ) under free vibration. The motion of this system can be expressed by the Newton's second law:

$$m\ddot{x} + kx = 0 \tag{1}$$

The trial solution  $x(t) = Xe^{i\omega t}$  for the displacement will only be satisfied if:

$$k - \omega^2 m = 0 \quad (2)$$

This shows that the natural frequency for this single mode of vibration system is:

$$\omega = \sqrt{\frac{k}{m}} \quad (3)$$

An increase in stiffness, therefore, will increase the natural frequency. Hence, if the structure becomes stiffer, then it will oscillate in a faster rate once the system gets excited. However, if the structure has damage, then it becomes “softer” and it will oscillate in a slower rate. This is the principle that it will be used in the present work.

Considering an excitation of the form:

$$f(t) = F e^{i\omega t} \quad (4)$$

The Frequency Response Function of this system can be written as:

$$H(\omega) = \frac{X}{F} = \frac{1}{k - \omega^2 m} \quad (5)$$

However, for a real structure, sometimes, it is necessary to consider damping effects. Thus, it is important to comment briefly about damped natural frequency, as well. To consider the effect of damping, the equation of motion for the system should now be written as:

$$m\ddot{x} + c\dot{x} + kx = 0 \quad (6)$$

For this, a more general solution must be used, in which "s" is a complex term:

$$x(t) = X e^{st} \quad (7)$$

For this solution requires the following condition to be valid. .

$$ms^2 + cs + k = 0 \quad (8)$$

This results in the solutions:

$$s_{1,2} = -\frac{c}{2m} \pm \frac{\sqrt{c^2 - 4km}}{2m} \quad (9)$$

Which may be re-written as:

$$s_{1,2} = -\omega_0\xi \pm i\omega_0\sqrt{1 - \xi^2} \quad (10)$$

$$\omega_0 = \sqrt{\frac{k}{m}} \quad (11)$$

$$\xi = \frac{c}{2\sqrt{km}} \quad (12)$$

The damping factor ( $\xi$ ) is a means of energy loss for the system. The effects of it in the dynamic signature are a gradual reduction of the magnitudes over the frequency and a reduction of the natural frequencies. The damped natural frequency of a single degree system is presented as function of  $\omega_n$ :

$$\omega_d = \omega_n\sqrt{1 - \xi^2} \quad (13)$$

A system with one degree of freedom has only one natural frequency, but more complex systems (like used in this work) have several natural frequencies, which are linked to respective vibration modes.

A non-damped free-free vibration with multiple degrees of freedom follows a similar equation to the case of single degree of freedom, but now, the values of mass, stiffness and damping are not scalar. In the Eq. (14), it is possible to observe the equation of motion for undamped system with multiple degrees of freedoms.

$$[M] * \{\ddot{u}\} + [K] * \{u\} = \{0\} \quad (14)$$

A valid solution to this differential equation is:

$$\{u\} = \{\phi\}e^{st} ; \{\ddot{u}\} = s^2\{\phi\}e^{st} \quad (15)$$

By placing the solution into the equation reveals a case of Eigenvalues ( $\lambda$ ) and Eigenvectors ( $\phi$ ) problem. That is true because  $e^{st}$  can never be equal to zero.

$$([K] - \lambda_n[M])\{\phi_n\} = \{0\} \quad (16)$$

$(\phi)_n$  represents an Eigenvector for the n-vibration mode and  $(\lambda)_n$  represents the respective Eigenvalue

The information of natural frequency is contained in the Eigenvalue. And, the natural frequency for the n-vibration mode of the structure is given by:

$$\omega_n = \sqrt{\lambda_n} \quad (17)$$

Therefore, a damaged structure will show dynamic behavior different than undamaged one. And, to monitor this, the present work uses piezoelectric sensors, so the equations above can be rewritten, introducing the piezoelectric effects. Besides, the influence of the piezoelectric sensor in the stiffness, damping and mass matrix can be considered. However, this can be found in details in Sartorato (2013a).

## 2.2. COMPOSITE STRUCTURES

This work investigated damaged and undamaged composite structures. The first one was bonded-joints of a composite beam linked to a titanium alloy beam. The second one was sandwich structures. Both of these are composite structures commonly used in the aeronautical industry.

According to Callister (2002), a composite material is a combination of other materials that maintains the identity of each material involved, but forms a structure, which gathers better mechanical properties of each component (material) or even suppresses the disadvantages of each one. It is important to highlight that there are different ways for classifying composite materials, such as reinforced by long or short fibers, laminate or single ply and others. In this work, it was investigated laminates, which are composed by stacked layers with different orientations of long fibers. It is possible to calculate the mechanical properties of the layers via micromechanical models, considering some simplifications shown below:

- The layers are linear elastic.
- The fibers of a layer are identical and parallel.
- The matrix is homogeneous, isotropic and linear elastic.
- The bonding between the matrix and the fibers is perfect.

However, the influence of manufacturing process is relevant on the mechanical properties of composite materials. Therefore, it is recommended to perform mechanical testing by using standard methods in order to determine the values of the mechanical properties. Based on these values and on the orientations of fibers in each layer, the stiffness of a laminate, which is very import for the determination of the natural frequencies of the structure, can be calculated for a given coordinate system as shown in Figure 1 (Tita, 2006).

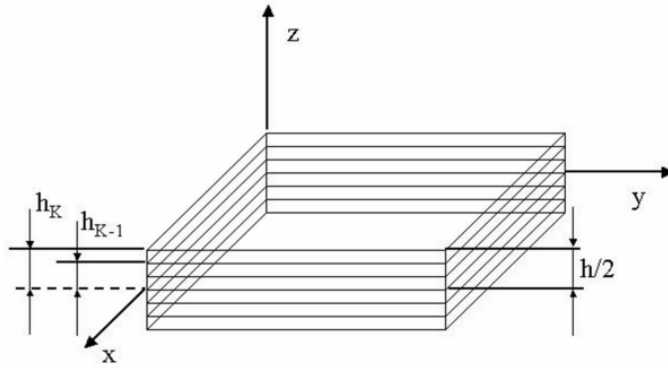


Figure 1. Laminate coordinates.

Considering the 3D stress state represented in Figure 2, it is possible to write the Stress Tensor shown by Eq. (18).

$$\sigma = \begin{bmatrix} \sigma_{xx} & \sigma_{xy} & \sigma_{xz} \\ \sigma_{yx} & \sigma_{yy} & \sigma_{yz} \\ \sigma_{zx} & \sigma_{zy} & \sigma_{zz} \end{bmatrix} \quad (18)$$

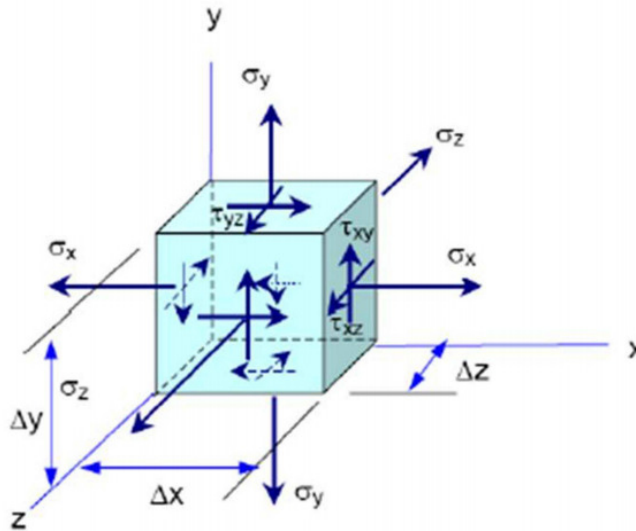


Figure 2. 3D stress state.

Since the body must be in equilibrium, it is possible to conclude that the stress tensor from Eq. (18) is symmetrical. Thus, the Stress Tensor can be written as shown by Eq. (19) and the Stain Tensor as shown by Eq. (14).

$$\sigma = \begin{bmatrix} \sigma_{xx} \\ \sigma_{yy} \\ \sigma_{zz} \\ \sigma_{yz} \\ \sigma_{zx} \\ \sigma_{xy} \end{bmatrix} = \begin{bmatrix} \sigma_{11} \\ \sigma_{22} \\ \sigma_{33} \\ \sigma_{23} \\ \sigma_{13} \\ \sigma_{12} \end{bmatrix} = \begin{bmatrix} \sigma_1 \\ \sigma_2 \\ \sigma_3 \\ \sigma_4 \\ \sigma_5 \\ \sigma_6 \end{bmatrix} \quad (19)$$

$$\epsilon = \begin{bmatrix} \epsilon_{xx} \\ \epsilon_{yy} \\ \epsilon_{zz} \\ \frac{\gamma_{yz}}{2} \\ \frac{\gamma_{zx}}{2} \\ \frac{\gamma_{xy}}{2} \end{bmatrix} = \begin{bmatrix} \epsilon_1 \\ \epsilon_2 \\ \epsilon_3 \\ \gamma_4 \\ \gamma_5 \\ \gamma_6 \end{bmatrix} \quad (20)$$

Strain and stress state can be related by the constitutive equation shown in Eq.(21).

$$\begin{bmatrix} \sigma_1 \\ \sigma_2 \\ \sigma_3 \\ \sigma_4 \\ \sigma_5 \\ \sigma_6 \end{bmatrix} = \begin{bmatrix} C_{11} & C_{12} & C_{13} & C_{14} & C_{15} & C_{16} \\ C_{21} & C_{22} & C_{23} & C_{24} & C_{25} & C_{26} \\ C_{31} & C_{32} & C_{33} & C_{34} & C_{35} & C_{36} \\ C_{41} & C_{42} & C_{43} & C_{44} & C_{45} & C_{46} \\ C_{51} & C_{52} & C_{53} & C_{54} & C_{55} & C_{56} \\ C_{61} & C_{62} & C_{63} & C_{64} & C_{65} & C_{66} \end{bmatrix} \begin{bmatrix} \epsilon_1 \\ \epsilon_2 \\ \epsilon_3 \\ \gamma_4 \\ \gamma_5 \\ \gamma_6 \end{bmatrix} \quad (21)$$

Considering that the layer can be simplified as an orthotropic material, some terms of the constitutive matrix [C] can be equal to zero, because there is not coupling between normal stresses and shear strains.

$$\begin{bmatrix} \sigma_1 \\ \sigma_2 \\ \sigma_3 \\ \sigma_4 \\ \sigma_5 \\ \sigma_6 \end{bmatrix} = \begin{bmatrix} C_{11} & C_{12} & C_{13} & 0 & 0 & 0 \\ C_{21} & C_{22} & C_{23} & 0 & 0 & 0 \\ C_{31} & C_{32} & C_{33} & 0 & 0 & 0 \\ 0 & 0 & 0 & C_{44} & 0 & 0 \\ 0 & 0 & 0 & 0 & C_{55} & 0 \\ 0 & 0 & 0 & 0 & 0 & C_{66} \end{bmatrix} \begin{bmatrix} \epsilon_1 \\ \epsilon_2 \\ \epsilon_3 \\ \gamma_4 \\ \gamma_5 \\ \gamma_6 \end{bmatrix} \quad (22)$$

By analogy, the flexibility matrix [D], which is the inverse of the constitutive matrix [C], can be simplified, as well.

$$\begin{bmatrix} \epsilon_1 \\ \epsilon_2 \\ \epsilon_3 \\ \gamma_4 \\ \gamma_5 \\ \gamma_6 \end{bmatrix} = \begin{bmatrix} D_{11} & D_{12} & D_{13} & 0 & 0 & 0 \\ D_{21} & D_{22} & D_{23} & 0 & 0 & 0 \\ D_{31} & D_{32} & D_{33} & 0 & 0 & 0 \\ 0 & 0 & 0 & D_{44} & 0 & 0 \\ 0 & 0 & 0 & 0 & D_{55} & 0 \\ 0 & 0 & 0 & 0 & 0 & D_{66} \end{bmatrix} \begin{bmatrix} \sigma_1 \\ \sigma_2 \\ \sigma_3 \\ \sigma_4 \\ \sigma_5 \\ \sigma_6 \end{bmatrix} \quad (23)$$

By applying the fundamentals of the Theory of Elasticity, it is possible to state:

$$\epsilon_1 = \frac{1}{E_{11}} (\sigma_1 - \nu_{12}(\sigma_2 + \sigma_3)) \quad (24)$$

$$\gamma_{ij} = \frac{1}{G_{ij}} \tau_{ij} \quad (25)$$

$$\frac{\nu_{ij}}{E_i} = \frac{\nu_{ji}}{E_j} \quad (26)$$

Since the stress components in the plane of each layer are much higher than the normal stress and transversal shear stresses, it is possible to consider plane stress state. And, the simplifications shown in Eq. (27) can be applied.

$$\sigma_{i3} = 0 \rightarrow \sigma_3 = \sigma_4 = \sigma_5 = 0 \quad (27)$$

Therefore the constitutive equation can be written as:

$$\begin{bmatrix} \sigma_1 \\ \sigma_2 \\ \sigma_6 \end{bmatrix} = \begin{bmatrix} Q_{11} & Q_{12} & 0 \\ Q_{12} & Q_{22} & 0 \\ 0 & 0 & Q_{66} \end{bmatrix} \begin{bmatrix} \epsilon_1 \\ \epsilon_2 \\ \gamma_6 \end{bmatrix} \quad (28)$$

Where:

$$Q_{11} = \frac{E_{11}}{1 - \nu_{12}\nu_{21}}; Q_{22} = \frac{E_{22}}{1 - \nu_{12}\nu_{21}}; \quad (29)$$

$$Q_{12} = \frac{\nu_{12} E_{22}}{1 - \nu_{12}\nu_{21}}; Q_{66} = G_{12}$$

To consider the different orientations ( $\theta$ ) of fibers in each layer, it is necessary to apply a Transformation Matrix [T] in order to transform stress or strain variables from the Global Coordinate System (Laminate Coordinates) to the Local Coordinate System (Layer Coordinates), Eq. (30).

$$\begin{bmatrix} \sigma_1 \\ \sigma_2 \\ \sigma_6 \end{bmatrix}_{Local} = \begin{bmatrix} \cos^2 \theta & \sin^2 \theta & 2 \cos \theta \sin \theta \\ \sin^2 \theta & \cos^2 \theta & -2 \cos \theta \sin \theta \\ -\cos \theta \sin \theta & \cos \theta \sin \theta & \cos^2 \theta - \sin^2 \theta \end{bmatrix} \begin{bmatrix} \sigma_1 \\ \sigma_2 \\ \sigma_6 \end{bmatrix}_{Global} \quad (30)$$

If the laminate is under Membrane Loadings [N], Shear Forces [Q] and Moments [M] (Figure 3), there are relations between these efforts and stress components as shown by Eq. (31).

$$\begin{bmatrix} N_x \\ N_y \\ N_{xy} \\ Q_x \\ Q_y \end{bmatrix} = \int_{-\frac{h}{2}}^{\frac{h}{2}} \begin{bmatrix} \sigma_x \\ \sigma_y \\ \sigma_{xy} \\ \sigma_{xz} \\ \sigma_{yz} \end{bmatrix} dz \quad (31)$$

$$\begin{bmatrix} M_x \\ M_y \\ M_{xy} \end{bmatrix} = \int_{-\frac{h}{2}}^{\frac{h}{2}} \begin{bmatrix} \sigma_x \\ \sigma_y \\ \sigma_{xy} \end{bmatrix} z dz$$

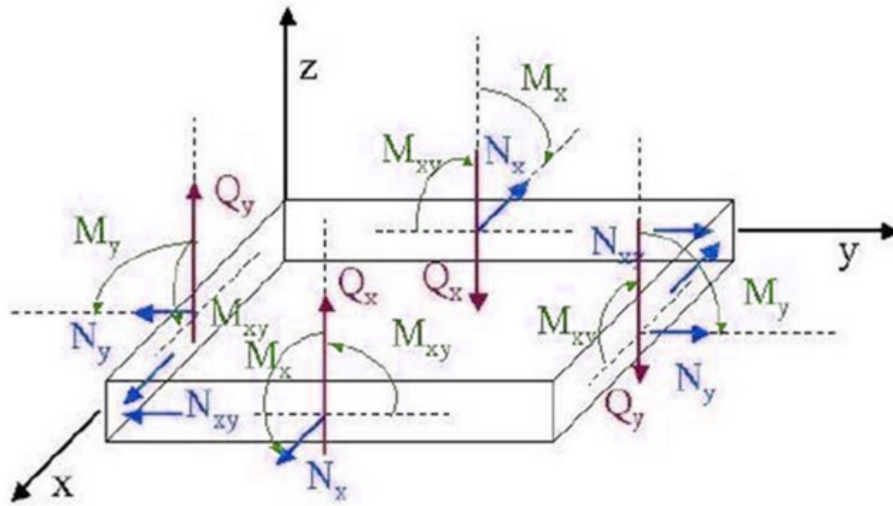


Figure 3. Membrane Loadings [N], Shear Forces [Q] and Moments [M] acting in the laminate.

At this stage, it is necessary to obtain the intern stresses of the laminate, which can be calculated by using CLT (Classical Laminate Theory). This theory is based on the Kirchhoffs' and other hypotheses, as well.

- ✓ The laminate is considered plane (as a plate) and the medium plane (medium surface), which split the laminate, is in the middle of the laminate and contains the plane x-y.
- ✓ The plies are perfectly linked and there is not relative displacement between plies, so the displacements are continuous.
- ✓ The matrix, which is between two plies, is very thin and it is not deformed by shear stress.
- ✓ The laminate is thin and Kirchhoff's kinematic hypotheses are applied. Therefore, these promotes  $\epsilon_{xz} = \epsilon_{yz} = \epsilon_z = 0$  and  $\sigma_{xz}, \sigma_{yz}, \sigma_z \ll \sigma_{xy}, \sigma_y, \sigma_x$ .

It is important to highlight that the Kirchhoff's kinematic hypotheses do not take into account the transversal shear stress. Hence, the transversal sections of the medium plane, which were plane and normal to the medium plane, remain plane and normal to the medium plane after the applied loading. Therefore:  $\epsilon_{xz} = \epsilon_{yz} = \epsilon_z = 0$ . However, the stresses  $\sigma_{xz}$ ,  $\sigma_{yz}$  and  $\sigma_z$  are very important for delamination analyses. Moreover, if the structure is thick, the

structural analyses should be affected in case of the transversal shears are not considered. Thus, for thick laminates or delamination analyses, it is necessary to use other kinematic hypotheses such as Mindlin-Reissner or Higher-order Shear deformation Theory – HST. However, in this work, it is considered mainly thin laminates, i.e. the relation length (or width) per thickness is minimum higher than 10.

Reorganizing the equations above, the relation (25) without Shear Forces can be rewritten in terms of the stiffness of the laminate:

$$\begin{bmatrix} N \\ M \end{bmatrix} = \begin{bmatrix} [A] & [B] \\ [B] & [D] \end{bmatrix} \begin{bmatrix} \varepsilon_o \\ K \end{bmatrix} \quad (32)$$

where:

$$[A] = \sum_{k=1}^n \int_{h_{k-1}}^{h_k} [\bar{Q}]_K dz = \text{membrane stiffness matrix.}$$

$$[B] = \sum_{k=1}^n \int_{h_{k-1}}^{h_k} [\bar{Q}]_K z dz = \text{coupling stiffness matrix.}$$

$$[D] = \sum_{k=1}^n \int_{h_{k-1}}^{h_k} [\bar{Q}]_K z^2 dz = \text{bending/torsion stiffness matrix.}$$

$[\varepsilon_o]$  = strains obtained via Kirchhoff's kinematic hypotheses

$[K]$  = curvatures via Kirchhoff's kinematic hypotheses

$$[\bar{Q}] = [T]^{-1}[Q][T] \quad ([T] \text{ is the Transformation Matrix in the Eq (24)}).$$

If the coupling matrix  $[B]$  is not null, then membrane loadings can cause not only normal and shear strains, but also curvatures  $K_x$ ,  $K_y$  and  $K_{xy}$ . By analogy, moments loadings can cause not only curvatures  $K_x$ ,  $K_y$  and  $K_{xy}$ , but also normal and shear strains. By the other side, if the coupling matrix  $[B]$  is null, these effects cannot occur. In fact, matrix  $[B]$  is null for symmetric laminates, and this is easily proved by verifying that stiffness part related to  $z$  positive values are canceled by stiffness part related to  $z$  negative values.

Finally, the stiffness of the laminate, required to obtain the natural frequencies, can be determined by calculating ABD, which depend on the mechanical properties of the plies, the orientation of the fibers in each ply and the thickness of each ply.



---

---

## 3. SHM FOR METAL-COMPOSITE JOINTS

---

---

### 3.2. REVIEW

Specifically on the subject of SHM of bonded joints, few studies were performed as shown by the literature. Vantomme (1992) studied the possibility of using modal parameters to perform a non-destructive evaluation of the integrity in large joint structures made of glass fiber reinforced polyester. One of his conclusions was that it is advantageous to use modal frequency over modal damping. Chiu et al. (2000) used piezoceramic materials in order to detect debonding damage for a composite repair attachment and its parent metallic structure. The researchers verified the reliability of the method, proving the piezoceramic material provided feedback and demonstrated the integrity of the structure. Zagrai et al (2008) monitored connectors and joints by using nonlinear ultrasonic response. The authors reported a variation of the non-linear response of the joints in relation to the applied structural loads. Qing et al. (2006) analyzed the influence of the performance of piezoelectric elements placed on bonded joints of aluminium parts. The authors concluded that the electromechanical impedance and resonance frequency of the piezoelectric transducer are linked to the thickness and elasticity of the adhesive. Quaegebeur et al. (2011) used a piezoceramic element to offer in-situ inspection of a bonded joint of carbon fiber reinforced polymer and titanium adherents. They applied SHM system based on lamb wave technique. The authors concluded that the methodology used was valid to identify the debonding damage at the joint.

Previous studies have been performed by Group of Aeronautic Structures-USP on the topic approached by the present work. Borges (2012) first started studying SHM of metal-composite bonded joints at his Master's Dissertation. The study was based on both computational and experimental analyses. The specimens had been biclamped as boundary condition, and they were fixed together by clamps in the set-up of the experiments. The justification for putting all specimens together was to mitigate possible variations in the result due to the different and unknown normal forces originated from the pressure of the clamps. The author concluded that an approach with known normal loads in the boundary conditions should be advantageous for future studies. Medeiros et al. (2013a) used damage quantification

metrics to identify debonding damage on metal-composite bonded joints. Medeiros et al (2013b) then comparing computational and experimental analyses, providing more explanations about damage identification in metal-composite bonded joints and metrics for damage quantification. Medeiros et al (2014b) showed experimental analyses also approached in the present Master's Dissertation, where composite-metal bonded joints were investigated under a pre-loaded biclamped and free-free boundary conditions. Regarding the SHM dedicated only for composite structures, Medeiros et al. (2013c) performed dynamic experimental analyses of a composite plate under free-free condition using piezoelectric sensors. The study also evaluated several types of damage metrics. The authors concluded that the vibration based methods provide limited information in regards to location and type of damage. However, a combination of vibration-based methods and damage metrics can provide reliable information on the structural integrity. In parallel to this study, Sartorato et al (2013b) formulated a quadratic shell finite element in ABAQUS via UEL (User Element subroutine). Sartorato and Tita (2014) formulated, implemented and evaluated a non-linear shell finite element with piezoelectric capabilities. The authors concluded that the element is reliable for simulation of smart structures with good accuracy.

### 3.3. SPECIFIC OBJECTIVES

The main objective consists on contributing for the development of SHM systems based on vibration methods to be applied in metal-composite bonded joints. A complete SHM system is able to identify and localize damage, as well as to evaluate the severity of the damage of metal-composite bonded joints. Thus, the main objective of the present work is focused on the identification of the damage. For that reason, it can be divided in different goals:

- ☑ Gather studies and results on the field of SHM for metal-composite bonded joints previously developed by the academy, giving more focus to those applied vibration based methods.
- ☑ Perform vibration experimental analyses on the specimens of metal-composite bonded joints.
- ☑ Develop computational models by using the software ABAQUS for the metal-composite bonded joints without damage and piezoelectric sensors and confront the

numerical results to the experimental data in order to evaluate the reliability of the undamaged Finite Element model (FEM).

- ☑ Based on the experimental data, develop a computational model with the presence of debonding damage and evaluate the potentialities and limitations of the FEM, considering the presence of damage in the dynamic signature of the metal-composite bonded joint.
- ☑ Insert piezoelectric sensors in the FEMs and confront the results to the experimental data. Based on the numerical results, refine the FEM to represent with more accuracy the experiments.
- ☑ Calculate Damage Quantification Metrics by using Frequency Response Functions obtained from computational and experimental analyses.

## 3.4. EXPERIMENTS

### 3.4.1. MATERIALS AND SPECIMENS

The specimens were metal-composite bonded joints of carbon-reinforced polymers and titanium alloy beams joined by epoxy resin. The dimensions are presented in Figure 4, it is important to point that this schema displays the configuration of the specimen, which has both the damage (represent by Teflon tape) in the joint and the presence of the piezoelectric (PZT) sensor, but the dimensions remain the same for all the other specimens, regardless of the absence of these elements (damage and/or PZT sensor).

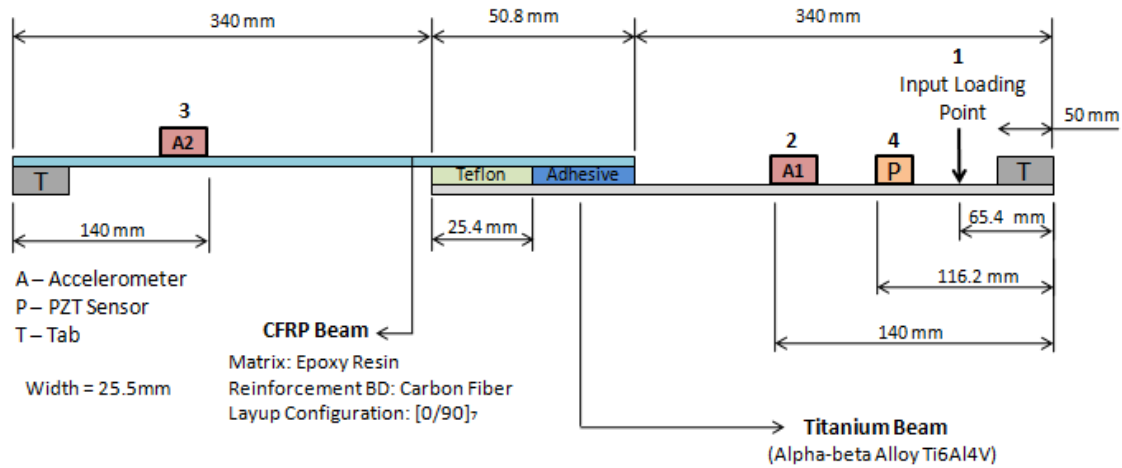


Figure 4. Metal-composite bonded joint specimens.

The composite part is specified by Hexcel<sup>™</sup> as G0904 D 1070 TCT and was made of bidirectional textile of carbon fibers commonly used in aircraft structures. The matrix consisted of the resin HexPly M20 Epoxy, also produced by Hexcel<sup>™</sup>. The properties of the CFRP (Carbon Fiber Reinforced Polymer) are presented at Table 1.

The metallic part was made of Titanium Alloy - Ti6Al4V, which does not have galvanic incompatibility in contact with the composite part. The properties of the alloy were acquired in the MIL-HDBK-5J (2003) and are shown at Table 2.

The adhesive component was the epoxy resin EA934NA by Hexcel<sup>™</sup>, which is vastly used by the aeronautical industry for jointing metal and composite structures. Its properties can be seen at Table 3. It is relevant to point that in the cases of damaged specimens, the debonding effect was obtained by replacing the adhesive component by a Teflon layer through 50% of the overlap area.

The piezoelectric sensor consisted of a PZT sensor type Midé QP10n. It is composed of a piezoelectric ceramic plate of Lead-Zirkonate-Titanate (PZT) and epoxy matrix, which is covered by thin electrodes on the bottom and top sides. The equivalent properties of the PZT sensor were calculated from a numerical homogenization method proposed by Medeiros et al. (2014a) and the values are presented at Table 4.

Details about the fabrication process of these specimens are available at Borges(2012).

Table 1. CFRP properties.

<b>Mechanical Properties and Allowable Values</b>	<b>Unit</b>	<b>Value</b>
Young's modulus in longitudinal direction - $E_{11}$	GPa	41.41
Young's modulus in transverse direction - $E_{22}$	GPa	39.15
Poisson's coefficient - $\nu_{12}$	-	0.107
Shear modulus in ply plane - $G_{12}$	GPa	2.82
Longitudinal direction tensile strength - $X_T$	MPa	$494.0 \pm 21$
Longitudinal direction compressive strength - $X_C$	MPa	$202.0 \pm 15$
Transverse direction tensile strength - $Y_T$	MPa	$494.0 \pm 19$
Transverse direction compressive strength - $Y_C$	MPa	$202.0 \pm 13$
Shear strength value in ply plane - $S_{12}$	MPa	$81.0 \pm 3$
Shear strength value out of plane - $S_{23}$	MPa	$65.0 \pm 3$
Tensile strain limit in longitudinal direction - $X'_T$	-	$0.0116 \pm 0.0013$

Table 2. Titanium Alloy - Ti6Al4V – properties.

<b>Properties</b>	<b>Unit</b>	<b>Value</b>
Young's Modulus of Elasticity - E	GPa	116.52
Poisson's Coefficient - $\nu$	-	0.31
Density - $\rho$	Kg/m <sup>3</sup>	4428.78

Table 3. Adhesive's properties.

<b>Properties</b>	<b>Unit</b>	<b>Value</b>
Strength	MPa	40
Young's modulus of Elasticity - E	MPa	3790
Glass Transition Temperature (Cure @ 25°C)	°C	75
Glass Transition Temperature (Cure @ 90°C)	°C	129

Table 4. Piezoelectric sensor properties (Mide QP10n).

<b>Properties</b>	<b>Unit</b>	<b>Value</b>
$c_{11}$	GPa	81.73
$c_{12}$	GPa	5.23
$c_{13}$	GPa	50.06
$c_{33}$	GPa	46.35
$c_{44}$	GPa	5.91
$c_{66}$	GPa	5.63
$e_{13}$	C/m <sup>2</sup>	-5.24
$e_{15}$	C/m <sup>2</sup>	1.13
$e_{33}$	C/m <sup>2</sup>	12.85
$\epsilon_{11}$	nF/m	6.89
$\epsilon_{33}$	nF/m	5.73
$\rho$	Kg/m <sup>3</sup>	7400

Four types of specimens were used in the experiments: (1) undamaged joint with only accelerometers present (no piezoelectric sensor); (2) damaged joint with only accelerometers present (no piezoelectric sensor); (3) undamaged joint with accelerometers and piezoelectric sensor; (4) damaged joint with accelerometers and piezoelectric sensor. The specimen configurations and corresponding identification names are presented at Table 5.

Table 5. Specimen identification.

<b>ID</b>	<b>Damage</b>	<b>PZT Sensor</b>
S1P0	No	No
S2P0	Yes	No
S1P1	No	Yes
S2P1	Yes	Yes

The choice for evaluating these types of specimens was based on the objective for analyzing the influence of damage and/or PZT sensor in a combined or isolated way. By comparing the results of the dynamic signatures of specimen S1P0 and specimen S2P0, it is possible to isolate the influence of the debonding damage. By comparing the results of the dynamic signatures of specimen S1P0 and specimen S1P1, it is possible to isolate the influence of the piezoelectric sensor. Lastly, by comparing the results of specimen S1P1 and

specimen S2P1 is possible to verify the reliability of the analysis of the piezoelectric sensor response as means to identify damage on bonded joints.

### 3.4.2. EXPERIMENTAL SET-UPS AND INSTRUMENTATION

The vibration tests were performed considering two different boundary conditions. The first set was placed under free-free condition, represented by the specimen being held via a very flexible elastomeric wire, as shown in Figure 5. Thus, one end of the wire was attached to a metal support, and the other end was attached to the edge of the metallic part of each specimen. The second set was placed under biclamped condition, considering a known traction pre-load (Figure 6). The justification for this approach was based on the previous study performed by Borges (2012), which showed difficulties of estimating the pre-loads originated by the encastre device (clamps).

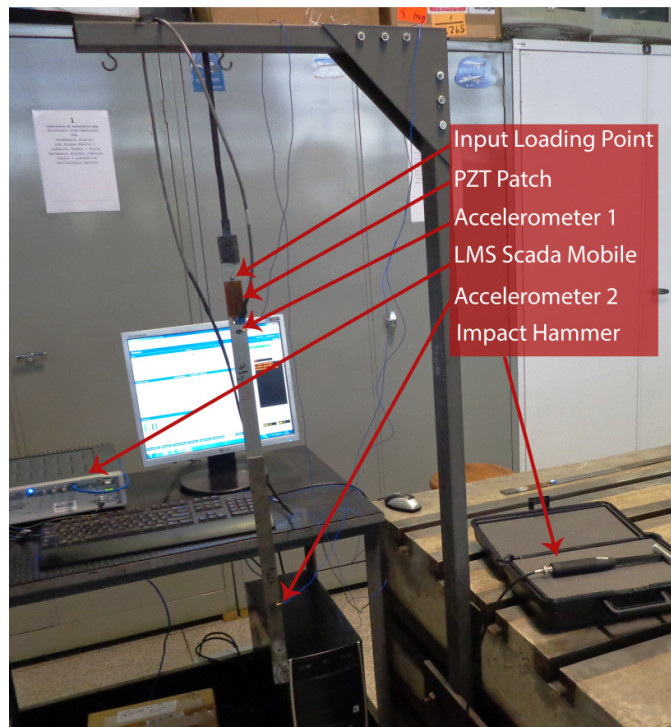


Figure 5. Experimental set-up for the free-free condition.

The data was acquired by using LMS SCADAS Mobile, set to cover a bandwidth of 1024 Hz with 2048 spectral lines. Lastly, to reduce the random fluctuation in the estimation of FRFs, the apparatus was set to average individual time records in groups of five. The acquisition software also performed Coherence analysis based on the acquisition of 5 repetitions for each experimental condition.

Besides using the piezoelectric sensor previously mentioned, data acquisition was also performed by using two accelerometers Piezotronics Model 352C22. One was set on the metallic part - with 9.94 mV/g sensitivity - and another on the CFRP - with 9.0 mV/g, which were placed on the specimens at the points 2 and 3 shown by Figure 4. The piezoelectric smart sensor was placed on the metallic part at point 4. The input load was performed by using an impulse force Piezotronics hammer Model PCB 0860C3 on the metallic part, more specifically at point 1 shown by Figure 4.

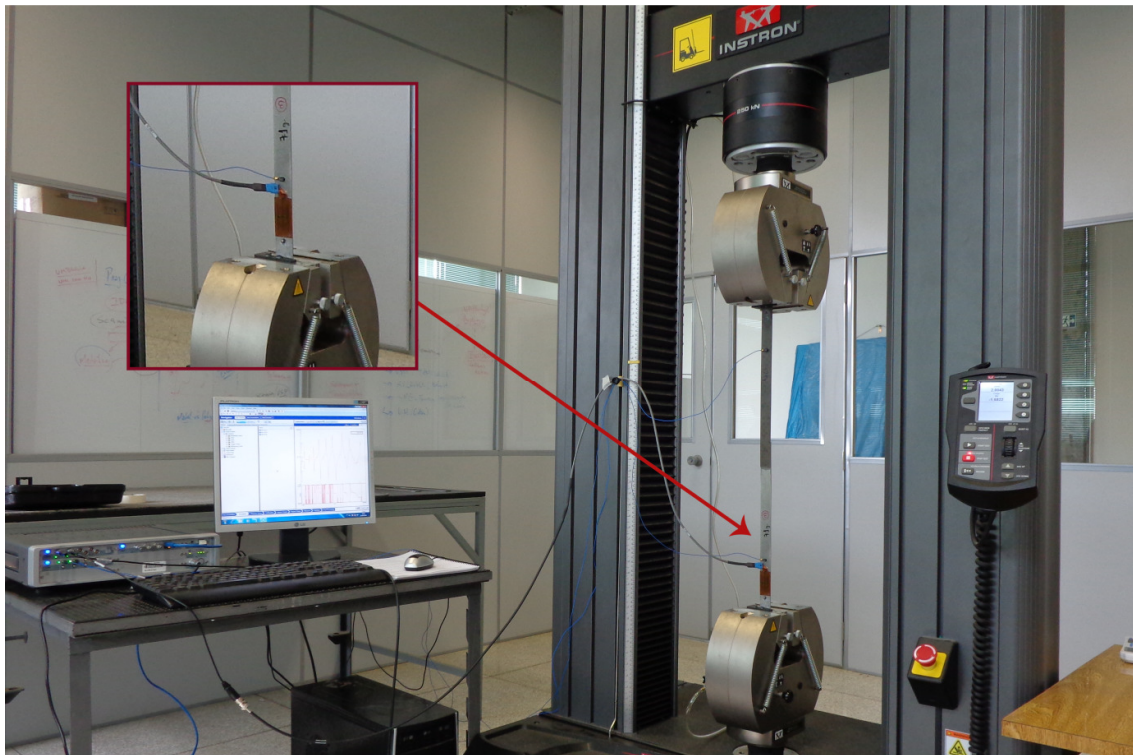


Figure 6. Experimental set-up for biclamped condition.

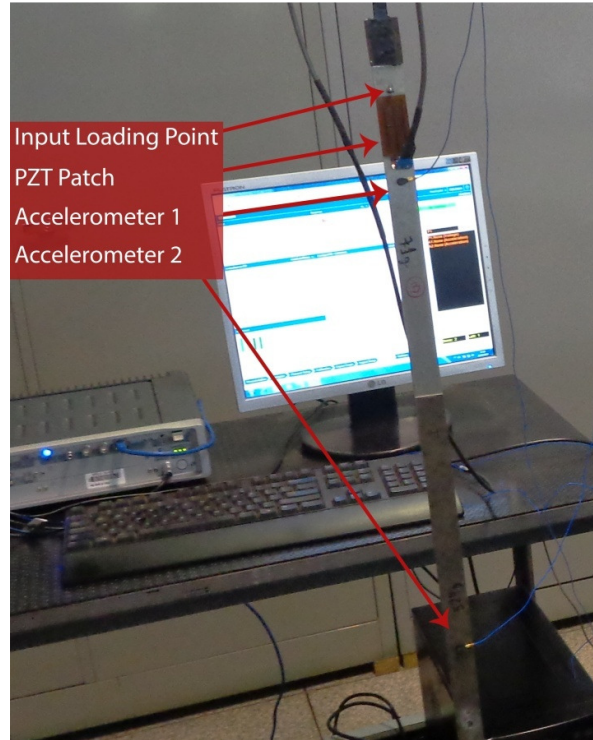


Figure 7. Disposition of (output) sensors and input point for the specimens.

### 3.4.3. EXPERIMENTAL PROCEDURES

As previously stated, considering the four types of specimens and two types of boundary conditions, eight experiments were performed in total. The data acquired from these eight experiments were used to perform seven analyses.

The first analysis (analysis 1) compared the dynamic response of the specimens S1P0 and S2P0 to verify the influence of the presence of damage in the bonded joint. The second one (analysis 2) compared the dynamic response of the specimens S1P0 and S1P1 to verify the influence of the presence of the piezoelectric sensor. The third analysis (analysis 3) compared the dynamic response of specimens S1P1 and S2P1 to perform the structural health monitoring via the piezoelectric response of the PZT sensor. Analyses 4 through 6 are equivalent to the previously mentioned, but regarding the biclamped condition. Finally, analysis 7 aimed in verifying the different behavior of the dynamic signature of the bonded joint, considering different boundary conditions.

### 3.4.4. DAMAGE METRICS

For the analyses 1, 3, 4 and 6, the damage was initially quantified by using the damage metric present in the work of Mickens et al. (2003). This method uses the magnitudes of the FRFs of both the undamaged and damaged structures, respectively  $H^i$  and  $H^d$ . Giving a certain range frequency  $[f_1, f_2]$  and certain frequency increment  $\Delta f$ , the damage factor (DF) can be calculated by the following equations:

$$y(f) = \left| \frac{|H^i| - |H^d|}{|H^i|} \right| \quad (33)$$

$$DF = \frac{\Delta f}{f_2 - f_1} \sum_i^n y_i(f) \quad (34)$$

A second metric was applied as well, the calculations follow the same procedure as the one described previously, but phase angle values were used instead of magnitudes.

$$\phi^x = \text{Tan}^{-1} \left( \frac{\text{Im}(H^x)}{\text{Real}(H^x)} \right); \quad x = i, d \quad (35)$$

$$y(f) = \left| \frac{|\phi^i| - |\phi^d|}{|\phi^i|} \right| \quad (36)$$

$$DF = \frac{\Delta f}{f_2 - f_1} \sum_i^n y_i(f) \quad (37)$$

### 3.4.5. PROPOSED DAMAGE METRICS

The methodology proposed by Mickens to quantify the damage is strictly based on the relative differences of magnitude between the dynamic signatures of the intact (undamaged) and damaged specimens.

As explained previously, this method is guided by the equations:

$$y(f) = \left| \frac{|H^i| - |H^d|}{|H^i|} \right| \quad (33)$$

$$D = \frac{\Delta f}{f_2 - f_1} \sum_i^n y_i(f) \quad (34)$$

This procedure includes two particular issues. The first one is the possibility of high values of damage, which are obtained when the denominator of Eq. (28) is low. This can occur because the difference between frequencies is too small. The second one is the fact that the damage factor has a tendentious behavior, because there are higher contributions from the dynamic response in which the damaged specimen has FRF magnitudes higher than the intact one.

When  $H^i$  approaches zero, the value of  $y(f)$  can become unreasonably high, even when the absolute difference between  $H^i$  and  $H^d$  is small. This can be observed during the quantification of the damage for the bonded joint specimen without PZT sensor for the frequencies around 10-20 Hz and 90-130 Hz as shown by Figure 8. The same behavior can be also observed when applying Mickens' method into phase data, as seen in Figure 10.

The issue with the tendentious behavior causes a difference of damage contribution for the same absolute difference  $|H^i - H^d|$ , depending on the FRF curve which is used. If the damaged FRF curve shows higher values, the damage contribution will be higher than if the situation were switched (intact FRF shows higher values than damaged one). This occurs because for the same absolute difference, the denominator will have a greater value if  $H^i$  is greater than  $H^d$ , this division by a larger number results in a smaller contribution for the damage factor. This can be confirmed by the Figure 9 for the range from 70 to 90 Hz.

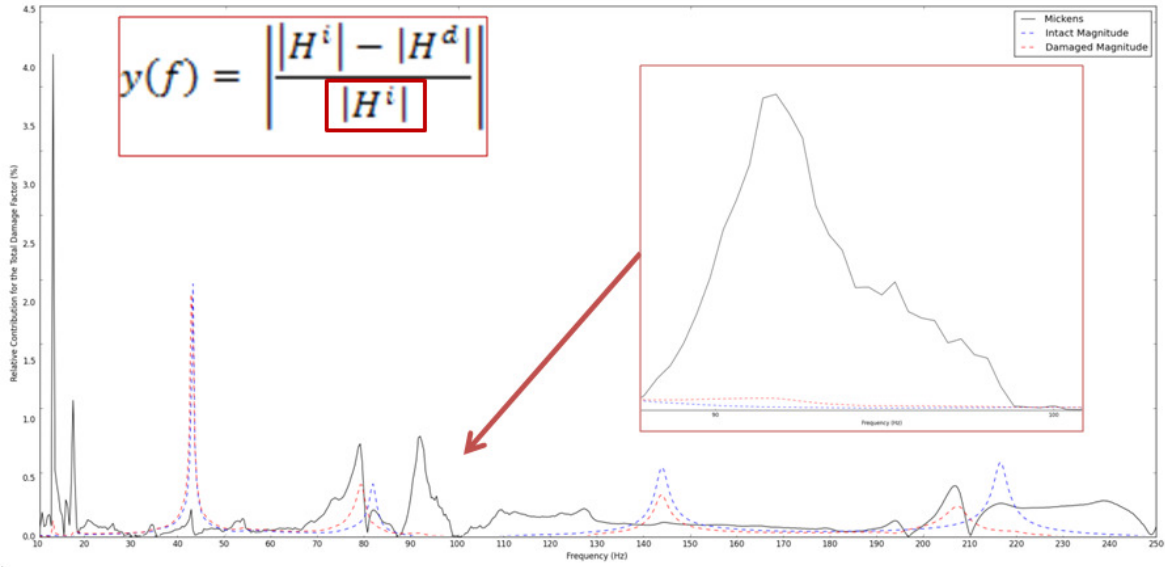


Figure 8. Mickens Damage Quantification (Magnitude) - Bonded Joint – Free-Free - S1P0[A2] vs. S2P0[A2] (Low value divisions)

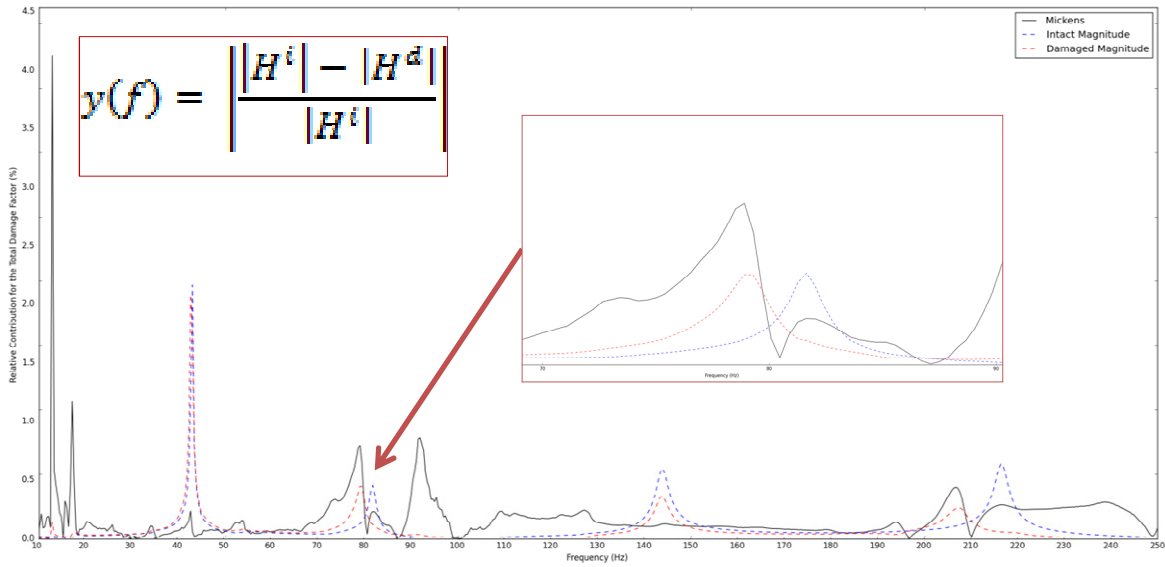


Figure 9. Mickens Damage Quantification (Magnitude) - Bonded Joint – Free-Free - S1P0[A2] vs. S2P0[A2].(Tendentious contributions)

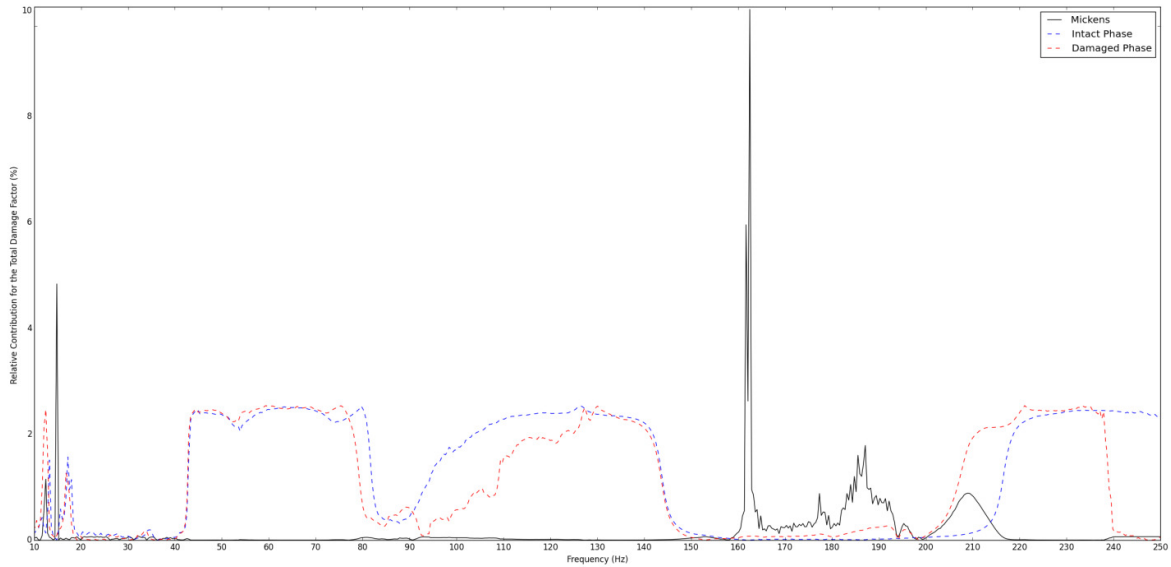


Figure 10. Mickens Damage Quantification (Phase) - Bonded Joint – Free-Free - S1P0[A2] vs. S2P0[A2].

To solve these issues, two modifications were implemented into the metric.

The first step consists in the implementation of a filter that reduces the occurrences of small denominators in the calculations. This filter operates on both the intact and damaged FRFs. This is achieved by the following procedures:

- The third quartile of the data is automatically accepted as the default. To obtain the third quartile, it is necessary to first arrange the values of the array in crescent order. The third quartile corresponds to the value between the median and the highest value of the array. In other words, given an array with  $n$  elements, if this array is arranged in crescent order, the third quartile will be the value stored at the  $0.75*n$  element.
- The values bellow the third quartile are only considered if their magnitude is greater than 15% of the highest value of the data. This step prevents data of reasonable magnitude to be ignored in systems that contain a low standard deviation.
- A range will only be ignored if it has been filtered in both the intact and damaged curves. By the end of the process, the filter can accept a number of values that cover from 25% up to 100% of original data. A value will be only ignored during the damage quantification if it is in a filtered frequency for both the intact and damaged FRFs. The overall result of this process is displayed at Figure 11.

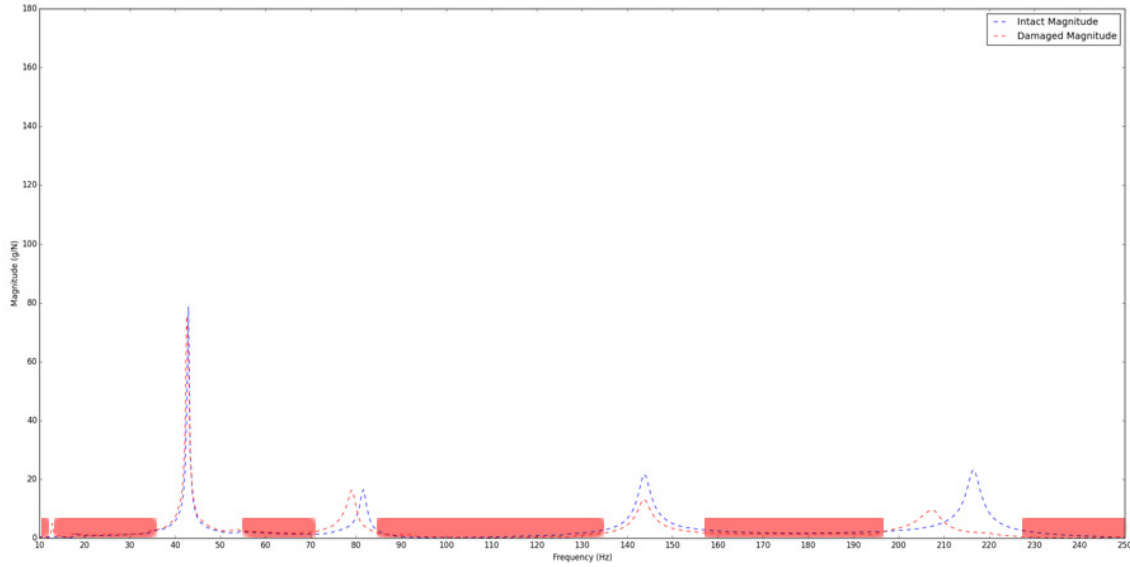


Figure 11. Filtering of specific frequency ranges of the Data

The next step has the purpose of solving the issues with the tendentious behavior of the damage contribution. This is solved by changing the denominator of the Eq. (33) to  $\min(H^i, H^d)$  or  $\max(H^i, H^d)$ . The modified damage metric applies  $\max(H^i, H^d)$  values in order to avoid divisions by small numbers, which provide high values for damage metric.

The graphics in Figures 8 and 10 can be plot using the modified damage metrics as shown by Figures 12 and 13.

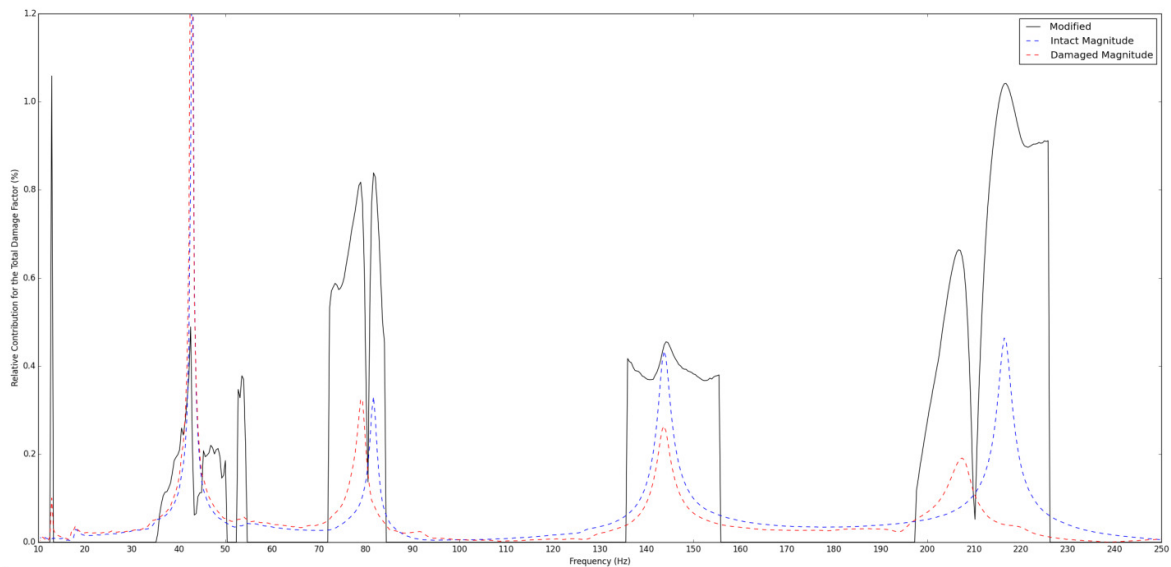


Figure 12. Modified Damage Quantification (Magnitude) - Bonded Joint – Free-Free - S1P0[A2] vs. S2P0[A2].

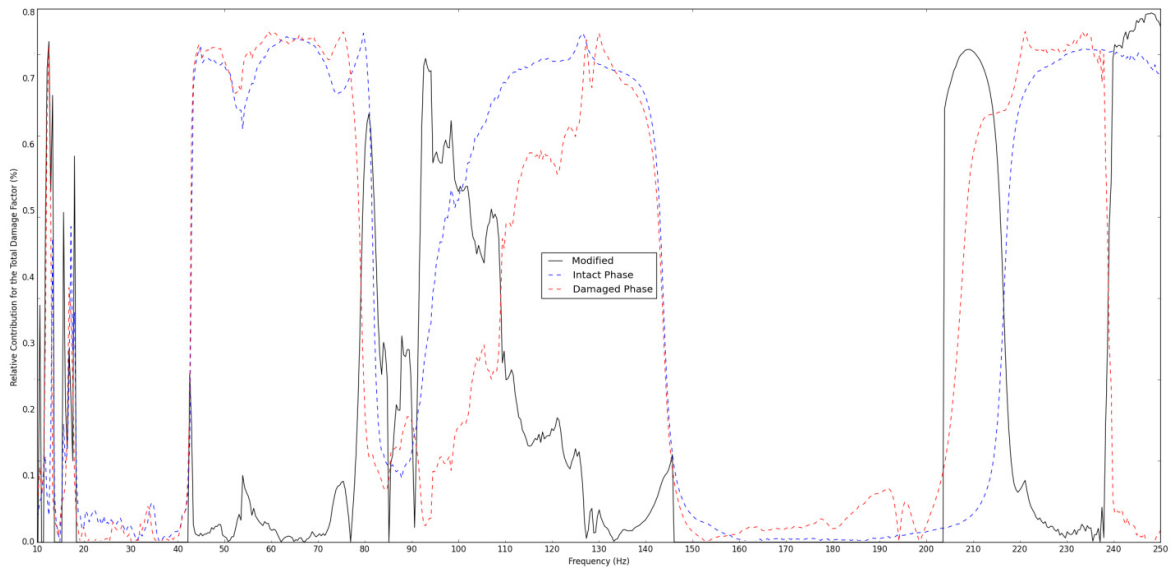


Figure 13. Modified Damage Quantification (Phase) - Bonded Joint – Free-Free - S1P0[A2] vs. S2P0[A2].

It is important to highlight that in Attachment 2, there is the implementation code via Python of the procedure described above.

### 3.5. FINITE ELEMENT ANALYSIS

The computational models were developed in ABAQUS<sup>TM</sup> v6.12. As explained in previous chapters, all the studies of damage quantification in this dissertation involve an analysis of both the dynamic signatures obtained computationally and experimentally.

The specimens were modeled with both the CFRP and the titanium alloy parts by using shell elements. The FE mesh was done by using elements defined by ABAQUS as S4R. This shell element has 4 nodes with 6 degrees of freedom (all translations and rotations in the tridimensional space) and uses reduced integration. The models are exposed from Figures 14 to 17.

The mesh for the piezoelectric sensor was modeled by using solid elements. The reason for this is because ABAQUS<sup>TM</sup> v6.12 formulation cannot generate shell elements that

support piezoelectric formulation, i.e. it is possible to simulate a problem with piezoelectric coupling only by using solid elements. The element is defined by ABAQUS as C3D20RE, which corresponds to a piezoelectric brick of quadratic order and uses reduced integration. Figure 17 shows in details the mesh elements for joint and piezoelectric sensor. Although the representation generated by ABAQUS shows thickness on all elements only the PZT sensor is solid.

The undamaged bonded joint was simplified by using the tie constraint defined by ABAQUS, meaning that it was assumed perfect adhesion and disregarding the thickness of the adhesive layer. In the regions where the debonding damage was present, the FE model represented the damage by removing the tie constraint over 50% of the overlap region. Surface-to-surface contact interaction could not be inserted in the model due to the limitations of the Modal Dynamics Procedure in ABAQUS<sup>TM</sup> v6.12. The end-tabs, which have the purpose of avoiding secondary moment effects in the specimen for the biclamped condition, were modeled via section assignment.

In regards to the boundary conditions, the free-free condition was represented by an elastomeric wire in the experiments, which was simulated by using spring element (Spring Engineering Assembly Feature - ABAQUS<sup>TM</sup> v6.12). The stiffness of the spring element was set so that the resulting natural frequency would be lower than 10% of the first non-rigid natural frequency of the structure in order to avoid the influence of the spring in the joint dynamic behavior. This procedure returned a stiffness of 70 N/m for the spring element.

The biclamped boundary condition was modeled by using encastre (fixed) condition in the region of the titanium alloy part and a prescribed displacement condition, which blocked all displacements and rotations at the end of the CFRP with the exception of the displacement in X direction. It was set the value of 0.23 mm in X direction, which corresponds to the pre-load applied by the machine test during the experiments as show in Figure 16.

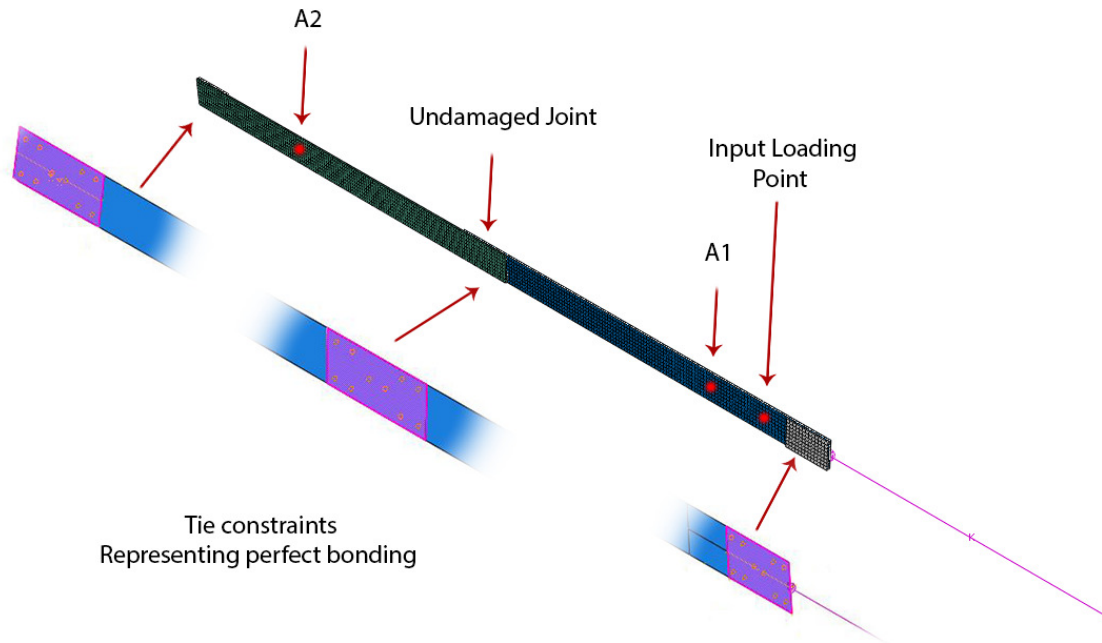


Figure 14. Finite Element model for the undamaged bonded joint without Piezoelectric Element (S1P0)/

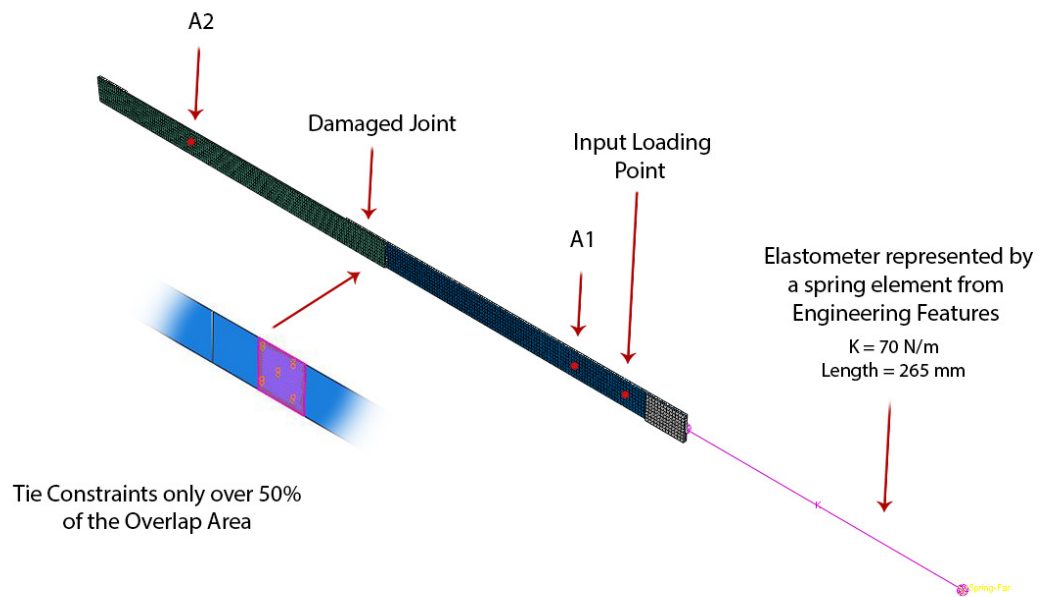


Figure 15. Finite Element model for the damaged joint without the Piezoelectric Element (S2P0).

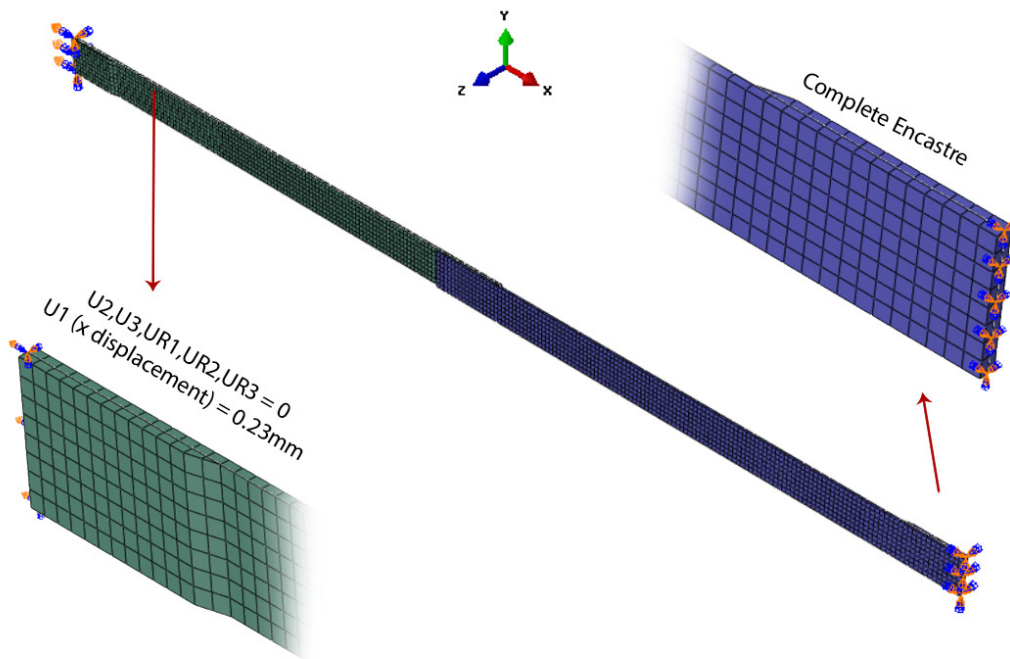


Figure 16. Boundary conditions and prescribed displacement for the biclamped model.

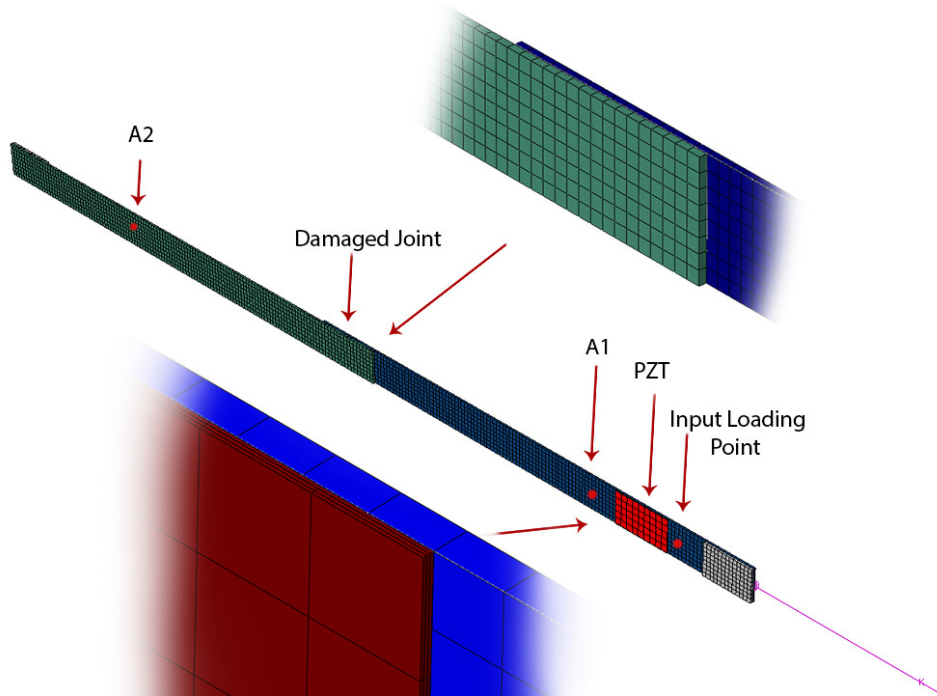


Figure 17. Finite Element model for the damaged joint with Piezoelectric Element (S2P1).

The dynamic analyses were performed via the "Steady-State Dynamics, Modal" step via ABAQUS™ v6.12. It is important to highlight that this step always need to be preceded by the "Frequency" step, which calculates the Eigen Values and Eigen Frequencies for the non-transient condition. Additionally, for the pre-loaded biclamped case, the steps need to be set for non-linear approach and "Frequency" must be preceded by a non-linear "Static, General" step via ABAQUS™ v6.12, which calculates and propagates the displacements and internal loads caused by the boundary pre-load to the "Frequency" step. To properly carry the complex parts of the eigenvectors generated by the deformed shape stresses and strains state into the "base state", it is important to follow this step with the "Complex Frequency" step, and request the same amount of eigenvalues. In the case of this study, the modal domain was composed of the 25 first eigenvalues and eigenvectors (the first 6 being related to the rigid-body movements). This number of eigenvalues was obtained by doing a convergence analysis of the FRF obtained for Specimen 3 with an increasing number of eigenvalues and the given desired bandwidth. Lastly, a "Steady-state dynamics, Modal" step was used to effectively gather the dynamic signatures. This step was complemented with "Direct modal frequency-based damping" for obtaining better results. There is a schema in Figure 18, showing the difference in the procedures in accordance to the boundary condition.

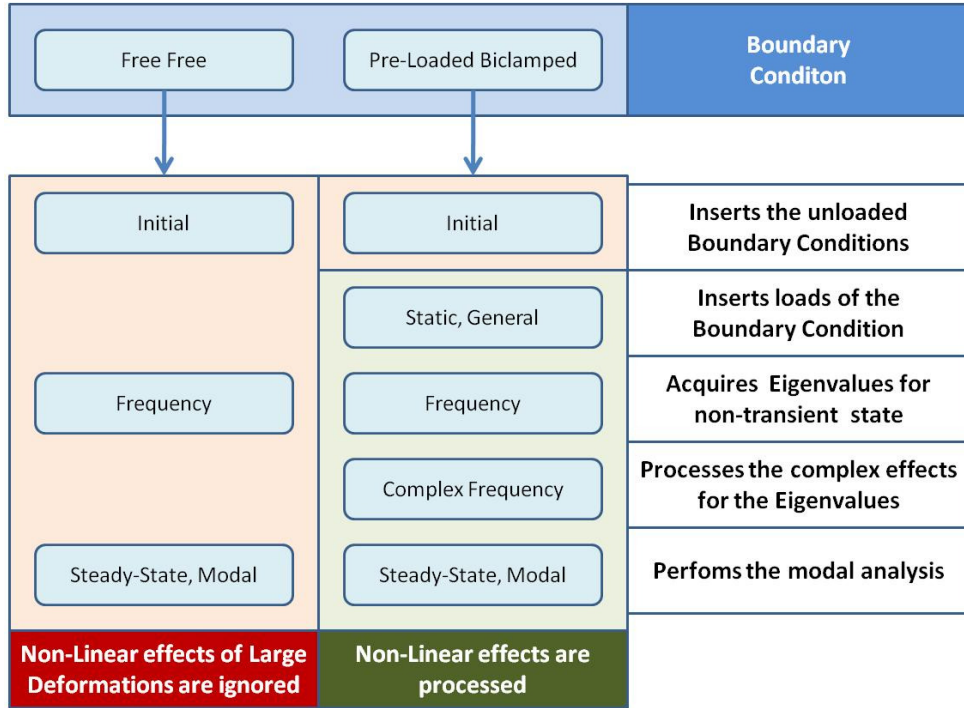


Figure 18. Step procedures for the numerical Modal Analysis via ABAQUS™ v6.12.

The damping factors used were obtained by approximating the modal peaks of the experimental FRFs into independent second order transfer functions. Therefore, each transfer function had a single natural frequency and a single damping factor associated to it. This procedure was made using Matlab™ 2013 and a frequency domain identification tools.

### 3.6. RESULTS

The experimental and computational analyses are shown in two parts. First, the results for free-free boundary conditions are discussed, and, after that, the investigation for biclamped boundary conditions.

#### 3.6.1. FREE-FREE BOUNDARY CONDITION

As previously stated, the experimental FRFs were used to obtain Critical Damping Factors for each non-rigid vibration mode in the frequency range of interest. The damping

factors related to the metal-composite bonded joints for free-free condition are presented at Tables 6 through 9. It is important to highlight that the Matlab subroutine (based on the Half-Potential Method) disregarded modal damping influence of the 1st flexural mode shape (14.21 Hz) due to its peak magnitude being much lower than the surround peaks.

Table 6. Critical Damping Factors for S1P0 – free-free.

<b>Frequency [Hz]</b>	<b>Critical Damping Factor</b>
2.18	0.00326
14.21	-
42.52	0.00459
81.03	0.00796
140.88	0.00733
215.10	0.00667

Table 7. Critical Damping Factors for S2P0 – free-free.

<b>Frequency [Hz]</b>	<b>Critical Damping Factor</b>
42.30	0.00546
76.88	0.01240
139.67	0.00749
200.96	0.01220
296.60	0.01293

Table 8. Critical Damping Factors for S1P1 – free-free.

<b>Frequency [Hz]</b>	<b>Critical Damping Factor</b>
42.90	0.00443
81.59	0.00773
143.83	0.00919
216.54	0.00676
305.95	0.01182

Table 9. Critical Damping Factors for S2P1 – free-free.

<b>Frequency [Hz]</b>	<b>Critical Damping Factor</b>
2.17	0.00076
42.74	0.00435
78.95	0.01130
143.74	0.01005
207.07	0.01050
306.23	0.01140

The first few flexible modes of the structure are the most important for identification of the damage by using FRFs. In the present work, the first five non-rigid vibration modes of the metal-composite bonded joints occur before 250 Hz, which was obtained from ABAQUS by using a simple steady-state analysis (Frequency Step) as shown in Table 10 and Figure 19. Notice that the frequencies presented at Table 10 are for the S1P0, which does not have damage and piezoelectric sensor. However, as it will be shown in the analyses ahead, the shift of the natural frequencies caused by the piezoelectric sensor or by the presence of the debonding damage is not high. Therefore the range of [10,250] Hz will be valid for the analyses of all specimens, since it is assured the first five non-rigid vibration modes will be within this range. The first non-rigid vibration modes are easier to analyze due to the small number of modes nodes and lower frequency of operation. Also, the magnitudes of the displacements induced on these modes are higher and more representative on the overall dynamical behavior of the structure.

For the next results, it is crucial to remember the points shown by Figure 4. For example, the FRFs  $H_{12}$  and  $H_{13}$  are obtained for output measurement from accelerometers 1 (position 2) and 2 (position 3), respectively. And, FRF  $H_{14}$  is determined for output measurement from the piezoelectric sensor.

Table 10. Modal Analysis for bonded joints – Numerical natural frequencies of S1P0 – free-free.

<b>Mode</b>	<b>Frequency [Hz]</b>
1 <sup>st</sup> Flexural	14.21
2 <sup>nd</sup> Flexural	39.89
3 <sup>rd</sup> Flexural	78.09
1 <sup>st</sup> Torsional	114.90
4 <sup>th</sup> Flexural	133.76

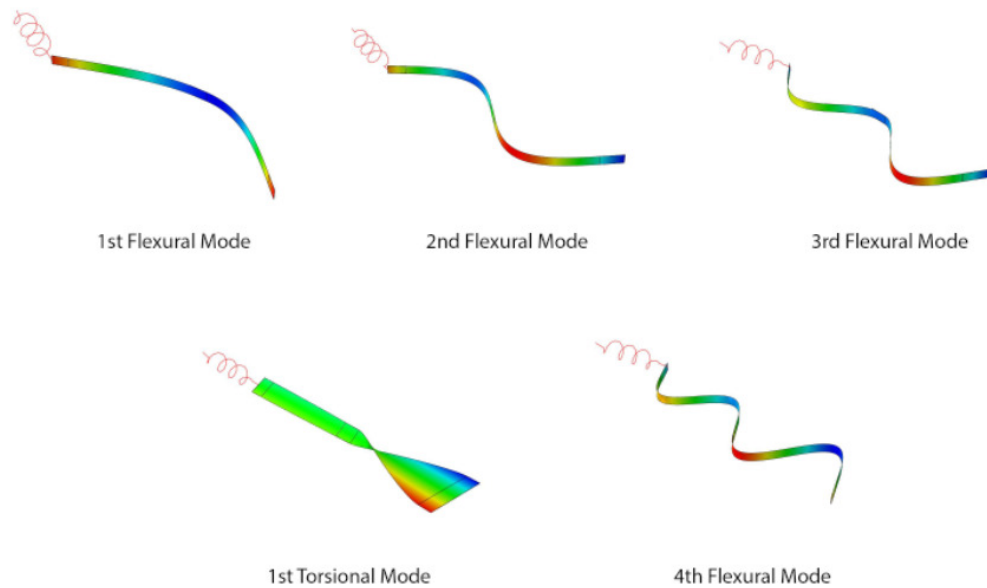


Figure 19. The first non-rigid mode shapes for the undamaged bonded joint - free-free.

It should be observed that the general computational analysis detected a torsional mode at the frequency of 114.90 Hz, which is shown at Table 10 and Figure 19. However, it will be noticed in the FRF curves that this mode does not appear for either the experimental nor computational results, as will be seen by the lack of peaks around 115 Hz at Figure 22. The reason for this is the disposition of the sensor, which is incapable to detect torsional modes.

### 3.6.1.1. CASE STUDY 1: INFLUENCE OF THE PZT SENSOR

Firstly, the influence of the PZT sensor was analyzed by comparing the FRFs of the S1P0 (undamaged without PZT) to the S1P1 (undamaged with PZT). Ideally, the PZT sensor should have very little influence, because its presence is only to monitor the integrity of the joint.

Based on the experimental curves presented at Figure 20, it can be noticed that the PZT sensor causes little influence in the dynamic behavior of the structure, considering the interest range of frequencies. However, there is an increment of the frequency for the 4th

flexural mode, and shifts of the phase angles for the frequency range close to the 3rd flexural mode. This is due to the very low mass and localized stiffness induced by the PZT sensor.

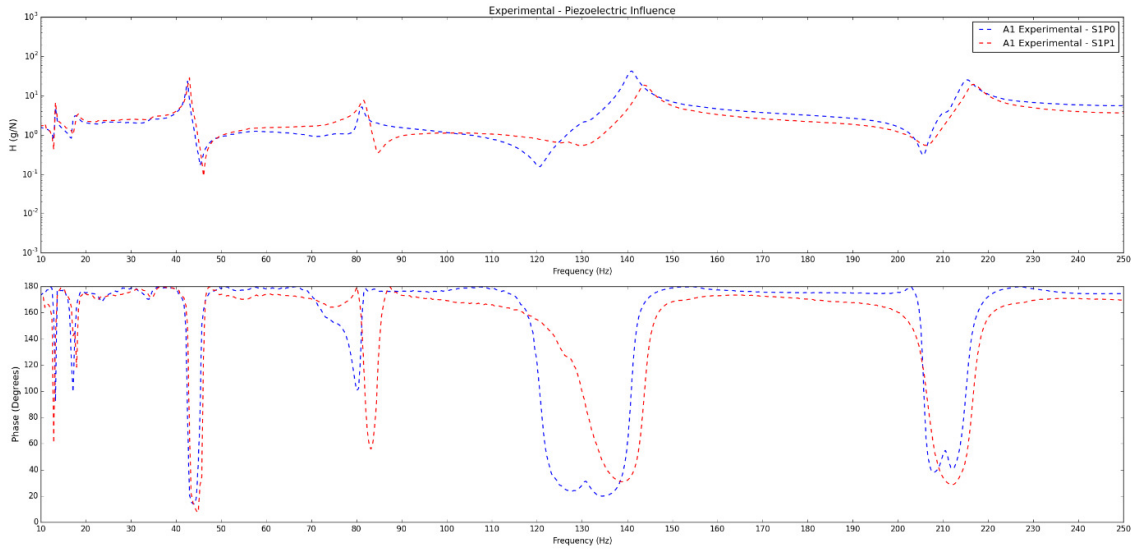


Figure 20. Experimental: Influence of the PZT sensor - Bonded Joint – free-free - A1.

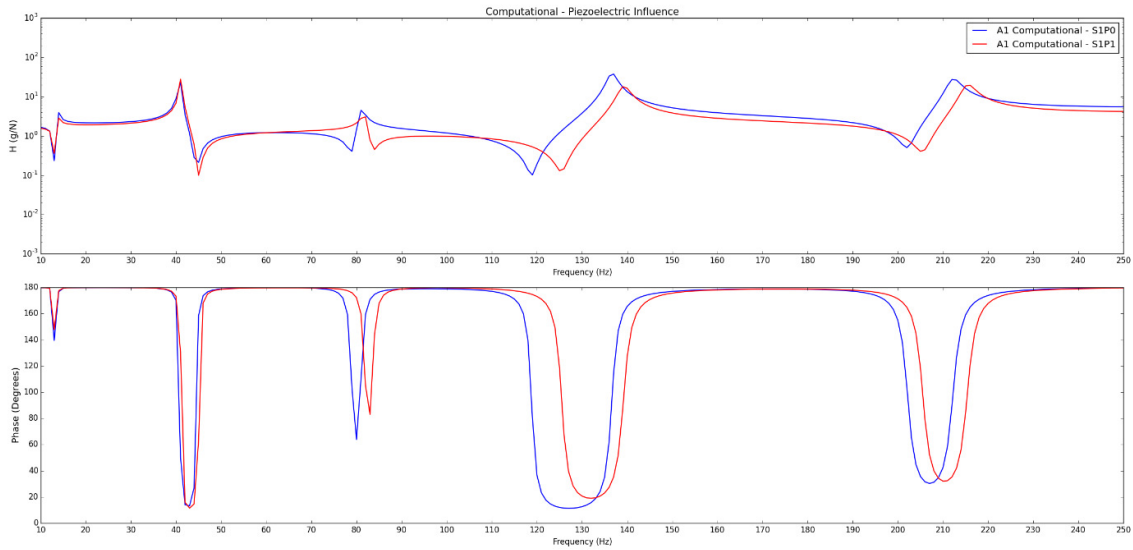


Figure 21. Computational: Influence of the PZT sensor - Bonded Joint - free-free - A1.

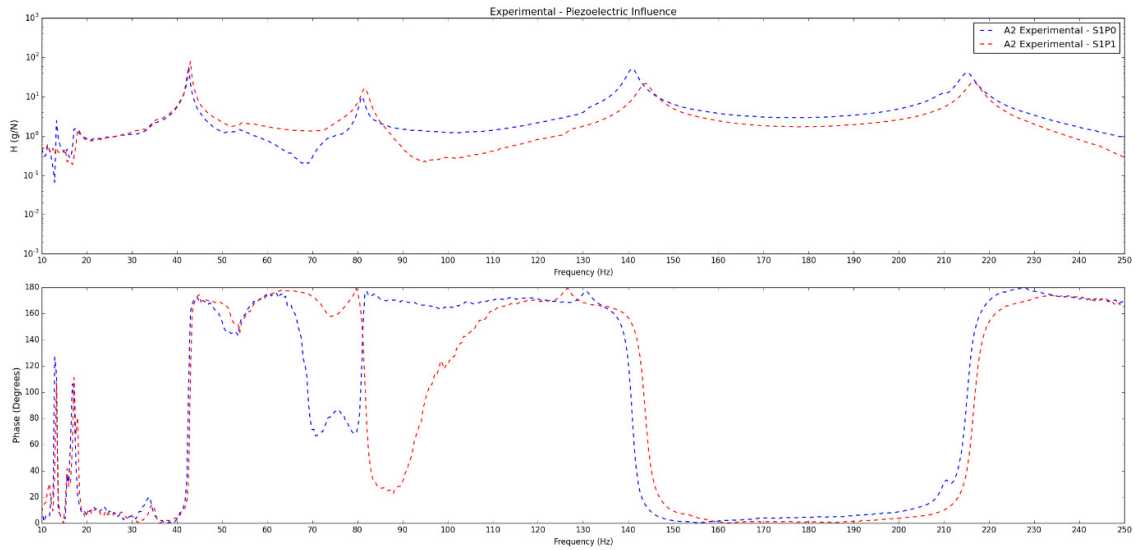


Figure 22. Experimental: Influence of the PZT sensor - Bonded Joint - free-free - A2.

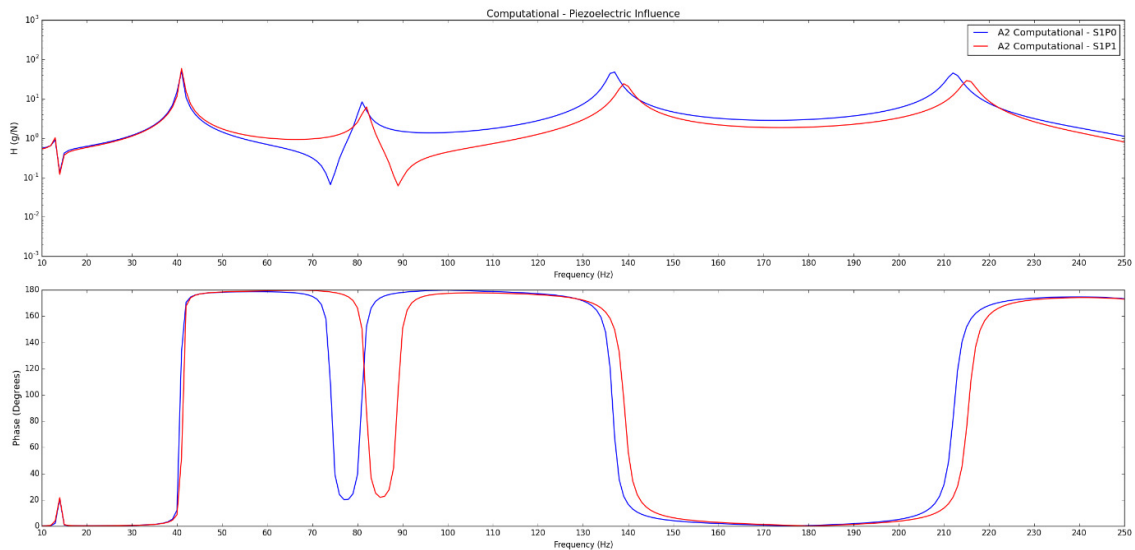


Figure 23. Computational: Influence of the PZT sensor - Bonded Joint - free-free - A2.

The flexural modes presented at Table 10 which were obtained via FEA - can be seen in the experimental FRF curves (Figure 20) such as the peaks at 14 Hz, 40 Hz and 134 Hz. By analyzing Figure 21, it can be noticed that FEA have shown similar results when compared to experimental FRFs. The computational models have also lower stiffness, which is represented by the lower values of natural frequencies as shown in Figure 24 and 23.

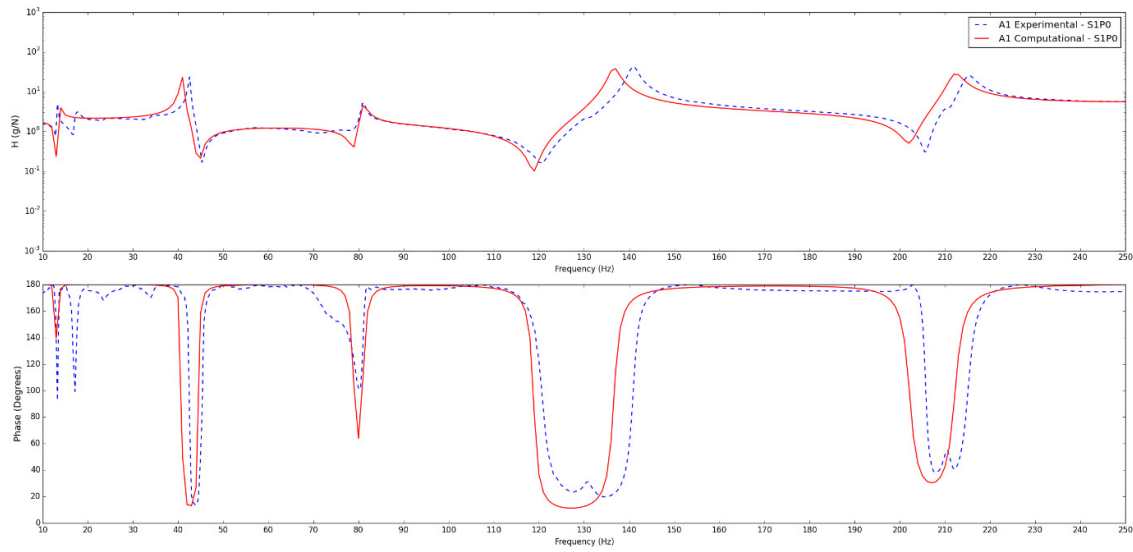


Figure 24. Comparison: Computational vs. Experimental FRF  $H_{12}$  S1P0 (free-free condition).

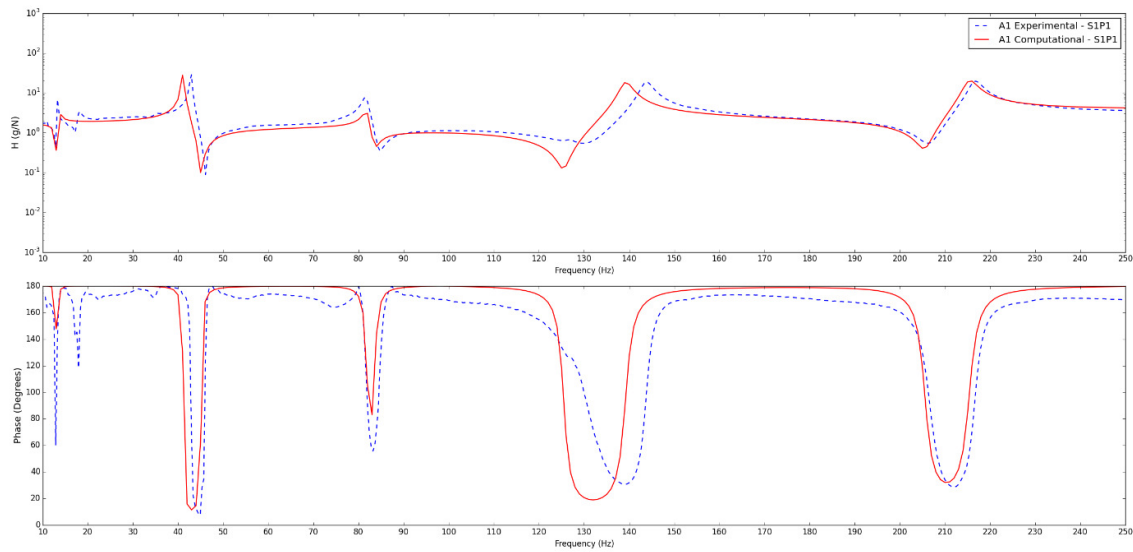


Figure 25. Comparison: Computational vs. Experimental FRF  $H_{12}$  S1P1 (free-free condition).

The natural frequencies obtained computationally are compared to the equivalent experimental values. This study was performed in accordance to Eq. (38) and the results are shown at Table 11.

Table 11. Comparison: Computational vs. Experimental FRF  $H_{12}$  – free-free.

Mode	Experimental [Hz]	Computational [Hz]	$\Delta$
1st Flexural	13.28	13.22	0.45%
2nd Flexural	42.58	39.59	7.02%
3rd Flexural	82.11	79.66	2.98%
4th Flexural	141.12	134.4	4.76%

$$\Delta = \left| \frac{F_E - F_C}{F_E} \right| * 100\% \quad (38)$$

### 3.6.1.2. CASE STUDY 2: INFLUENCE OF THE DAMAGE

Upon analyzing the FRFs to verify the influence of the debonding damage, it has been noticed a considerable reduction of the natural frequency for the 3rd flexural mode when compared to the other modal peaks, as shown in Figures 30 to .33 The reason for this is the greater displacements imposed of the overlap area due at the third flexural modal shape when compared to the others, as it can be seen in Figures 26 to 29.

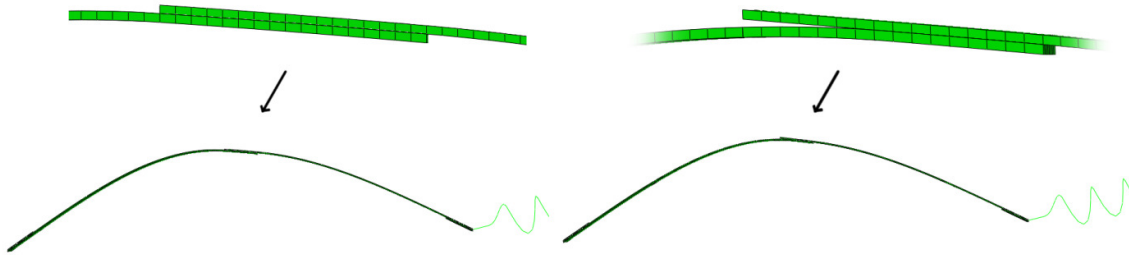


Figure 26. 1st Flexural Modal Shape: Undamaged vs. Damaged.

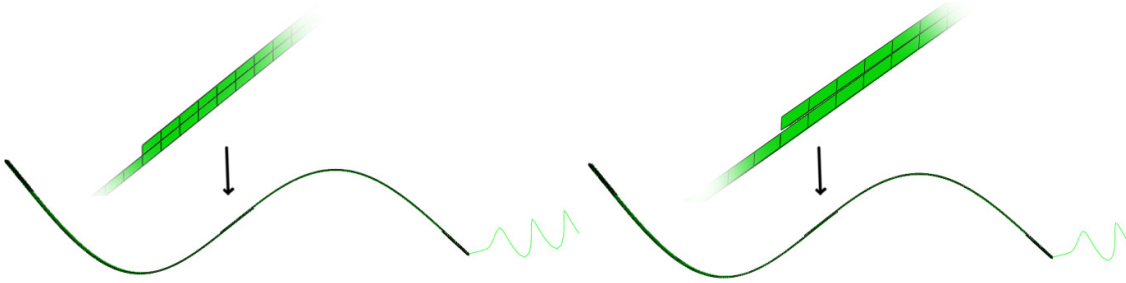


Figure 27. 2nd Flexural Modal Shape: Undamaged vs. Damaged.

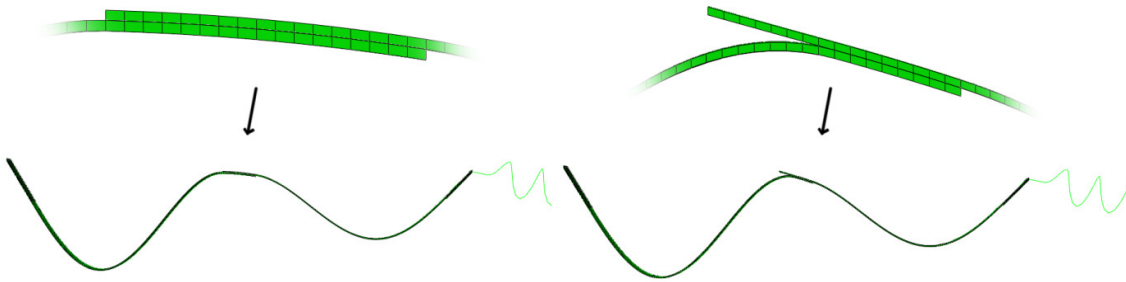


Figure 28. 3rd Flexural Modal Shape: Undamaged vs. Damaged.

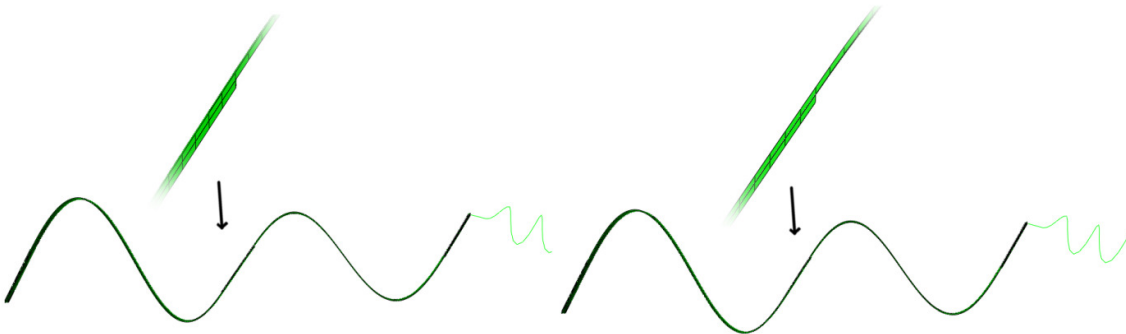


Figure 29. 4th Flexural Modal Shape: Undamaged vs. Damaged.

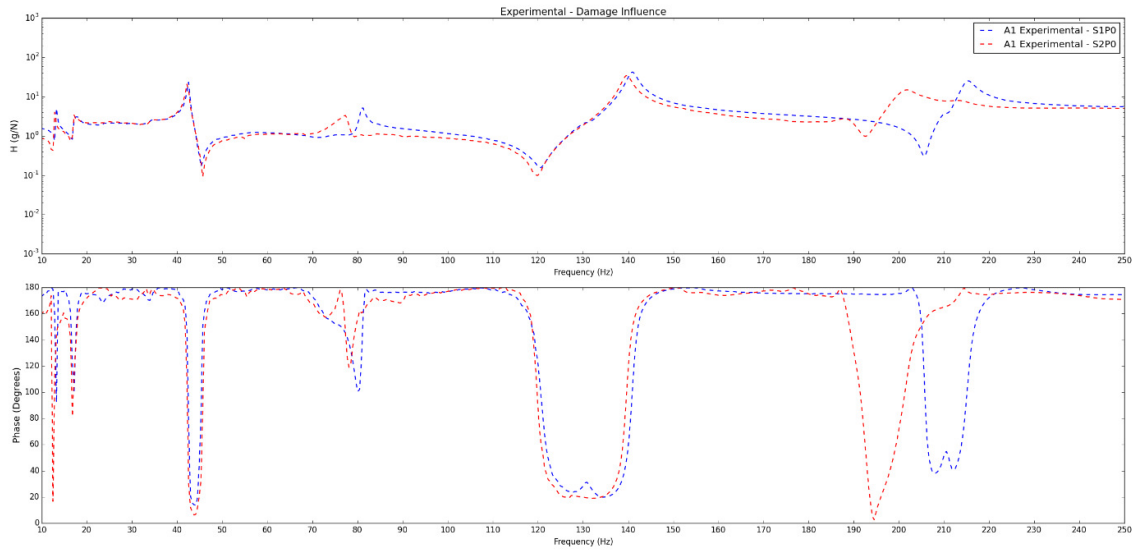


Figure 30. Experimental: Influence of Debonding Damage - Bonded Joint - free-free - A1.

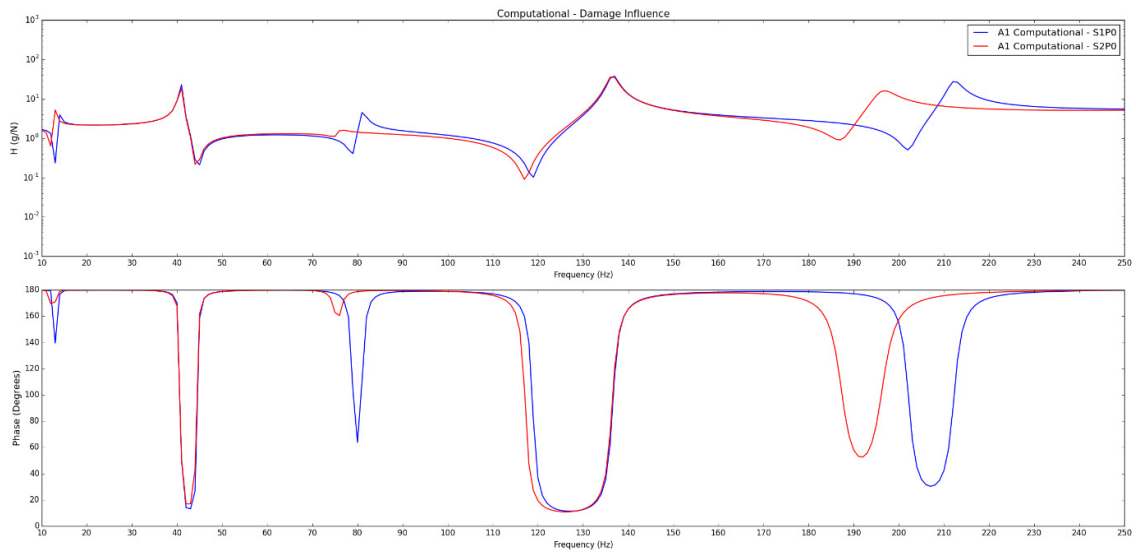


Figure 31. Computational: Influence of Debonding Damage - Bonded Joint - free-free - A1.

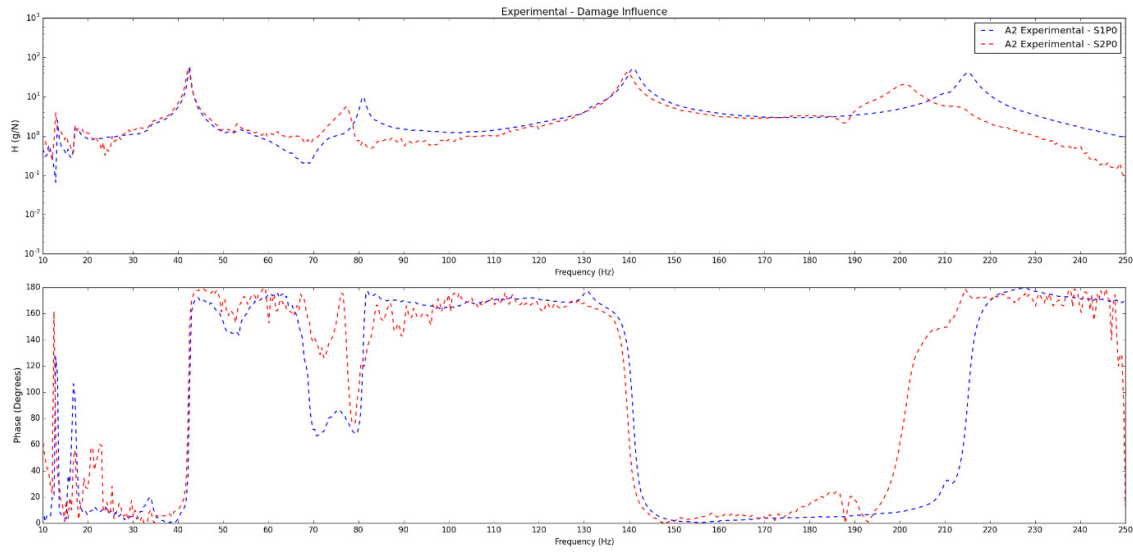


Figure 32. Experimental: Influence of Debonding Damage - Bonded Joint - free-free - A2.

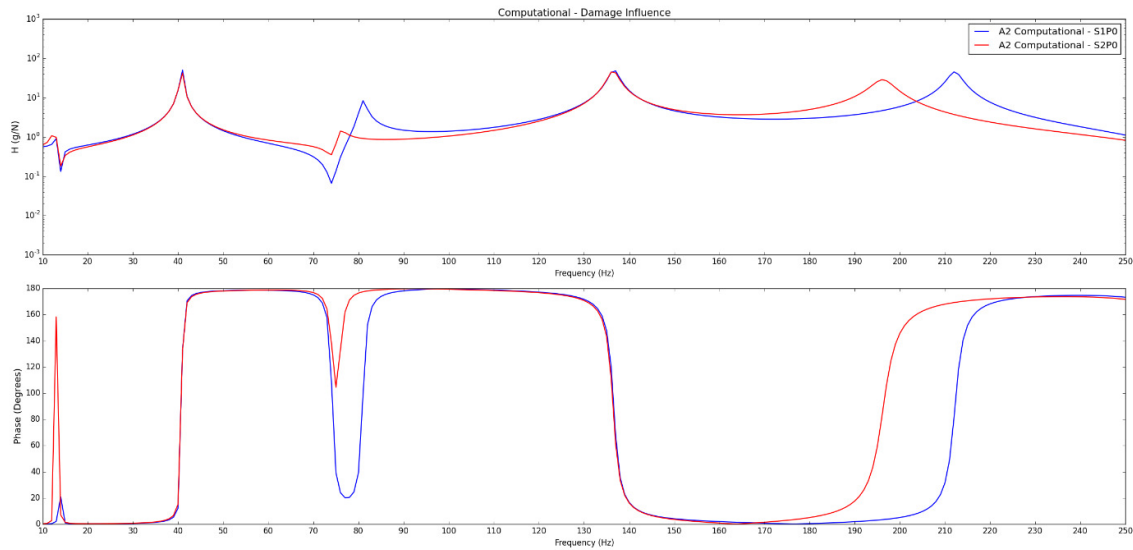


Figure 33. Computational: Influence of Debonding Damage - Bonded Joint - free-free - A2.

Metrics of Damage Quantification are ideal for objectively analyze the dynamic signatures for the purposes of diagnosis. Often the damages may be very small and unnoticeable by visually inspecting the FRF curves. The damage metrics applied were calculated via Equations (33) through (37) are exposed in Table 12.

Table 12. Mickens Damage Factors for Specimens without PZT - Bonded Joint - free-free.

<i>Computational Model</i>	<b>DF(Amplitude)</b>	<b>DF(Phase)</b>
H <sub>12</sub>	0.83	0.21
H <sub>13</sub>	0.51	3.33
<i>Experiments</i>		
H <sub>12</sub>	0.80	0.20
H <sub>13</sub>	0.65	1.65

Table 13. Modified Damage Factors for Specimens without PZT - Bonded Joint - free-free.

<i>Computational Model</i>	<b>DF(Amplitude)</b>	<b>DF(Phase)</b>
H <sub>12</sub>	0.11	0.09
H <sub>13</sub>	0.13	0.11
<i>Experiments</i>		
H <sub>12</sub>	0.12	0.11
H <sub>13</sub>	0.14	0.15

The new metrics present more stable results with both the Phase-based and Magnitude-based, following the same standard. Mickens' metric also provided reliable results for the Magnitude, but for Phase values, the metrics faces divisions by low numbers, corrupting the quantified damage.

### 3.6.1.3. CASE STUDY 3: DAMAGE IDENTIFICATION

Lastly, the same damage was inspected by analyzing the response of the PZT sensor. Tables 14 and 15 were created following the same procedure used for the specimens without PZT (Tables 12 and 13), with the additional element  $H_{14}$  which corresponds to the response of the PZT sensor.

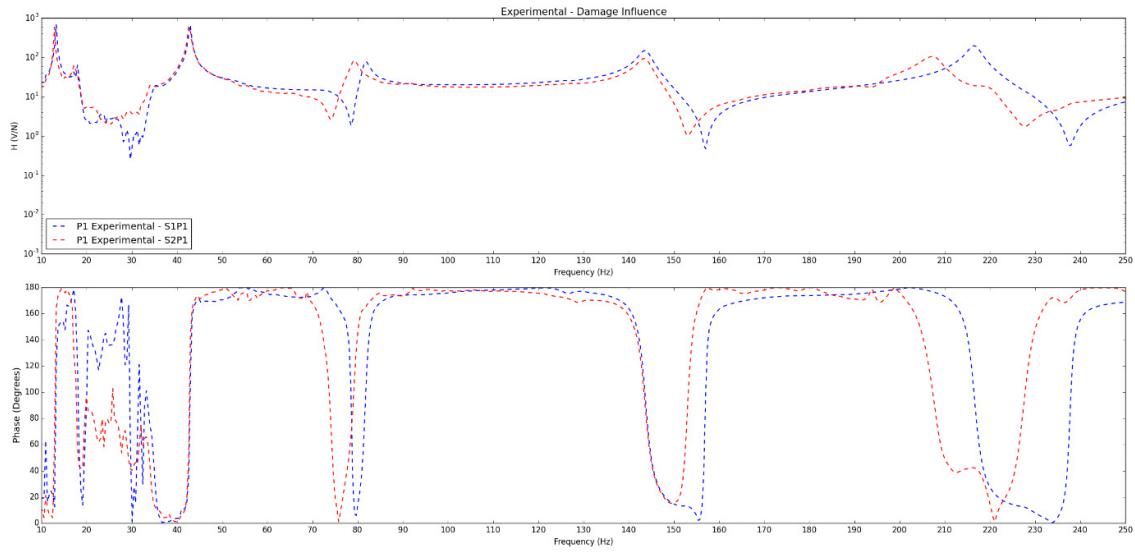


Figure 34. Experimental: Influence of the Damage - Bonded Joint - free-free - P1.

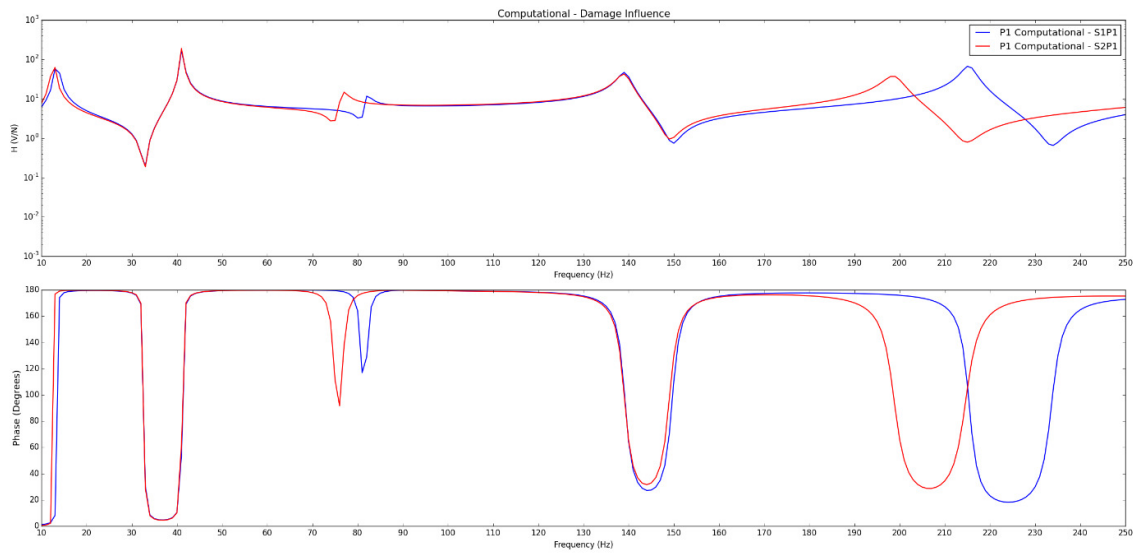


Figure 35. Computational: Influence of the Damage - Bonded Joint - free-free - P1.

Table 14. Mickens Damage Factors for Specimens with PZT - Bonded Joint - free-free.

<i>Computational Model</i>	<b>DF(Amplitude)</b>	<b>DF(Phase)</b>
H <sub>12</sub>	0.74	0.20
H <sub>13</sub>	0.53	2.93
H <sub>14</sub>	0.45	0.58
<i>Experiments</i>		
H <sub>12</sub>	0.63	0.21
H <sub>13</sub>	0.53	2.49
H <sub>14</sub>	0.79	2.93

Table 15. Modified Damage Factors for Specimens with PZT - Bonded Joint - free-free.

<i>Computational Model</i>	<b>DF(Amplitude)</b>	<b>DF(Phase)</b>
H <sub>12</sub>	0.11	0.09
H <sub>13</sub>	0.14	0.12
H <sub>14</sub>	0.13	0.14
<i>Experiments</i>		
H <sub>12</sub>	0.12	0.12
H <sub>13</sub>	0.14	0.20
H <sub>14</sub>	0.12	0.19

The relative difference, Tables 16 and 17, was calculated in accordance to Eq. (39), where  $DF_a$  corresponds to the Damage Factor calculated on specimen S2P0 (damaged without PZT), and  $DF_b$  corresponds to the specimen S2P1 (damaged with PZT). It can be noticed that the variation of the Damage Factor for the magnitude based method is overall more stable to the influence of the piezoelectric sensor when compared to the phase based method.

$$R = \left| \frac{DF_b - DF_a}{DF_a} \right| * 100\% \quad (39)$$

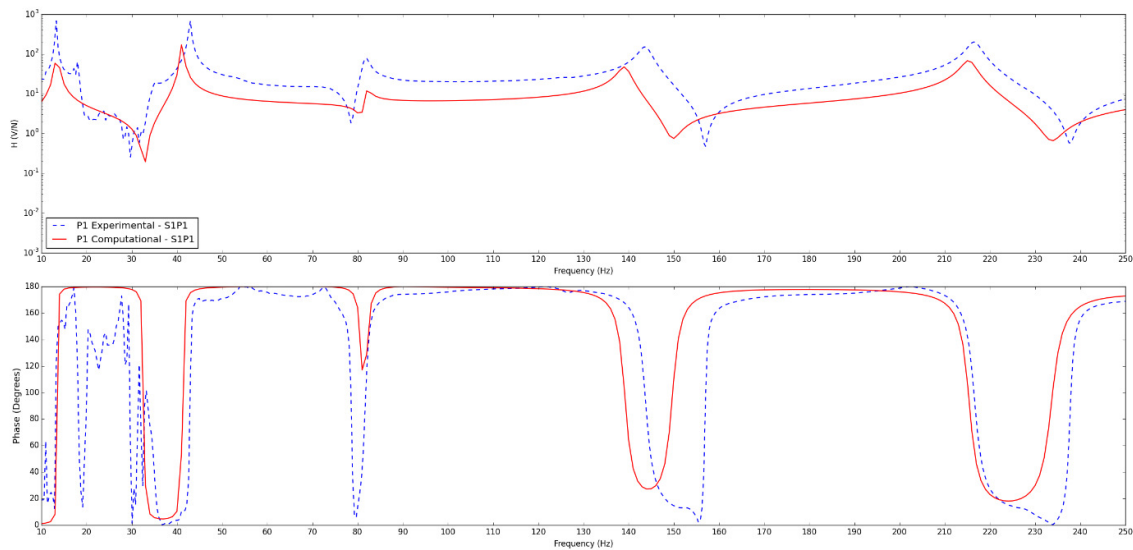
Table 16. Relative Difference between Damage Factors - free-free – Mickens.

<i>Computational Model</i>	<b>Amplitude</b>	<b>Phase</b>
$H_{12}$	10.84%	4.76%
$H_{13}$	3.92%	12.01%
<i>Experiments</i>		
$H_{12}$	21.25%	5.00%
$H_{13}$	18.46%	50.91%

Table 17. Relative Difference between Damage Factors - free-free – Modified.

<i>Computational Model</i>	<b>Amplitude</b>	<b>Phase</b>
$H_{12}$	0.00%	0.00%
$H_{13}$	7.69%	9.09%
<i>Experiments</i>		
$H_{12}$	0.00%	9.09%
$H_{13}$	0.00%	33.33%

Lastly, by comparing the FRFs of the computational and experimental piezoelectric responses - Figure 36 and Figure 37 - it can be noticed that the curves shown similar behavior, with the exception of the lower frequencies, which present a noisy response for the experimental data.

Figure 36. Comparison: Computational vs. Experimental FRF  $H_{14}$  S1P1 ( free-free condition).

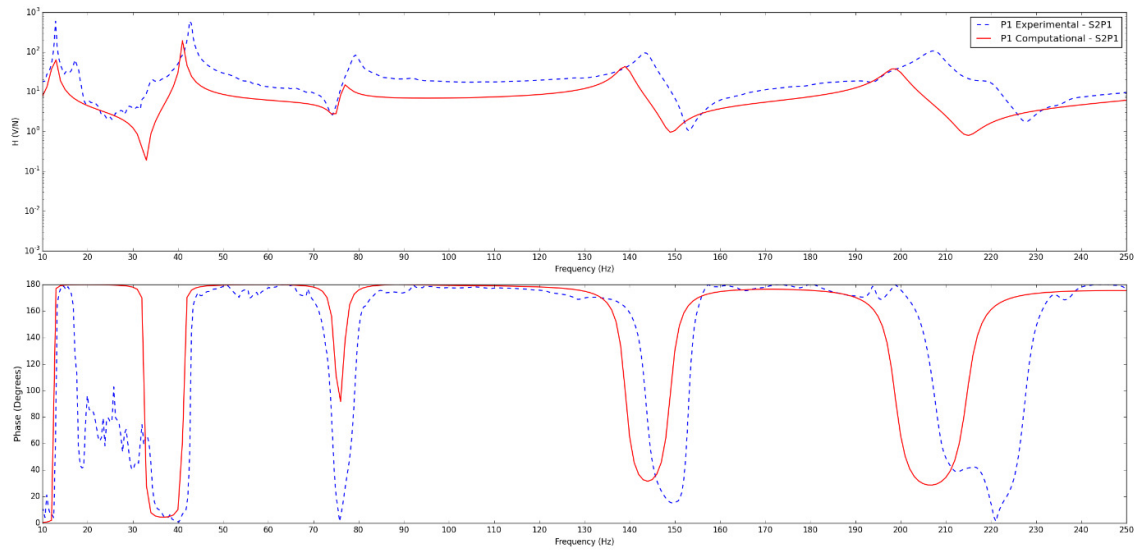


Figure 37. Comparison: Computational vs. Experimental FRF  $H_{14}$  S2P1 (free-free condition).

### 3.6.2. BICLAMPED BOUNDARY CONDITION

Similarly to what has been done at the development of the free-free FEMs, the computational models for the biclamped condition also considered the modal damping factor, which were calculated based on the experimental FRFs of the specimens (Figure 39). The damping factors are presented at Tables 18 through 21.

Table 18. Critical Damping Factors for Specimen 1 – biclamped.

Frequency [Hz]	Critical Damping Factor
60.35	0.00244
142.18	0.00220
217.31	0.00307
310.53	0.00266
431.78	0.00226

Table 19. Critical Damping Factors for Specimen 2 – biclamped.

<b>Frequency [Hz]</b>	<b>Critical Damping Factor</b>
59.20	0.00188
139.08	0.00349
206.58	0.00450
298.87	0.00409
407.33	0.00517

Table 20. Critical Damping Factors for Specimen 3 – biclamped.

<b>Frequency [Hz]</b>	<b>Critical Damping Factor</b>
59.74	0.00454
140.19	0.00588
214.13	0.00393
304.24	0.00489
424.33	0.00299

Table 21. Critical Damping Factors for Specimen 4 – biclamped.

<b>Frequency [Hz]</b>	<b>Critical Damping Factor</b>
59.75	0.00401
139.64	0.00389
208.96	0.00551
295.83	0.00859
413.00	0.00548

After that, it was necessary to identify the range of frequencies, which have the first non-rigid vibration modes. A way to do this is by analyzing the vibration modes provided by the “Frequency step”. As explained earlier, it is important to find the range of frequencies, which contains the first few flexible modes of the structure. To estimate this frequency range, studies were carried out for the specimen 1. The first 4 flexural modes of the biclamped specimen 1 are below the range of 350 Hz as shown in Table 22. A minimum frequency of interest was set at 50 Hz in order to avoid experimental noises, which are intense for lower frequencies.

Table 22. Modal Analysis for bonded joints - Numerical Modal frequencies for S1P0 - biclamped.

Mode	Frequency [Hz]
1 <sup>st</sup> Flexural	60.55
2 <sup>nd</sup> Flexural	141.10
3 <sup>rd</sup> Flexural	214.38
1 <sup>st</sup> Torsional	231.74
4 <sup>th</sup> Flexural	302.03

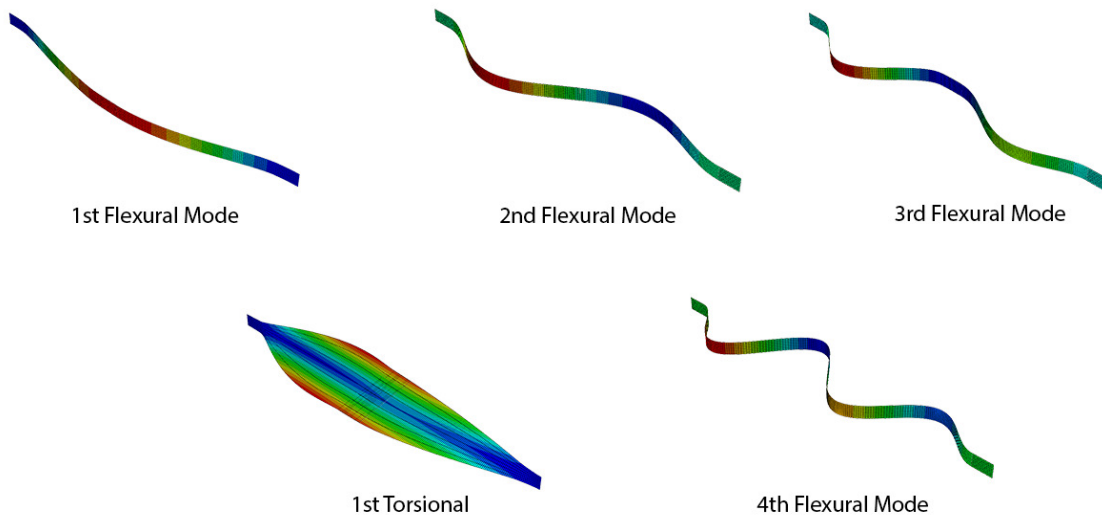


Figure 38. The first non-rigid mode shapes for the undamaged bonded joint - biclamped.

To evaluate the FEM for the biclamped condition, the values for the natural frequencies were compared to the ones obtained by the experiments (Figure 39). The results are shown at Table 23, and they prove that the computational model is reliable for simulating the experiments.

Table 23. Comparison: Computational vs. Experimental FRF  $H_{13}$  – biclamped.

Mode	Experimental [Hz]	Computational [Hz]	$\Delta$
1st Flexural	60.5	60.55	-0.08%
2nd Flexural	141.5	141.1	0.28%
3rd Flexural	217.5	214.38	1.43%
4th Flexural	311.0	302.03	2.88%

### 3.6.2.1. CASE STUDY 1: INFLUENCE OF THE PZT SENSOR

Following the procedures adopted for the free-free condition, the first analysis verifies the influence of the PZT sensor on the dynamic signature. As it can be seen in Figure 39, the influence consists on a small reduction of the natural frequencies, and this effect is stronger for higher frequencies.

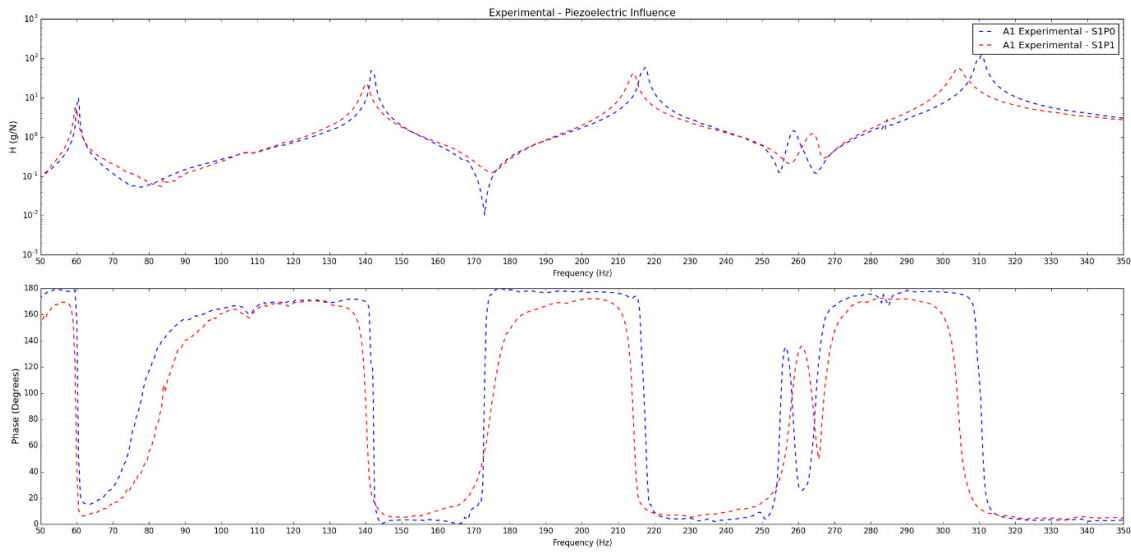


Figure 39. Experimental: Influence of the PZT sensor - Bonded Joint - biclamped - A1.

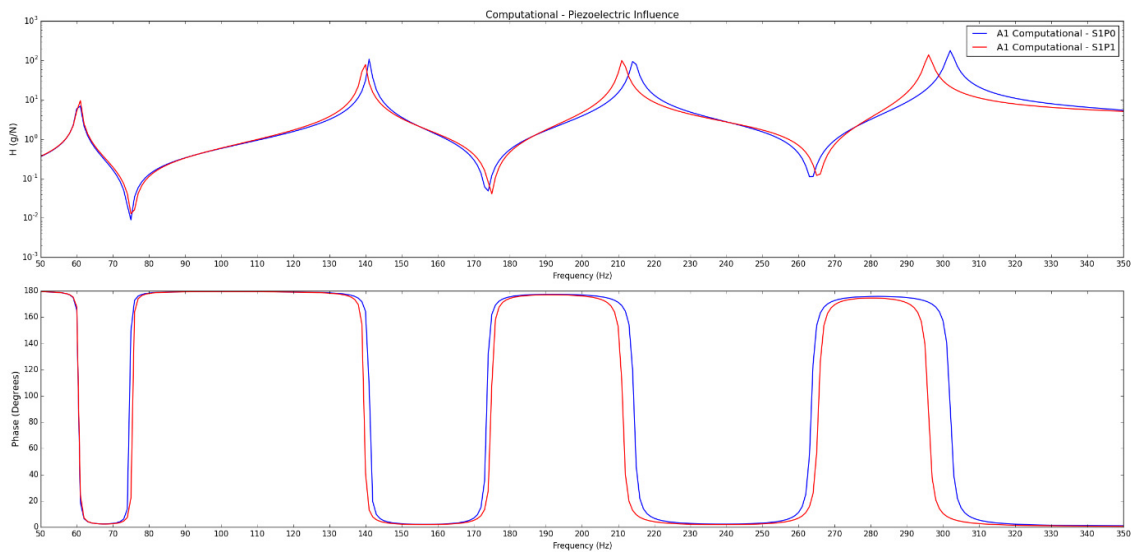


Figure 40. Computational: Influence of the PZT sensor - Bonded Joint - biclamped - A1.

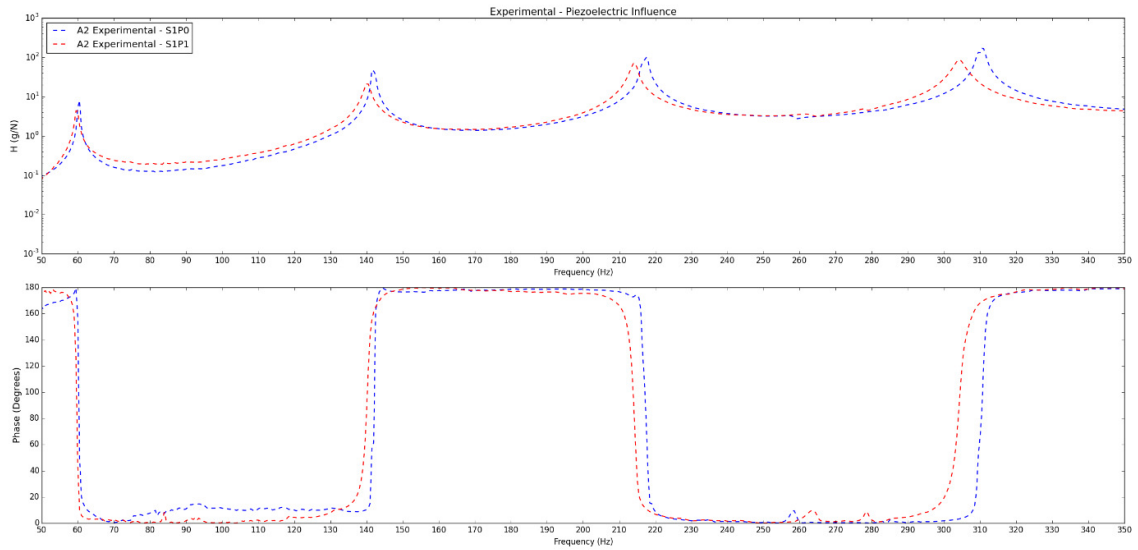


Figure 41. Experimental: Influence of the PZT sensor - Bonded Joint - biclamped - A2.

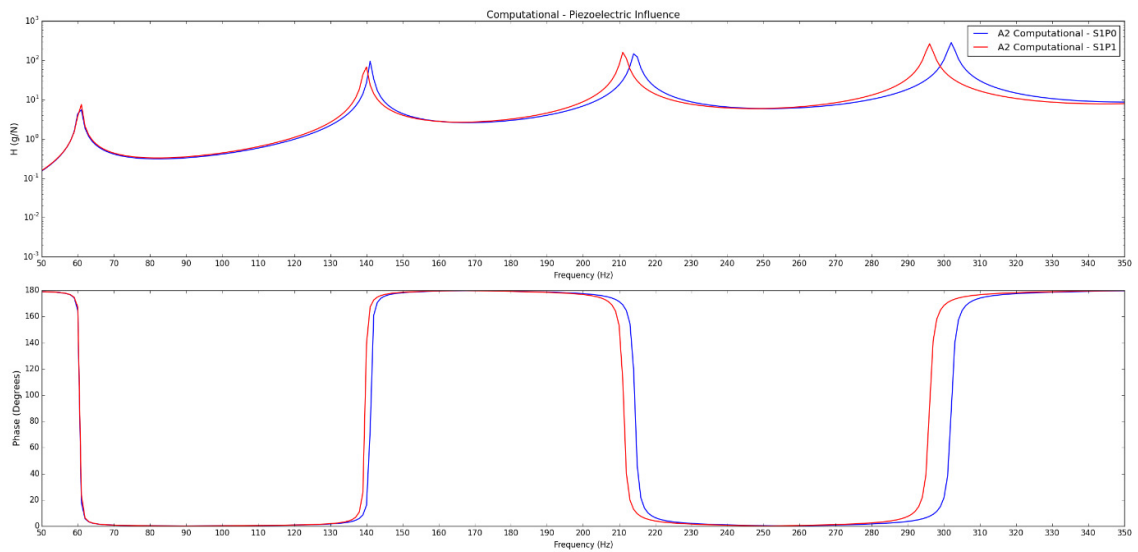


Figure 42. Computational: Influence of the PZT sensor - Bonded Joint - biclamped - A2.

### 3.6.2.2. CASE STUDY 2: INFLUENCE OF THE DAMAGE

Similarly to the free-free condition results, the presence of debonding damage caused a reduction of joint stiffness, and the results are shown in Figure 43. The damage factors for biclamped boundary condition are higher than the ones obtained for free-free condition.

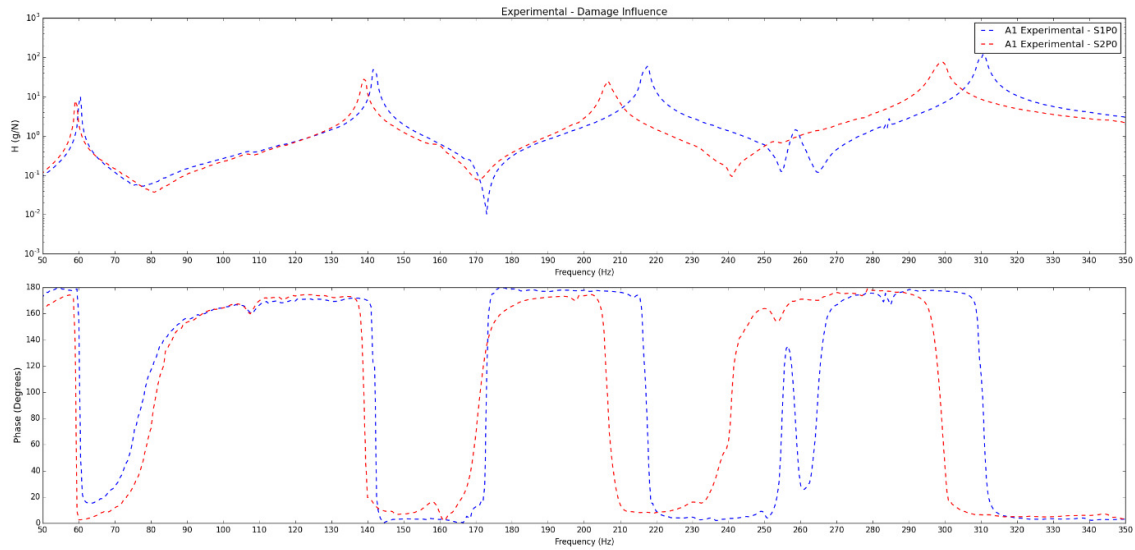


Figure 43. Experimental: Influence of Damage - Bonded Joint - biclamped - A1.

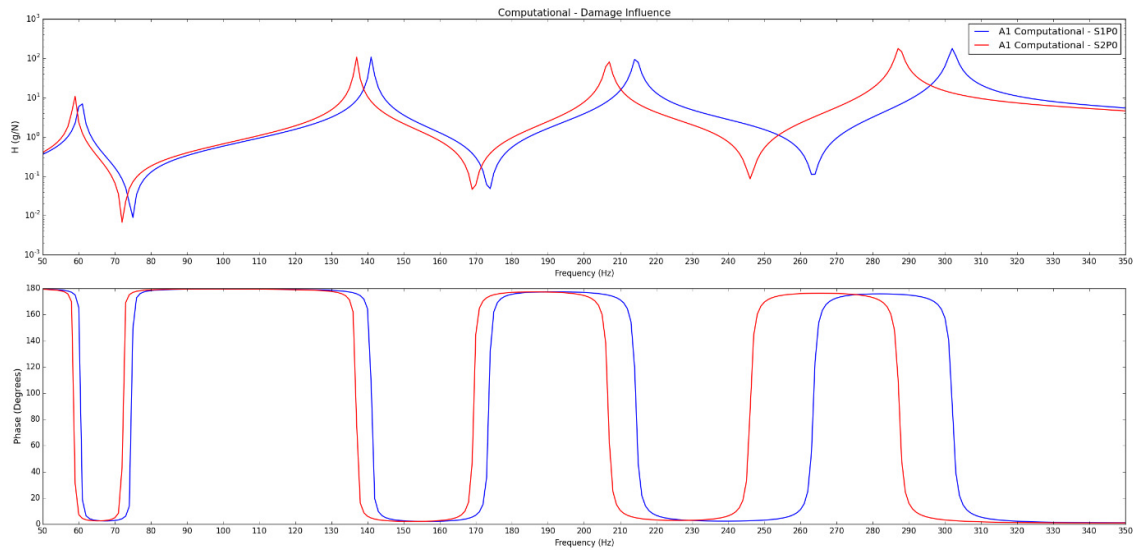


Figure 44. Computational: Influence of Damage - Bonded Joint - biclamped - A1.

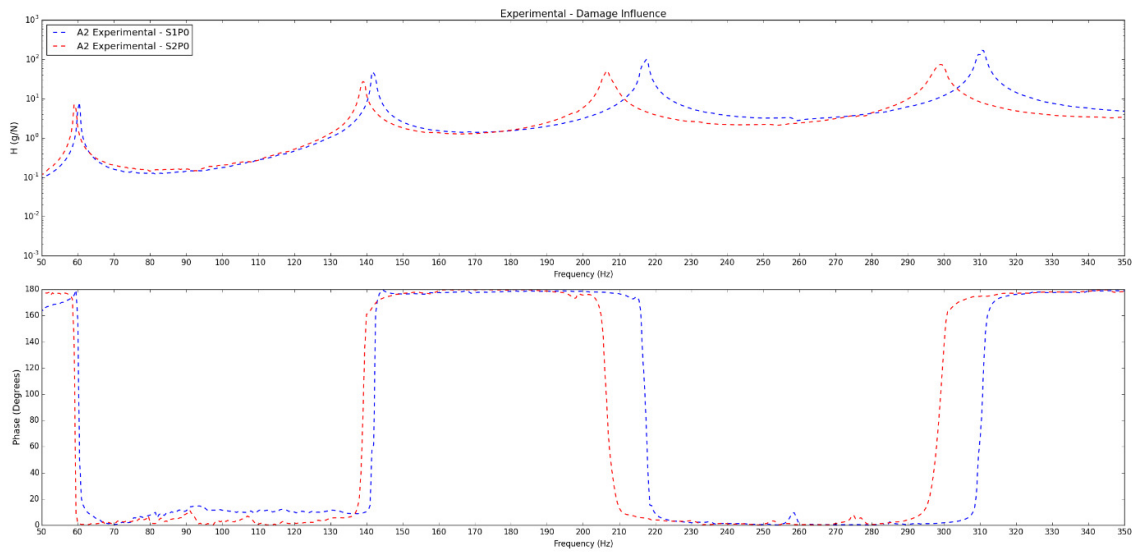


Figure 45. Experimental: Influence of Damage - Bonded Joint - biclamped - A2.

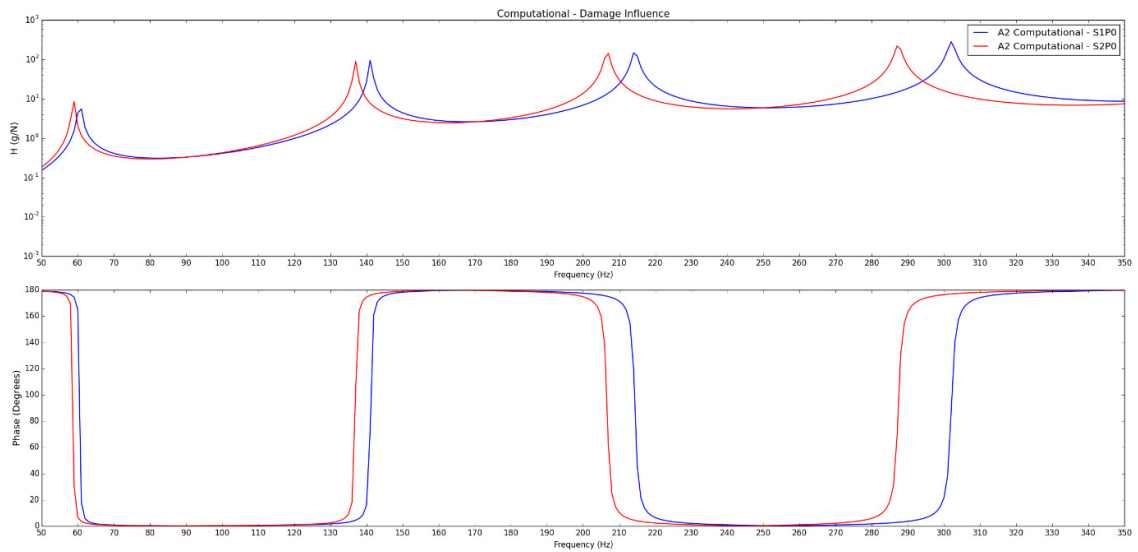


Figure 46. Computational: Influence of Damage - Bonded Joint - biclamped - A2.

The damage factors were calculated following the procedures mentioned in the free-free analysis, and they are presented at Tables 24 to 25 (for the specimen without PZT sensor) and Tables 26 to 27 (for the specimen with PZT sensor).

Table 24. Mickens Damage Factors for specimens without PZT - Bonded Joint – biclamped.

<i>Computational Model</i>	<b>DF(Amplitude)</b>	<b>DF(Phase)</b>
H <sub>12</sub>	1.63	2.76
H <sub>13</sub>	0.68	2.44
<i>Experiments</i>		
H <sub>12</sub>	1.04	2.52
H <sub>13</sub>	0.57	3.27

Table 25. Modified Damage Factors for specimens without PZT - Bonded Joint – biclamped.

<i>Computational Model</i>	<b>DF(Amplitude)</b>	<b>DF(Phase)</b>
H <sub>12</sub>	0.21	0.19
H <sub>13</sub>	0.20	0.11
<i>Experiments</i>		
H <sub>12</sub>	0.21	0.22
H <sub>13</sub>	0.20	0.10

### 3.6.2.3. CASE STUDY 3: DAMAGE IDENTIFICATION

Once again, the same procedures, which were performed for the free-free condition analyses, are repeated for the biclamped. The piezoelectric sensor behaved as expected and provided dynamic signatures similar to the ones obtained by the accelerometers.

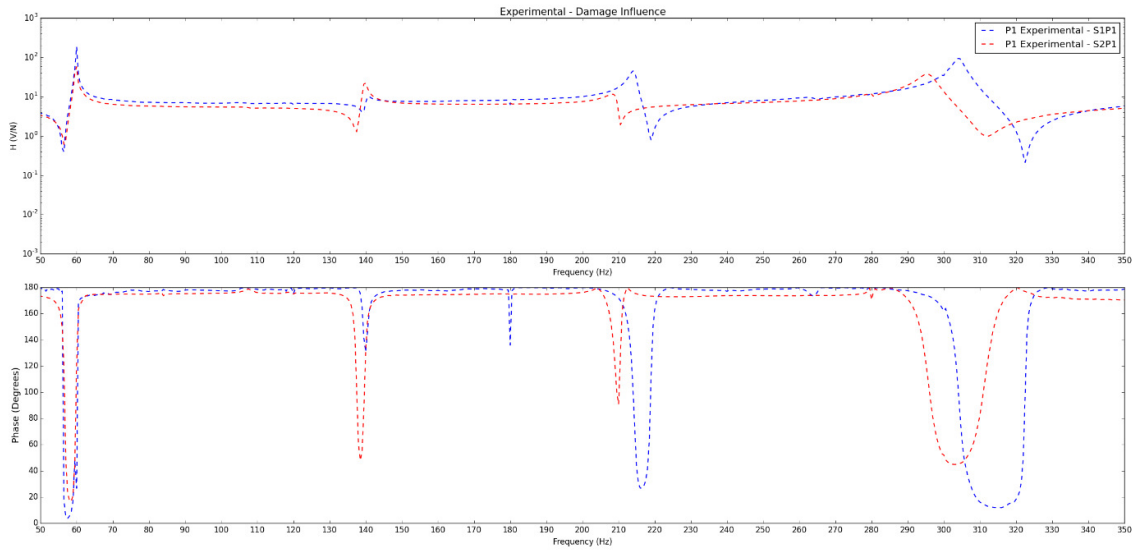


Figure 47. Experimental: Influence of the Damage - Bonded Joint - biclamped - P1.

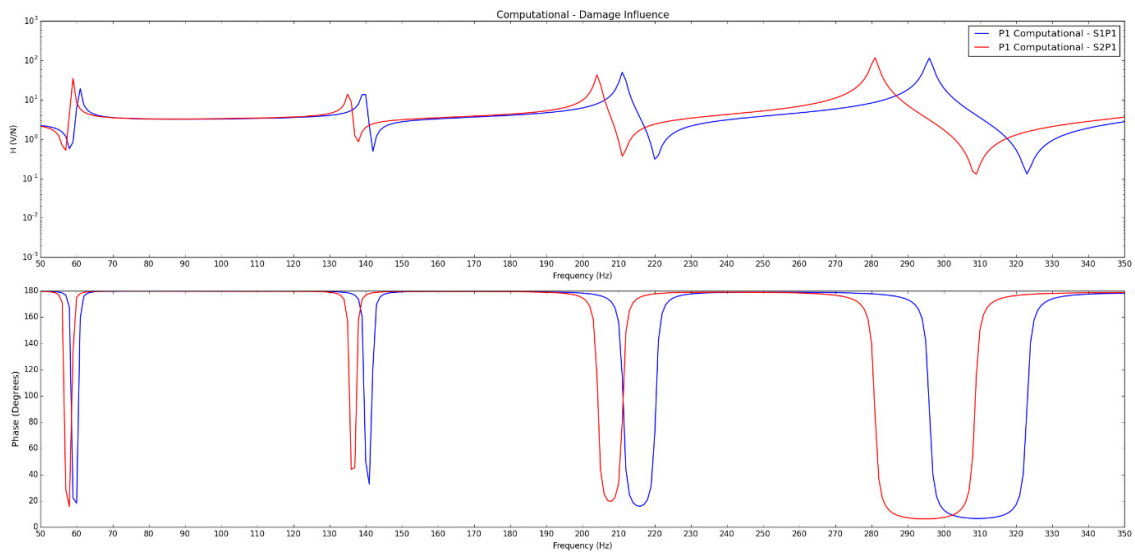


Figure 48. Computational: Influence of the Damage - Bonded Joint - biclamped - P1.

The damage metrics are more sensible to the shift of natural frequencies when they are based on Phase. The larger shifts caused in the biclamped condition explains the discrepancy between the Damage Factors obtained by phase when compared to the Magnitude-based ones.

Table 26. Mickens Damage Factors for Specimens with PZT - Bonded Joint – biclamped.

<i>Computational Model</i>	<b>DF(Amplitude)</b>	<b>DF(Phase)</b>
H <sub>12</sub>	1.82	3.09
H <sub>13</sub>	0.67	2.50
H <sub>14</sub>	0.89	1.19
<i>Experiments</i>		
H <sub>12</sub>	3.09	1.05
H <sub>13</sub>	2.50	3.35
H <sub>14</sub>	1.19	0.57

Table 27. Modified Damage Factors for Specimens with PZT - Bonded Joint – biclamped.

<i>Computational Model</i>	<b>DF(Amplitude)</b>	<b>DF(Phase)</b>
H <sub>12</sub>	0.21	0.19
H <sub>13</sub>	0.20	0.11
H <sub>14</sub>	0.19	0.19
<i>Experiments</i>		
H <sub>12</sub>	0.15	0.18
H <sub>13</sub>	0.14	0.07
H <sub>14</sub>	0.10	0.11

In this case, the magnitude based damage factors provided results that were more unstable than the ones obtained via the phase angle method, as shown at Table 28. This instability was mitigated by the use of the filtering methodology proposed to the metrics, and the results are shown in Table 29.

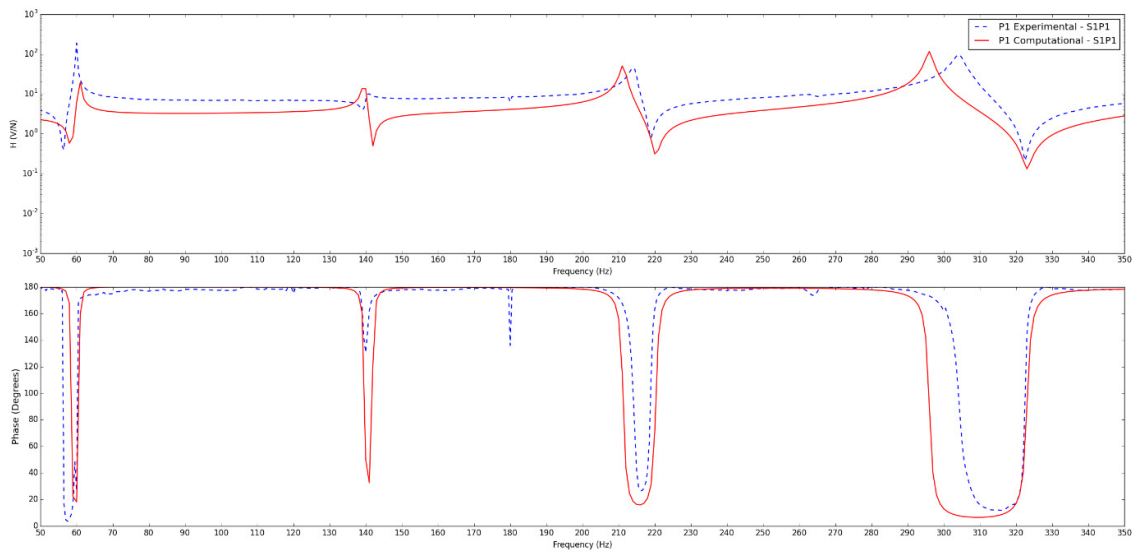
Table 28. Relative Difference between Damage Factors - biclamped – Mickens.

<i>Computational Model</i>	<b>Amplitude</b>	<b>Phase</b>
H <sub>12</sub>	11.66%	11.96%
H <sub>13</sub>	1.47%	2.46%
<i>Experiments</i>		
H <sub>12</sub>	197.12%	58.33%
H <sub>13</sub>	338.60%	2.45%

Table 29. Relative Difference between Damage Factors - biclamped – Modified.

<i>Computational Model</i>	<b>Amplitude</b>	<b>Phase</b>
H <sub>12</sub>	0.00%	0.00%
H <sub>13</sub>	0.00%	0.00%
<i>Experiments</i>		
H <sub>12</sub>	28.57%	18.18%
H <sub>13</sub>	30.00%	30.00%

Lastly, Figures 49 and 50 compare the results obtained experimentally by the data obtained via the computational models. The numerical analysis provided results with satisfactory convergence to the experimental data.

Figure 49. Comparison: Computational vs. Experimental FRF H<sub>14</sub> S1P1 (biclamped condition).

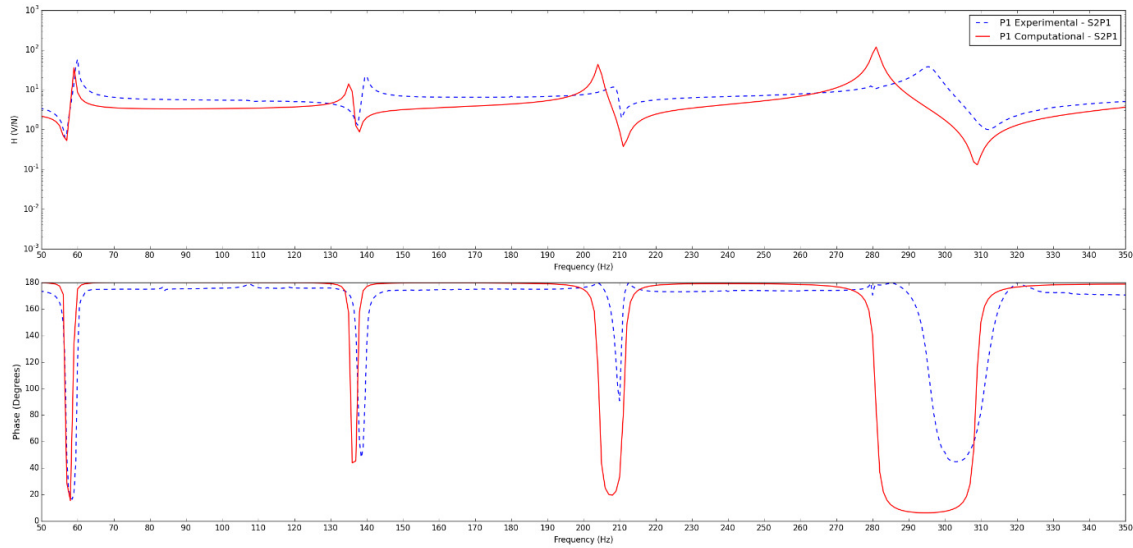


Figure 50. Comparison: Computational vs. Experimental FRF  $H_{14}$  S2P1 (biclamped condition).

### 3.7. CONSIDERATIONS

Refinements can be made in the computational models by inserting a better representation of the piezoelectric sensor. A possible approach to refine this element is the determination of the material properties. It is also possible to make use of User Elements (UEL), such as the one developed by Sartorato et al. (2013b), instead of using the standard element available in ABAQUS.

Both methods (Amplitude-based and Phase-based) of damage quantification applied in this work are heavily sensible to the frequency range of choice. Therefore, it is strategic to optimize the identification of debonding damage by proposing ways to narrow the frequency range of analysis in order to identify better this kind of failure.

The magnitude and phase based damage quantification methods seem to work well in pairs and the modifications implemented provided more stable results for the damage metrics. However, the present study is not able to properly judge those metrics. Future approaches should work with different extensions of damage to properly analyze how to evaluate the limitations and potentialities of each metric. For example, a new metal-composite bonded joint specimen with debonding damage over 25% of the overlap area could be investigated, comparing the present results.

## 4. SHM FOR SANDWICH STRUCTURES

---

---

### 4.2. REVIEW

Birman and Simonyan (1994) developed a thermoelastic theory for cylindrical sandwich shells with piezoelectric elements working as both sensors and actuators and placed inner and outer skins, exploring the application of the sensors to detect delamination damage. The authors concluded that even a very small dynamic excitation can induce significant piezoelectric response over the region with delamination, and at the same time, a small response at the undamaged region.

Lestari and Qiao (2004) used smart sensors to perform damage detection, location and quantification of damage based on curvature mode shapes. The authors used honeycomb sandwich beams made of glass fibers and polyester resin with the core in corrugated cells damaged and undamaged. The authors concluded that the methodology was a success, and it could be implemented in full-scale composite structures.

Orugandi et al. (2009) performed SHM on a sandwich structure composed by carbon fiber and epoxy resin for skins and honeycomb core. They used displacement and curvature mode shapes to monitor the structure. The publication also shows a small review on methodologies to identify damage.

Amir et al (2010) used the dynamic response of a honeycomb sandwich structure to detect multi-site damage (MSD). The authors determined variation of natural frequencies and variation of damping ratio to estimate the damage. The studies concluded that damping ratio was more reliable than natural frequency. The authors also discussed how low impact damage, such as dropped tools during maintenance, can cause small indentations in the structure. They highlighted that the use of natural frequency for detecting damage cannot reliably detect initial damages on the structures. Thus, for composite structures, the interest by the academy over the use of modal damping variation has increased since this criterion is more sensible to damage than stiffness. This is the reason that in the present work, it will be used variation of natural frequency combined to damage metrics.

Luchinsky et al (2011) used the Lamb Wave propagation technique to analyze the detection of impact damage on a SSHC (Sandwich Structure with Honeycomb Core) in aluminum. Numerical (FEM developed in ABAQUS) and experimental analyses were carried out. The authors concluded that flexural lamb waves are more sensitive to impact damage than symmetric lamb waves.

Masmoudi et al (2014) studied the influence of embedding a piezoelectric sensor in a sandwich beam made of PVC foam core and glass fiber/resin skins. The authors performed two kinds of experimental analyses for three different specimens. The first experiment was a three-point bending test, and the second one was a fatigue test. The first specimen did not have piezoelectric sensor, the second one had a small sensor and the last one had a large sensor. The authors concluded that the behavior of the three specimens was similar in the three-point bending test. However for the fatigue tests, the authors noticed that the fatigue curve for the specimen with the large embedded sensor had a much higher degradation rate, while the other two specimens had very similar curves. Thus the authors concluded that the size of the embedded sensor has significant influence on the lifetime and mechanical characteristics of the material under fatigue.

Dhamande and Bhaskar (2014) made use of the first three natural frequencies and mode shapes to detect and localize two types of damage - debonding and core crushing - in a honeycomb sandwich beam, which has core in aluminium and skins in CFRP. The authors concluded that the technique was a success, and that it is possible to obtain approximate crack locations by using frequency contour.

Based on the scenario approached above, this present work will also focus on SHM for sandwich structures based on difference of Frequency Response Functions aided by metrics for damage quantification.

### **4.3. SPECIFIC OBJECTIVES**

The main objective consists on contributing for the development of SHM systems based on vibration methods to be applied in sandwich structures. A complete SHM system is able to identify and to localize damage, as well as to evaluate the severity of the damage of

sandwich structures. However, the main objective of the present work is focused on the identification of the damage. Thus, it can be divided in different goals:

- ☑ Gather studies and results on the field of vibration based method for SHM on sandwich structures previously developed by the academy, giving more focus to those applied vibration based methods.
- ☑ Develop a preliminary computational model of the sandwich structure for undamaged condition. This model will work as reference for the development of the specimens (sandwich structures made of skins in epoxy resin reinforced by glass fiber and a core of PVC foam) used in the experimental analyses.
- ☑ Based on computational model of the undamaged sandwich structure, develop preliminary FE models of the sandwich structure with damage and/or presence of the piezoelectric sensor. Perform vibration experimental analyses on undamaged specimens of sandwich structures. The mode shapes, natural frequencies and overall dynamic signature will be compared to the computational results in order to evaluate the potentialities and limitations of FEM.
- ☑ Generate new sandwich structure models more refined due to the studies performed with the new acquired experimental data.
- ☑ Perform vibration experimental analyses on specimens of sandwich structure with damage and/or with PZT sensor. Compare the results to the computational data in order to evaluate the potentialities and limitations of the FEM.
- ☑ Calculate Damage Metrics by using Frequency Response Functions obtained from computational and experimental analyses.

## 4.4. EXPERIMENTS

### 4.4.1. MATERIALS AND SPECIMENS

The sandwich structures were made of glass fiber/epoxy skins and PVC foam core. The specimens have 3 output regions, 1 input point and 1 damage area. The dimensions for the specimens are displayed at Figure 51. As noted in the schema, the points 2 and 3 will have accelerometers for some specimens and MFCs for others. Region 4 is the area of damage, which was created via the same process used for the bonded joint specimens with debonding at overlap area. Lastly, point 5 will have always an accelerometer, which is considered as a reference point.

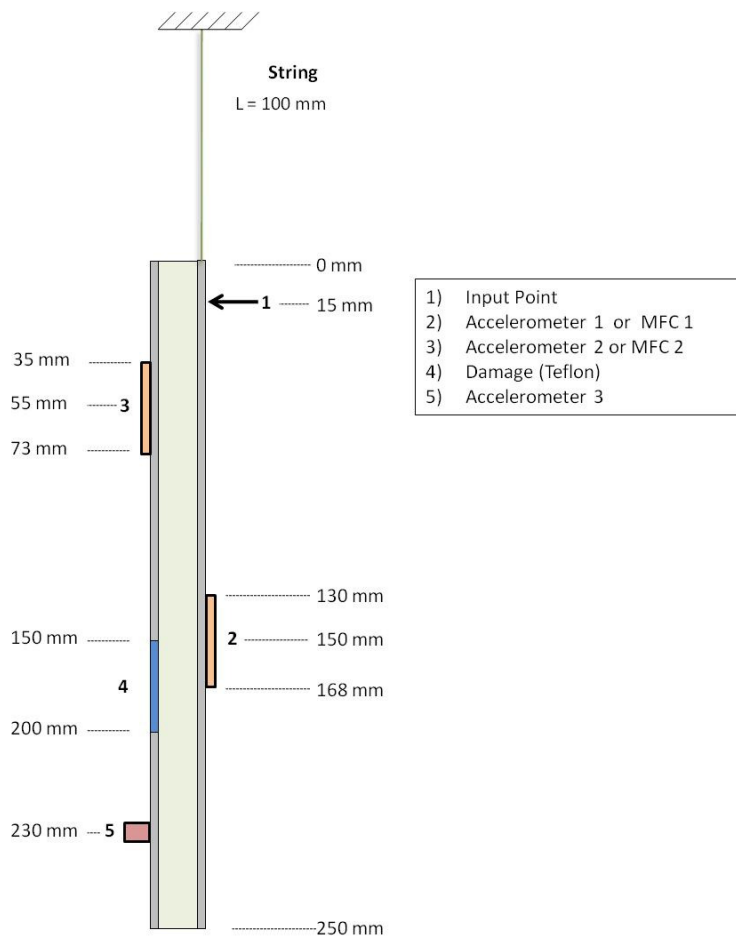


Figure 51. Sandwich structure specimens.

The skin was a laminate made of unidirectional glass fibers and epoxy Araldite Ly 1564 BR resin catalyzed by REN Hy 150 BR. The plies were stacked as  $[0^\circ, +45^\circ, -45^\circ]_5$  configuration. This composite material was manufactured at Laboratory of Aeronautic Structures (University of São Paulo). They were produced by laying up dry fibers on top of a flat glass mould in accordance to the stacking sequence, vide Figure 52. The resin was applied by using Vacuum and it was cured under  $25^\circ\text{C}$  for 12 hours, as shown in Figure 53. The mechanical properties of the skins were not obtained experimentally, for that reason, values used in the computational analyses were found in the literature (SINGH; TALREJA, 2010). These values are shown in Table 30.

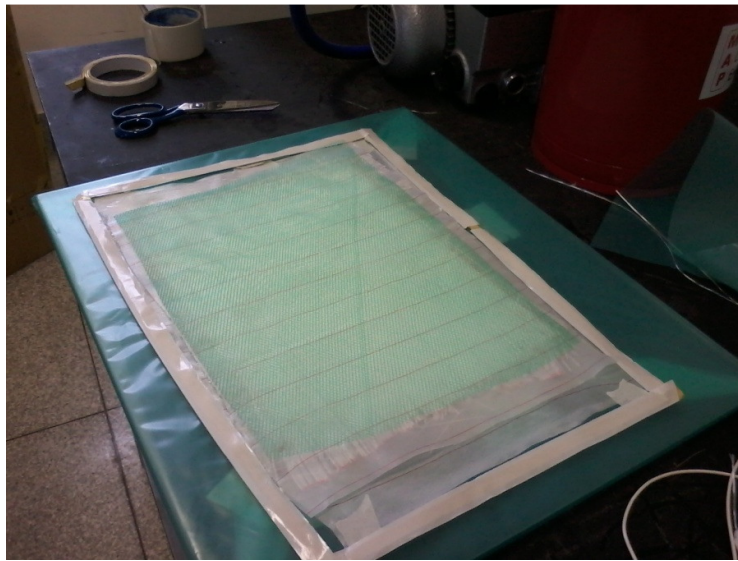


Figure 52. Lay-up of dry fibers for the Skins of the Sandwich Structure.



Figure 53. Manufacturing process of the Skins

Table 30. Skin properties.

<b>Properties</b>	<b>Unit</b>	<b>Value</b>
$E_{11}$	GPa	44.80
$E_{22}$	GPa	11.30
$E_{33}$	GPa	11.30
$G_{13}$	GPa	4.86
$G_{23}$	GPa	4.45
$G_{12}$	GPa	4.86
$\nu_{12}$	-	0.28
$\nu_{13}$	-	0.28
$\nu_{23}$	-	0.28
$\rho$	Kg/m <sup>3</sup>	1580

The core was made of PVC foam H60 from Divinicell, which is commonly used by the aeronautical industry. In fact, the elastic properties and strength values under tension and compression were determined by Caliri Júnior (2010) and it is shown at Table 31.

Table 31. PVC foam core elastic properties.

<b>Properties</b>	<b>Unit</b>	<b>Value</b>
$E_{11}$	GPa	3.40E-02
$E_{22}$	GPa	3.40E-02
$E_{33}$	GPa	1.12E-01
$G_{13}$	GPa	2.00E-02
$G_{23}$	GPa	2.00E-02
$G_{12}$	GPa	1.39E-02
$\nu_{12}$	-	0.22
$\nu_{21}$	-	0.22
$\nu_{13}$	-	0.35
$\nu_{31}$	-	0.11
$\nu_{23}$	-	0.35
$\nu_{32}$	-	0.11
$\rho$	Kg/m <sup>3</sup>	60.00

A different piezoelectric sensor was used for monitoring the sandwich structure, the MFC M2814-P1 by Smart Material Corp. The properties of this component were obtained in the works of Sartorato et al (2015) and are shown at Table 32. This MFC is lighter, thinner and more flexible than the Quick Patch used in the studies for composite-metal bonded joints.

Lastly, the skins were jointed to the core by using the same epoxy resin used for the matrix of the skins. This bond was cured inside a kiln for 8 hours at the temperature of 65 °C, Figure 54 shows the resulting structure. This structure was then carefully cut into 4 specimens of sandwich structure at the defined dimensions.

For the Finite Element model, the glue was simulated linking the skin to the core by using the "tie" algorithm implemented at ABAQUS. Hence, the glue is considered perfect and not deformable.

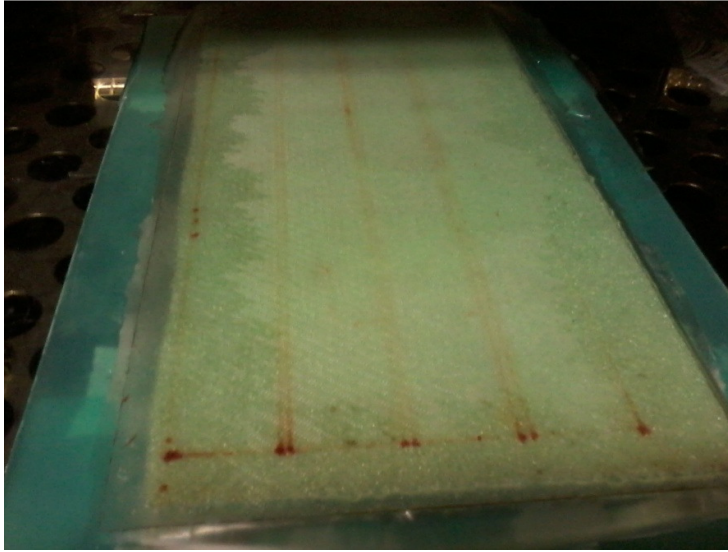


Figure 54. Fabrication Process of the Sandwich Structure

Table 32. Piezoelectric sensor properties (M2814-P1).

Properties	Unit	Value
$c_{11}$	GPa	1.47
$c_{12}$	GPa	1.19
$c_{13}$	GPa	1.22
$c_{33}$	GPa	59.70
$c_{44}$	GPa	23.20
$c_{66}$	GPa	0.28
$e_{13}$	C/m <sup>2</sup>	-0.05
$e_{15}$	C/m <sup>2</sup>	0.17
$e_{33}$	C/m <sup>2</sup>	21.07
$\epsilon_{11}$	nF/m	0.62
$\epsilon_{33}$	nF/m	15.40
$\rho$	Kg/m <sup>3</sup>	5440

The specimens analyzed are identified in accordance to the following code:

- S1: Intact (Undamaged) Condition
- S2: Damaged Condition
- P0: Absence of MFC (Output by Accelerometers: "A1", "A2", "A3")
- P1: Presence of one MFC (Output by: "P1", "A2", "A3")

- P2: Presence of two MFCs (Output by: "P1", "P2", "A3")

#### 4.4.2. EXPERIMENTAL SET-UPS AND INSTRUMENTATION

Since the biclamped condition is considerably more complex to perform experimentally for sandwich structures, the vibration tests were limited to the free-free boundary condition. Thus, the specimens were connected to a metal support via a thin string as shown in Figure 55.



Figure 55. Experimental set-up for the free-free condition of sandwich structures.

The data was acquired by using LMS SCADAS Mobile, which was set to cover a bandwidth of 4096 Hz with 8193 spectral lines. The apparatus was set to compute the mean values out of 5 repetitions to reduce random fluctuations or noise and only data with reasonable high coherence values for the range of interest was used.

Besides the piezoelectric sensor previously mentioned, data acquisition was also performed by using three accelerometers Piezotronics Model 352C22, which had the sensitivities of 9.57 mV/g , 9.31 mV/g and 99.6 mV/g. The input load was performed by using an impulse force Piezotronics hammer Model PCB 0860C3. Figure 56 shows details about the input point and location of accelerometer.

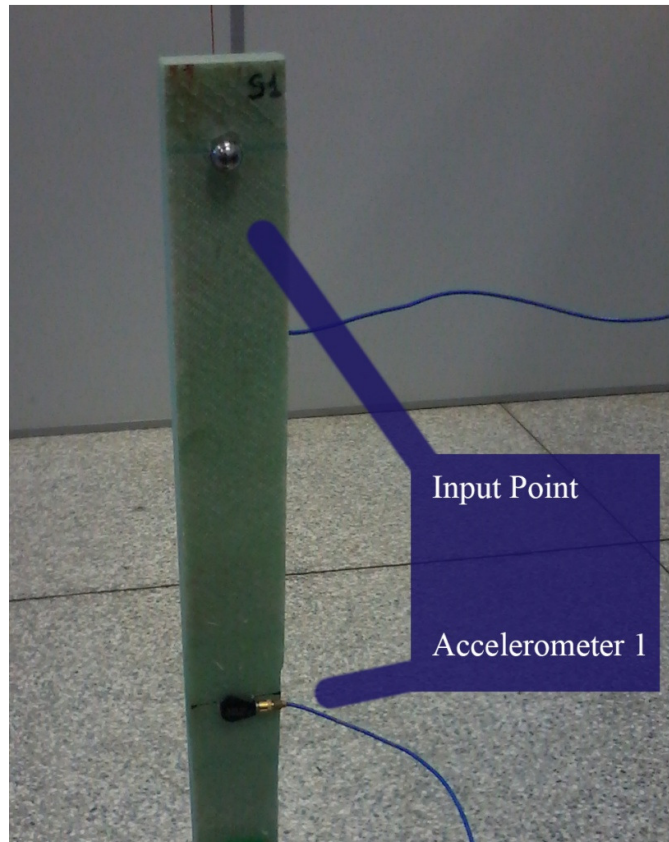


Figure 56. Details of the experimental set-up for free-free condition of sandwich structure: input and output points.

#### 4.4.3. EXPERIMENTAL PROCEDURES

The experimental procedures follow the same method shown earlier. The first analysis compared the dynamic response of the specimens S1P0 and S2P0 in order to verify the influence of the presence of damage in the sandwich structure. The second one compared the dynamic response of the specimens S1P0, S1P1 and S1P2 in order to verify the influence of the presence of the piezoelectric sensor. The third analysis compared the dynamic response of

specimens with MFCs in order to verify the possibility of using their dynamic signature to identify the damage.

#### 4.5. FINITE ELEMENT ANALYSIS

The simulations for the Sandwich structures were also performed in ABAQUS™ v6.12. The skins were modeled by shell elements (S4R), while the core and MFCs sensors were modeled by solid elements.

The core was meshed by C3D8R, which is an 8-node linear brick for 3D stress analyses, and the MFCs were meshed by C3D20RE, which is a 20-node quadratic brick with piezoelectric degrees of freedom.

The bond between the skins and the core was modeled in the same way for the bonded joint, i.e. a perfect bond with no thickness and tie constraint. The damage was defined as simply a region without the tie constraint, allowing the surfaces to separate freely. The boundary condition followed the same process used for the bonded joints. Thus, the free-free condition was simulated by using the engineering feature "spring". Figure 57 shows specimen S2P2 (which contains both the damage and the MFC elements).

The dynamic analyses followed the same procedures used for bonded joints, including the insertion of experimental damping factors in order to improve the numerical models.

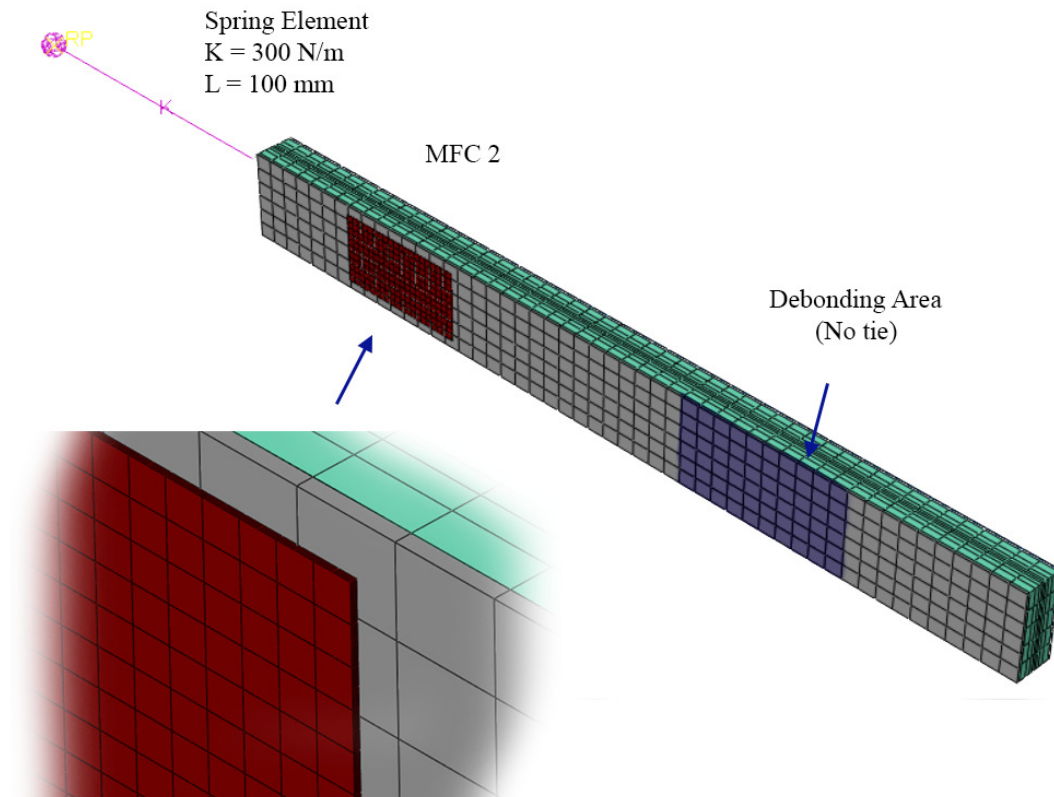


Figure 57. Finite Element model for the sandwich structure S2P2.

## 4.6. RESULTS

After performing the experimental analysis at a frequency range  $[0,4096]$  Hz, it is necessary to define more restricted range, considering the possible limitations of the experimental method used, and the fact that for the purposes of this study, the range of interest needs only to involve the first non-rigid vibration modes of the specimens.

As described in the previously, the FE models had damping calculated experimentally in order to improve their results. The relevant damping factors for this study are presented from Table 33 to Table 38.

Table 33. Critical Damping Factors for S1P0 – Sandwich Structure.

<b>Frequency [Hz]</b>	<b>Critical Damping Factor</b>
699.64	0.00798
1343.91	0.01638
2264.00	0.03083

Table 34. Critical Damping Factors for S1P1 – Sandwich Structure.

<b>Frequency [Hz]</b>	<b>Critical Damping Factor</b>
704.42	0.00703
1338.62	0.01390
2025.52	0.01396

Table 35. Critical Damping Factors for S1P2 – Sandwich Structure.

<b>Frequency [Hz]</b>	<b>Critical Damping Factor</b>
705.94	0.00760
1348.84	0.01306
2046.24	0.01185

Table 36. Critical Damping Factors for S2P0 – Sandwich Structure.

<b>Frequency [Hz]</b>	<b>Critical Damping Factor</b>
683.02	0.00730
1317.94	0.01292
1995.14	0.02161

Table 37. Critical Damping Factors for S2P1 – Sandwich Structure.

<b>Frequency [Hz]</b>	<b>Critical Damping Factor</b>
689.59	0.00759
1309.59	0.01547
1986.76	0.02366

Table 38. Critical Damping Factors for S2P2 – Sandwich Structure.

<b>Frequency [Hz]</b>	<b>Critical Damping Factor</b>
691.34	0.00799
1325.12	0.01502
1997.59	0.01484

The vibration modes for the undamaged specimen and their respective natural frequencies are shown in Figure 58 and Table 39.

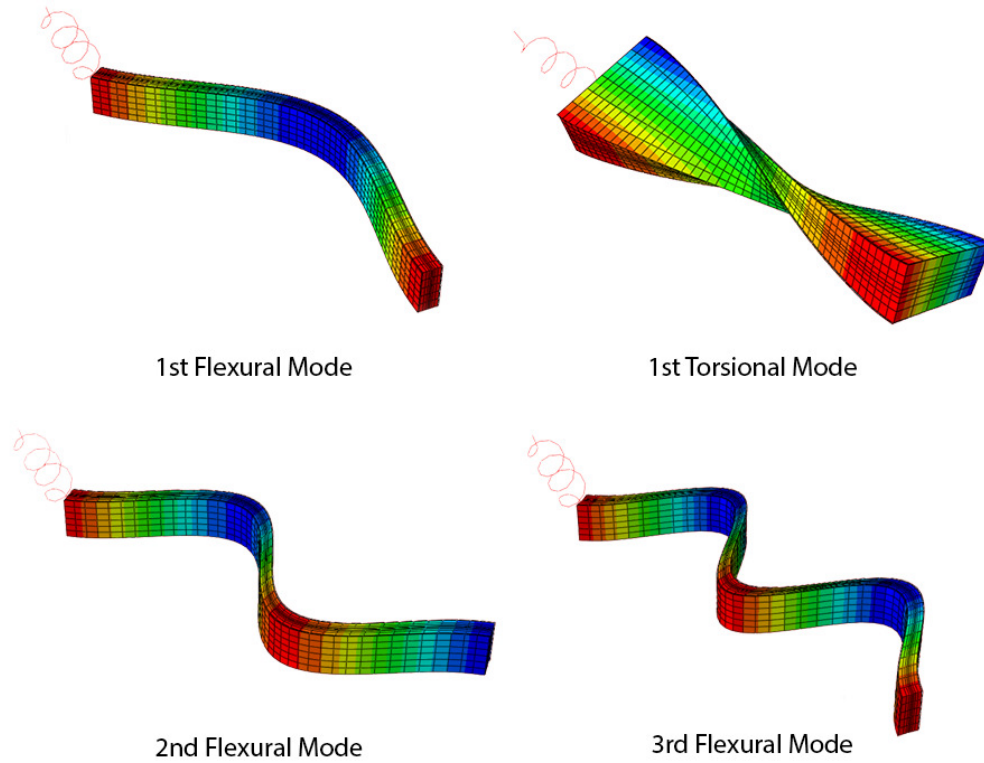


Figure 58. First non-rigid modal shapes for the undamaged sandwich structure.

Table 39. Modal Analysis for Sandwich Structures - Numerical natural frequencies for specimen S1P0.

<b>Mode</b>	<b>Frequency [Hz]</b>
1 <sup>st</sup> Flexural	780.96
1 <sup>st</sup> Torsional	932.15
2 <sup>nd</sup> Flexural	1402.30
3 <sup>rd</sup> Flexural	2042.00

Based on the mode shapes, the frequency range of interest was set from [50, 2300] Hz.

#### 4.6.1. CASE STUDY 1: INFLUENCE OF THE PZT SENSOR

To verify the influence of the PZT sensor in the dynamic behavior of the sandwich structure, the FRF of the permanent accelerometer (Accelerometer 3) was compared to all specimens without damage. In other words, the studied signatures came from specimens S1P0, S1P1 and S1P2. The results are shown in Figures 59 and 60

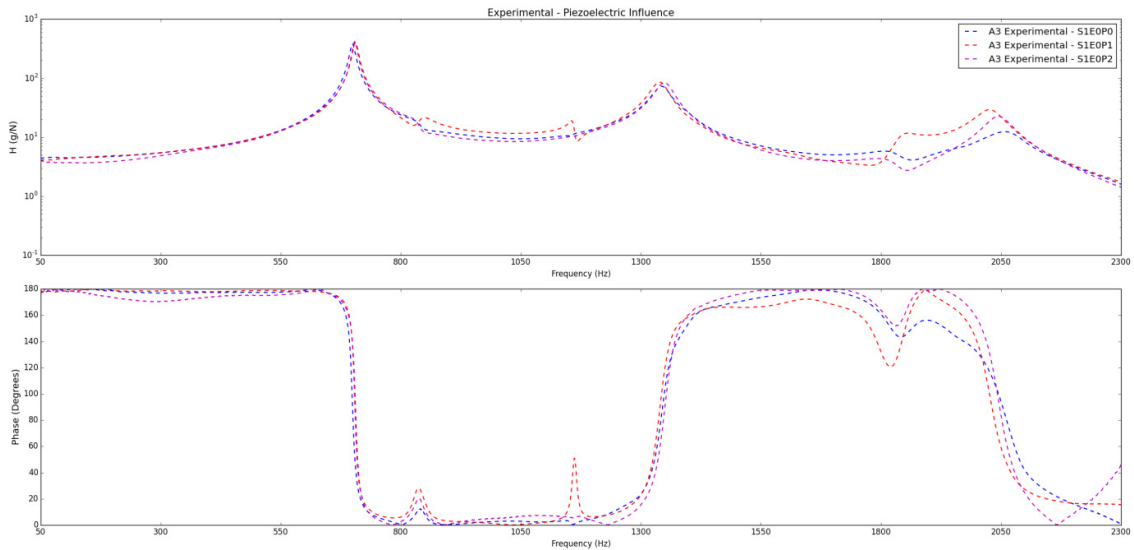


Figure 59. Experimental: Influence of the PZT sensor – Sandwich Structure - A3.

The influence of the MFC on the dynamic behavior of the sandwich structure is minimal as shown by the experimental results. However, the computational analysis provided a much greater influence, which is typical of a strong reduction in the stiffness of the structure.

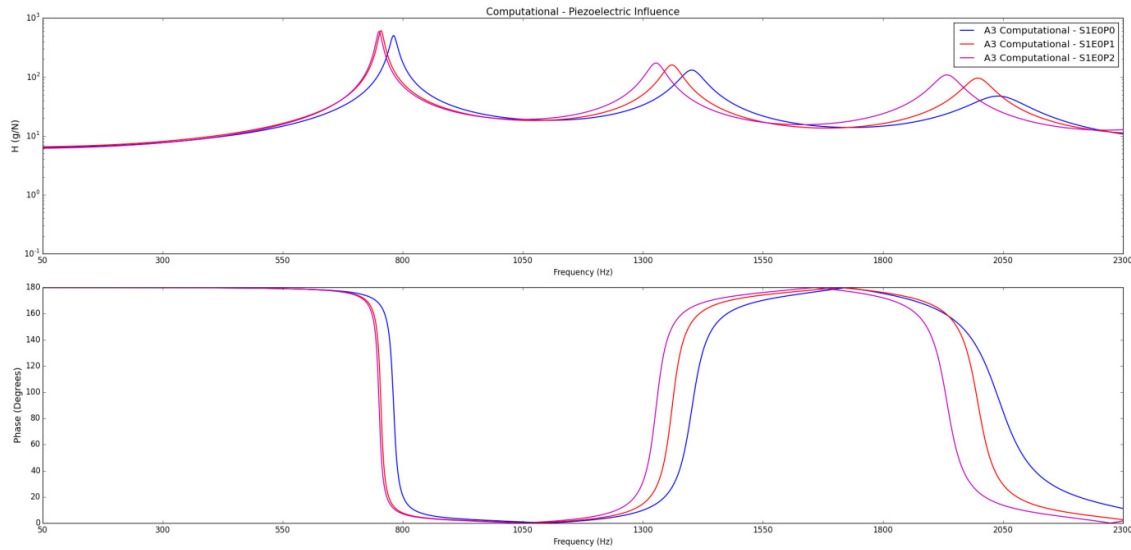


Figure 60. Computational: Influence of the PZT sensor - Sandwich Structure - A3.

By comparing the curves for Specimen S1P2, it can be noticed that the computational analysis is predicting a higher influence of the MFC sensor than the influence obtained experimentally as shown by Figures 61 and 62. Comparing the curves of S1P0, it becomes evident that the computational model displays a higher stiffness than the experimental specimens. One possible explanation is a discrepancy between the mechanical properties of the skins obtained from the literature and the real properties for the specimens used.

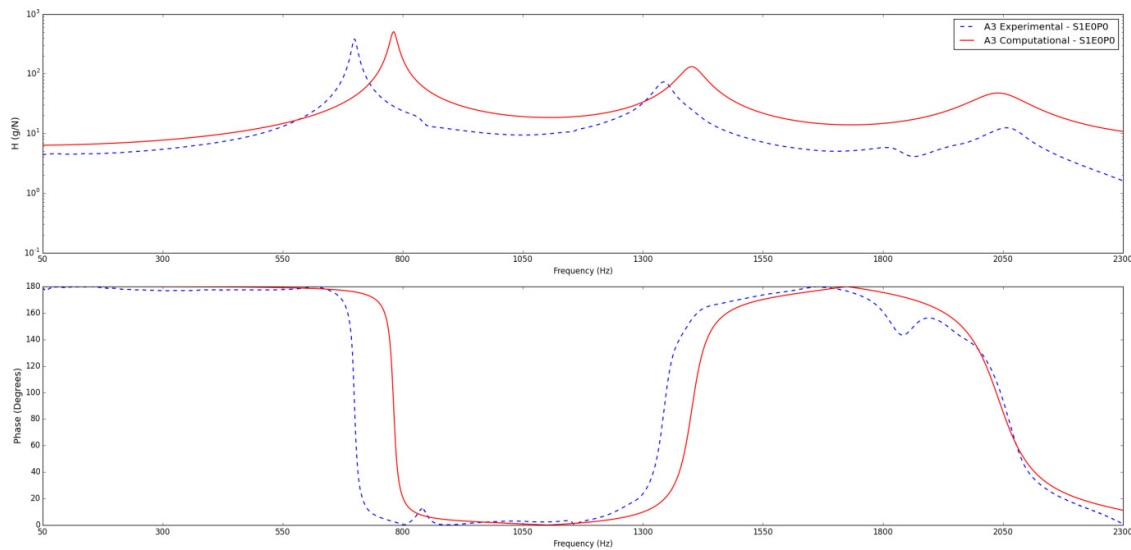


Figure 61. Comparison: Computational vs. Experimental FRF  $H_{14}$  S1P2 (Sandwich Structure).

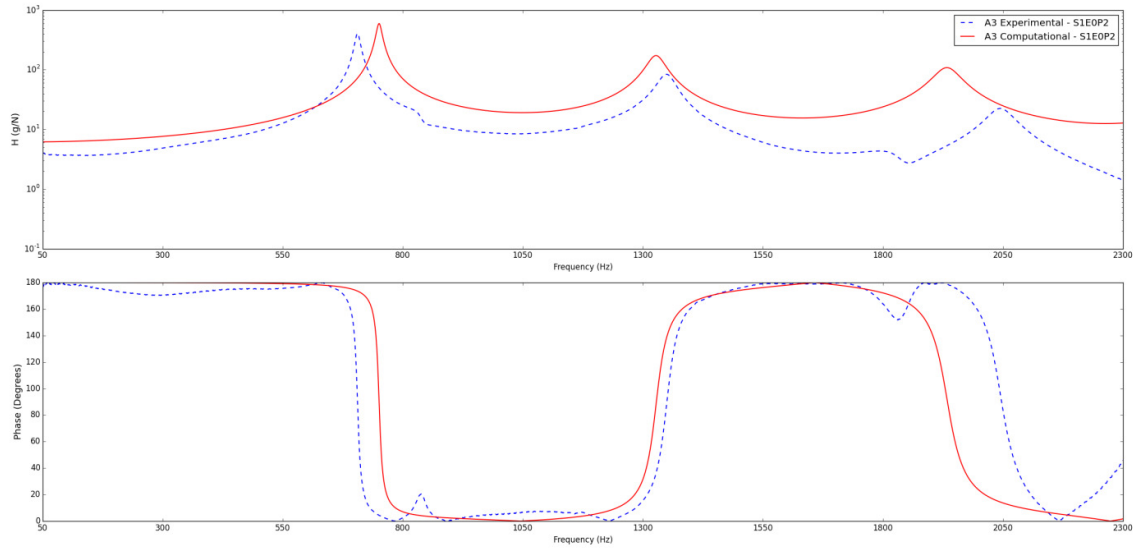


Figure 62. Comparison: Computational vs. Experimental FRF  $H_{14}$  S1P2 (Sandwich Structure).

#### 4.6.2. CASE STUDY 2: INFLUENCE OF THE DAMAGE

The influence of the debonding damage was studied by comparing the FRFs of the accelerometers for the specimens without MFC sensor. As explained previously, the reason for this is to isolate the influence of damage.

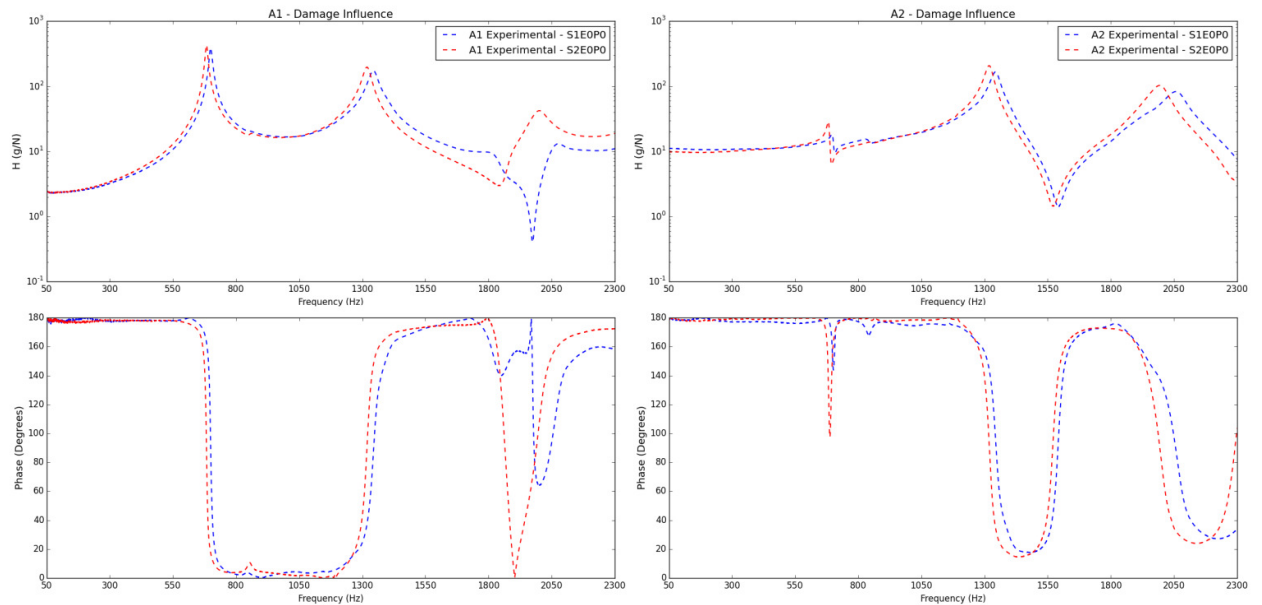


Figure 63. Experimental: Influence of Debonding Damage - Sandwich Structure - A1 and A2.

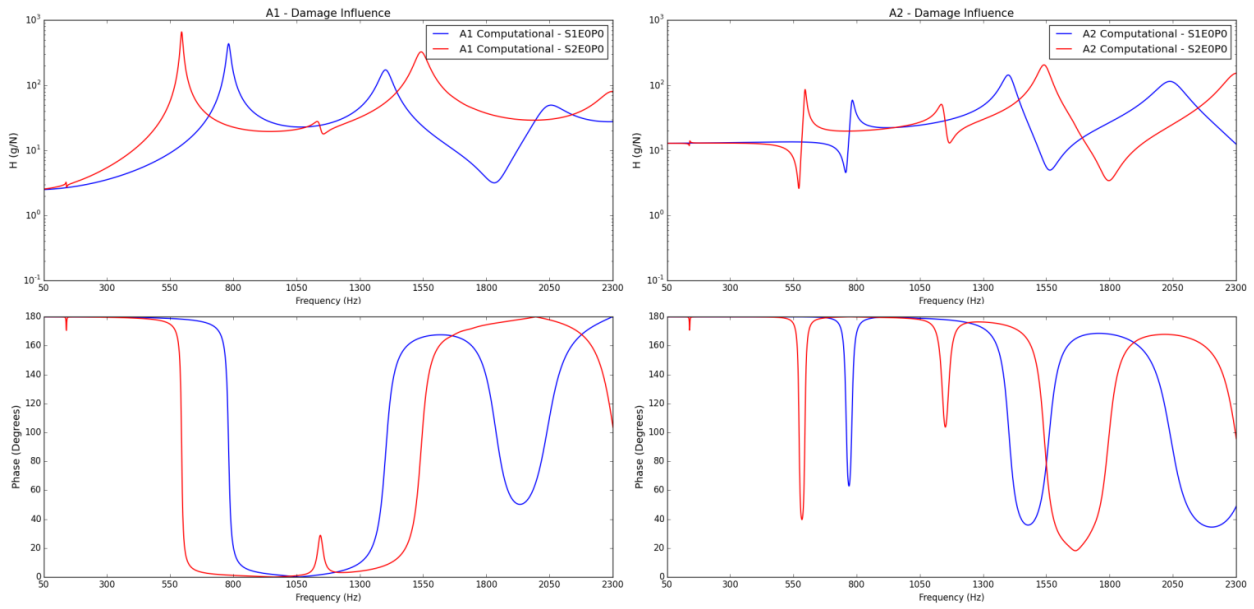


Figure 64. Computational: Influence of Debonding Damage - Sandwich Structure - A1 and A2.

The influence of damage in the FE model is much more relevant compared to experimental results. Possible reasons for this effect are the perfect freedom of displacement, which exists in the debonded area for the FE model. In the experiments, that same region might have resistance to movements, which could have smaller debonding area, because it is very complicated to control the manufacturing process to produce this specific damage.

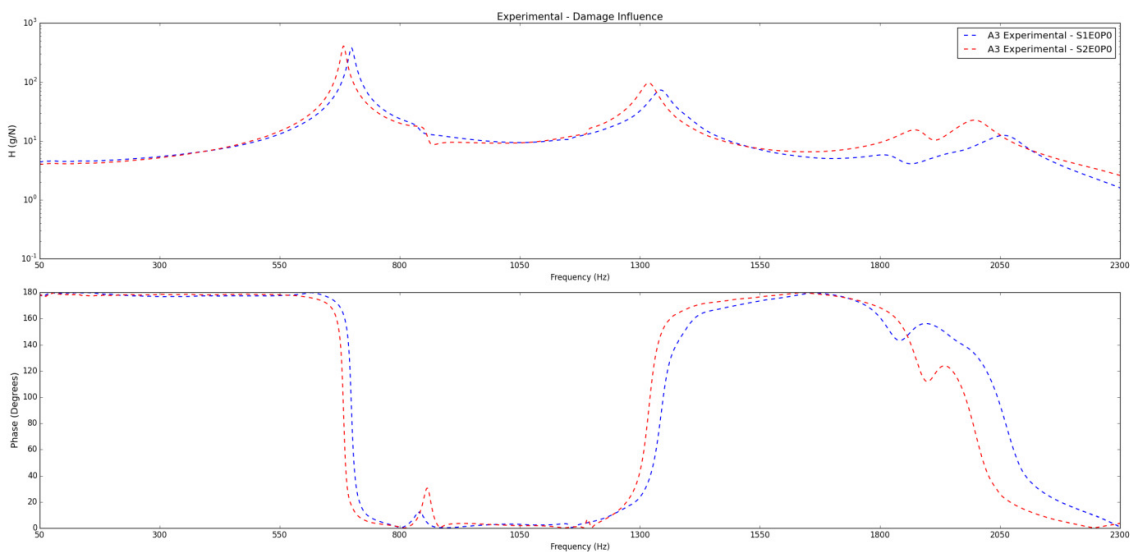


Figure 65. Experimental: Influence of Debonding Damage - Sandwich Structure - A3.

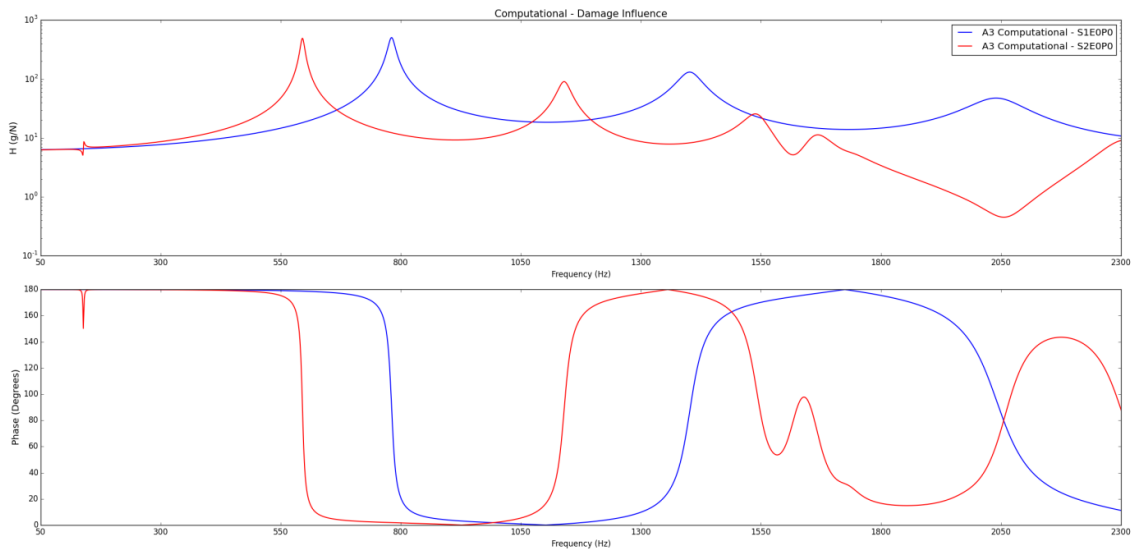


Figure 66. Computational: Influence of Debonding Damage - Sandwich Structure- A3.

#### 4.6.3. CASE STUDY 3: DAMAGE IDENTIFICATION

The damage identification is now performed by two different MFC sensors. The purpose of this case study, as explained in the previous sections, is to use the dynamic signatures in order to observe the shift caused by the presence of damage, followed by the appliance of the damage metrics.

The Frequency Response Functions used for these analyses are shown in Figures 67 and 68.

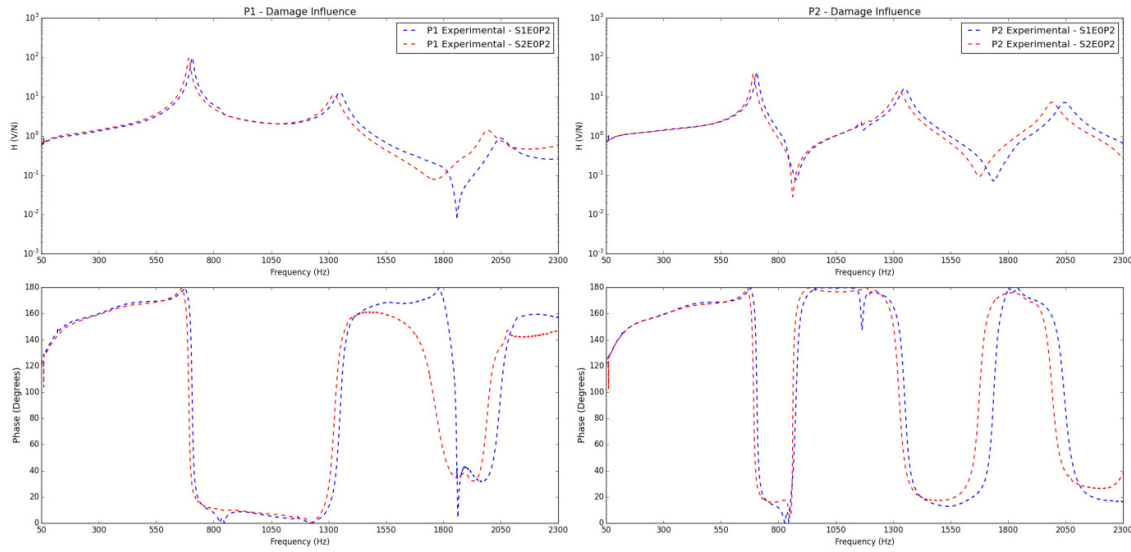


Figure 67. Experimental: Influence of the Damage - Sandwich Structure - P1 and P2.

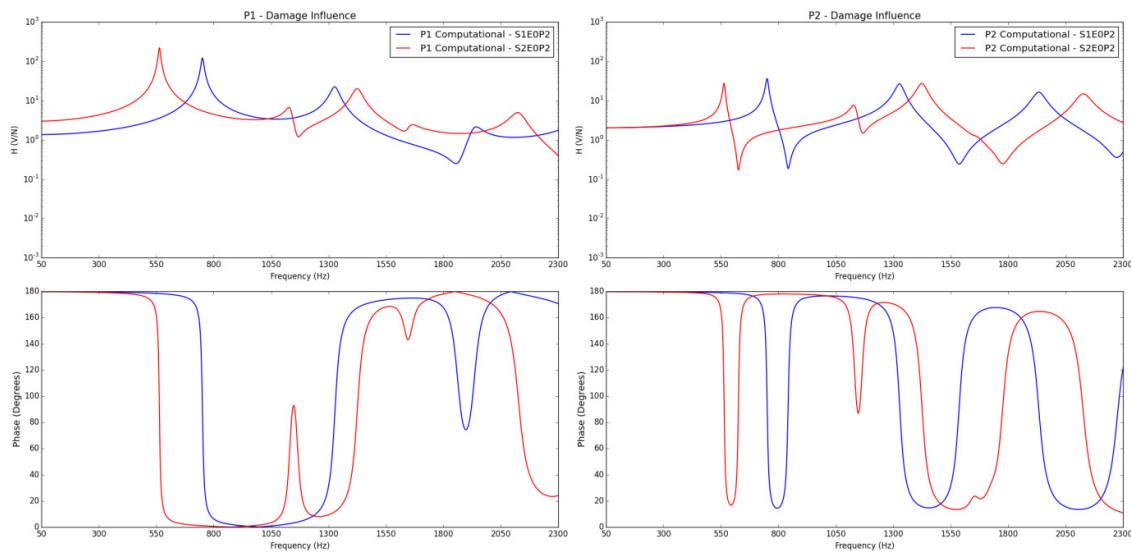


Figure 68. Computational: Influence of the Damage - Sandwich Structure - P1 and P2.

The computational models did not properly represent the damage for the structure. The effect of the damage in the dynamic signature of the computational specimens is much greater than the experimental ones.

Figure 69 shows that in the intact specimens (S1), the dynamic signatures are very similar, where the highest differences are more evident for higher frequencies. However, as

shown by Figure 70, the response of the damaged specimens is very clear even for lower frequencies.

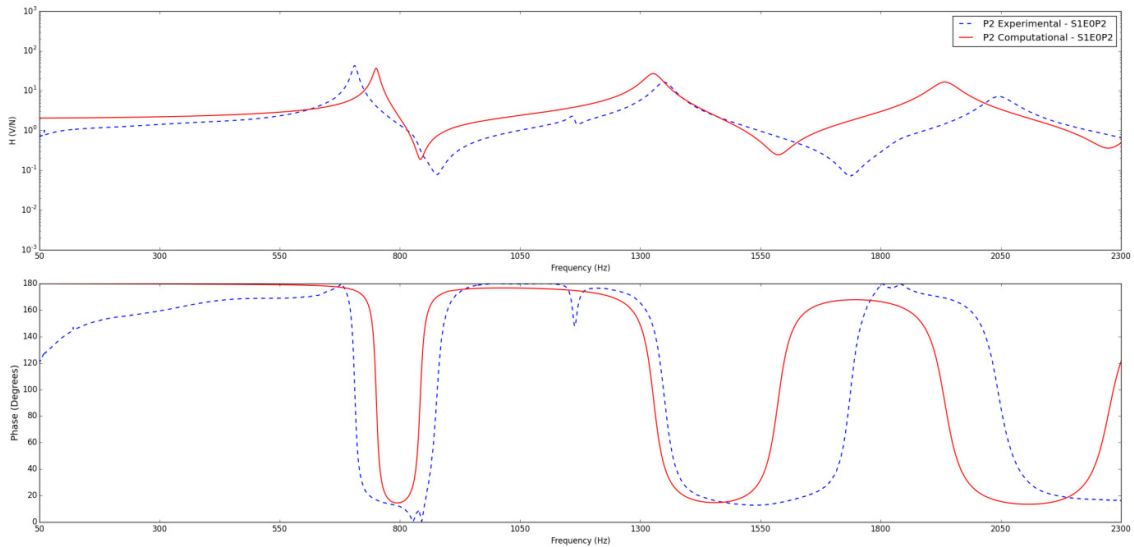


Figure 69. Comparison: Computational vs. Experimental FRF  $H_{13}$  S1P2 (Sandwich Structure).

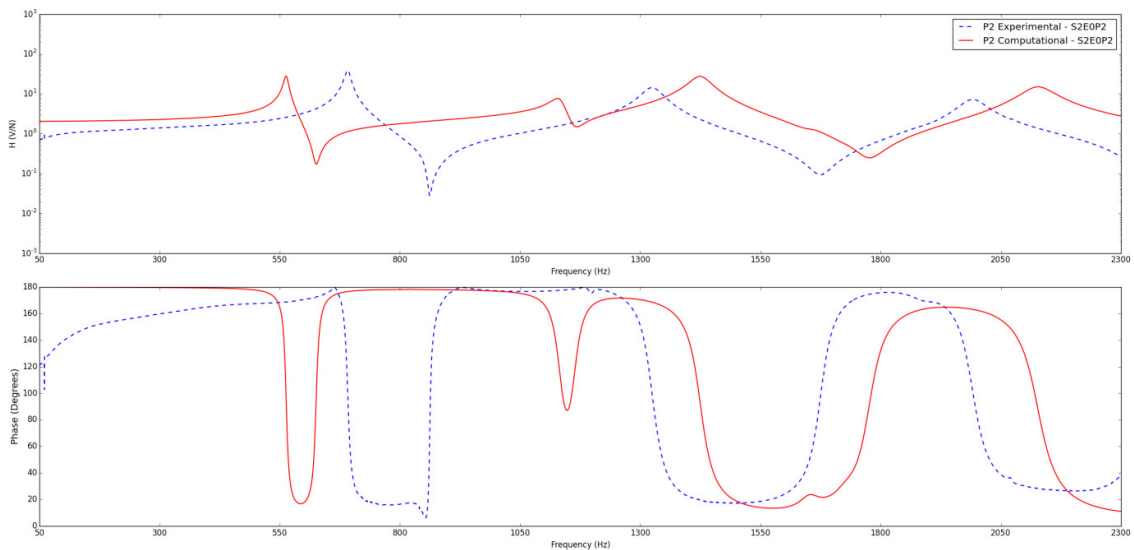


Figure 70. Comparison: Computational vs. Experimental FRF  $H_{13}$  S2P2 (Sandwich Structure).

By applying the metrics of damage quantification previously explained, it is possible to calculate the damage factors for the sandwich structure. The values are presented in Tables 40 and 41.

Table 40. Mickens Damage Factors for the Sandwich Structure.

<i>Computational Model</i>	<b>No MFCs</b>		<b>1 MFC</b>		<b>2 MFCs</b>	
	<b>DF(Amp)</b>	<b>DF(Phase)</b>	<b>DF(Amp)</b>	<b>DF(Phase)</b>	<b>DF(Amp)</b>	<b>DF(Phase)</b>
H <sub>12</sub>	2.41	1.75	1.99	0.73	0.86	8.30
H <sub>13</sub>	1.66	0.59	0.87	9.24	2.01	1.58
H <sub>14</sub>	0.88	12.72	2.2	11.71	1.78	1.35
<i>Experiments</i>						
H <sub>12</sub>	1.41	0.76	0.20	0.11	0.44	0.79
H <sub>13</sub>	0.25	0.14	0.26	0.65	0.66	0.65
H <sub>14</sub>	0.35	0.46	0.47	0.52	0.39	0.36

Table 41. Modified Damage Factors for the Sandwich Structure.

<i>Computational Model</i>	<b>No MFCs</b>		<b>1 MFC</b>		<b>2 MFCs</b>	
	<b>DF(Amp)</b>	<b>DF(Phase)</b>	<b>DF(Amp)</b>	<b>DF(Phase)</b>	<b>DF(Amp)</b>	<b>DF(Phase)</b>
H <sub>12</sub>	0.27	0.25	0.31	0.24	0.30	0.41
H <sub>13</sub>	0.34	0.25	0.31	0.46	0.26	0.27
H <sub>14</sub>	0.30	0.47	0.25	0.32	0.32	0.34
<i>Experiments</i>						
H <sub>12</sub>	0.12	0.10	0.09	0.08	0.08	0.10
H <sub>13</sub>	0.10	0.11	0.08	0.10	0.06	0.11
H <sub>14</sub>	0.09	0.09	0.07	0.12	0.10	0.11

For the modified Metric, the damage factor obtained experimentally by the MFC 1 and MFC 2 were respectively 0.08 and 0.06 when based on the Magnitude. And, the damage factor obtained by A3 for a specimen without MFC sensor was of 0.09.

The worst discrepancy of damage factor calculation happens for the computational analysis when using phase-based method with the MFC 1, which provides a damage factor of 0.41. And, the accelerometer 3 shows a damage factor of 0.30.

For the original metric, the experimental analysis based on Magnitude, the MFC sensors provide a value of 0.44 and 0.66. And, the Accelerometer 3 provides a damage factor of 0.35.

Overall the values were satisfactory, but the damage factors of the computational model became much greater than the experimental ones due to the higher effect of the

debonding damage in the FRFs of the computational data, as well as the influence of the material properties of the skins used in the FE model.

#### 4.7. CONSIDERATIONS

The metrics showed to be effective even for the free-free sandwich structure case. The use of MFC sensor response still represented a similar damage factor to those of the reference accelerometers.

The discrepancy between the computational and the experimental results can be from either problem during the manufacturing process to produce the damage (debonding area) or due to the material properties of the skins used in the computational model. Moreover, the computational models should be certainly improved for future studies, considering not only material properties from characterization tests for all elements (skins, MFC sensor and core, including viscoelastic properties), but also other finite element formulations.



## 5. CONCLUSION AND FUTURE PERSPECTIVES

---

---

The present research focused on a specific field, which consist on application of vibration based methods for monitoring debonding damage in metal-composite bonded joints and sandwich structures. In general, numerical and experimental results can be considered satisfactory, giving relevant contributions for the field pointed above. Moreover, damage metrics presented by the literature were also improved in the present work, providing better results than the previous ones.

The progress reached different extends for both structures, which are divided into its specific subsections.

### 5.1. METAL-COMPOSITE BONDED JOINT

For metal-composite bonded joints, it has been observed that even considering the large extension of the damage (high severity of the damage) used in the experiments, 50% of debonding in the joint area, the influence on the Frequency Response Functions is considerably low. This justifies the need to focus on damage quantification metrics. Therefore, two metrics of damage identification were investigated, and those can be considered reliable for this task. However, the damage metrics have shown more stable results after applying the filter proposed in the present work.

As shown in this Master's Dissertation, the damage may heavily influence one peak of the FRF without changing the other ones. Thus, when this phenomenon happens, the metrics dilute the effect of the damage, and result in small damage factors. Therefore, it is also important to achieve methods to successfully narrow the range of frequencies, which are under study to improve the identification of the damage.

Lastly, it is suggested that future studies focus on further testing of damage metrics by analyzing specimens with different severity of damage, including two different "undamaged specimens" to properly observe cases of possible false identification of damage.

## 5.2. SANDWICH STRUCTURE

For the computational models of the sandwich structures, debonding damage had stronger effect on the dynamic response compared to the experimental analyses. This could be related either to the mechanical properties assumed to the composite skins of sandwich structures or to an overestimation of the severity of damage in the finite element model compared to the real debonding extension in the sandwich structure.

Since the computational representation of the damage used for the sandwich was the same used for the bonded joints, it is reasonable to conclude that some discrepancies between computational and experimental results can be also related to the manufacturing process effects like the gluing process of the skins to the core.

## 6. REFERENCES

---

---

- AMIR, S., MORLIER, J., GOURINAT, Y., **Damage monitoring in sandwich beams by modal parameter shifts: A comparative study of burst random and sine dwell vibration testing.** Journal of Sound and Vibration 329, no. 5, pp. 566-584, 2010.
- BIRMANI, V., SIMONYAN, A., **Theory and applications of cylindrical sandwich shells with piezoelectric sensors and actuators.** Smart Materials and Structures 3(4), 391, 1994.
- BORGES, E.N, 2012, **Fabricação, Análise Experimental e Computacional de Juntas Híbridas Coladas Monitoradas por Compósitos Inteligentes.** Dissertação de Mestrado - Escola de Engenharia de São Carlos, Universidade de São Paulo, Programa de Pós-Graduação em Engenharia Mecânica, 168p, 2012.
- CALIRI, M.F., **Modelos de material para espumas poliméricas aplicadas a estruturas aeronáuticas em material compósito sanduíche.** Dissertação de Mestrado - Escola de Engenharia de São Carlos, Universidade de São Paulo, São Carlos, 2010.
- CALLISTER, W. D. **Ciencia e Engenharia de Materiais: Uma Introdução.** Rio de Janeiro: Livros Técnicos e Científicos, 2002.
- CHIU, W.K., GALEA, S.C., KOSS, L.L., AND RAJIC, N., **Damage detection in bonded repairs using piezoceramic,** Smart Mater. Struct 9, pp 466-475, 2000.
- DAWOOD, T. A., SHENOI, R.A., VERES, S.M., SAHIN, M., GUNNING, M.J., **Damage detection in a sandwich composite beam using wavelet transforms.** In: SMITH, R. C. (Ed.). Smart Structures and Materials 2003: Modeling, Signal Processing, and Control. Bellingham: Spie-Int Soc Optical Engineering, v.5049,. p.706-717, 2003.
- DHAMANDE, L. S., BHASKAR, R. V., **Damage Detection in Aluminium Honeycomb Structure using Vibration Analysis.** International Journal of Current Engineering and Technology, v.5 n.5. 2014.
- EWINS, D.J., **Modal Testing: Theory, Practice and Applications.** Research Studies Press, Baldock, Hertfordshire, England 2000.

- GUYOTT CCH, CAWLEY P, ADAMS RD, **The Nondestructive Testing Of Adhesively Bonded Structure - A Review**, Journal Of Adhesion, v.20, ISSN:0021-8464, P.129-159, 1986.
- HAFIYCHUK, V., LUCHINSKY, D. G., SMELYANSKIY, V. N., **Comparisons of SHM Sensor Models with Empirical Test Data for Sandwich Composite Structures**. Lancaster: Deustech Publications, 2011.
- HALL S.R., **The Effective Management and Use of Structural Health Data**. Proceedings of the 2nd International Workshop on Structural Health Monitoring, 265-275, 1999.
- HAMLEY C.S., LESTARI W., QIAO P, ET AL., **Experimental damage identification of carbon/epoxy composite beams using curvature mode shapes**. Struct Health Monit; 3(4): 333-353, 2004.
- HIGGINS, A., **Adhesive Bonding Aircraft Structures**, International Journal of Adhesion and Adhesives, v. 20, n.5, p. 367-376, 2000.
- LESTARI, W., QIAO, P., **Damage detection of fiber-reinforced polymer honeycomb sandwich beams**. Composite Structures, v. 67, n. 3, p. 365-373, 2005.
- LUCHINSKY, G. et al. **High-fidelity modeling for health monitoring in honeycomb sandwich structures**. In: Aerospace Conference, IEEE. p. 1-7, 2011.
- MASMOUDI, S., EL MAHI, A., EL GUERJOUA, R., **Mechanical behaviour and health monitoring by acoustic emission of sandwich composite integrated by piezoelectric implant**. Composites Part B: Engineering, v. 67, p. 76-83, 2014.
- MEDEIROS, R., RIBEIRO, BORGES, E. N., CARVALHO, F.G., TITA, V. **Vibration-based structural monitoring applied on hybrid bonded joints**, Proceedings of 22nd Brazilian Congress of Mechanical Engineering – COBEM, Ribeirão Preto, Brazil, 2013a.
- MEDEIROS, R., RIBEIRO, M.L., BORGES, E.N. AND TITA, V., **Computational and experimental dynamic analyses of hybrid bonded joints monitored through smart composites**. In: 17th International Conference on Composite Structures – ICCS17, Porto, Portugal, .2013b.

- MEDEIROS, R., Sartorato, M., Marques, F.D., Vandepitte, D. and Tita, V. **Vibration-Based damage identification applied for composite plate: Experimental analyses**. In: 22nd International Congress of Mechanical Engineering – COBEM, Ribeirão Preto, Brazil, 2013c.
- MEDEIROS, R. ; RODRIGUEZ-RAMOS, R. ; GUINOVART-DIAZ, R. ; BRAVO-CASTILLERO, J. ; OTERO, J. A. ; TITA, V. ., **Numerical and analytical analyses for active fiber composite piezoelectric composite materials**. Journal of Intelligent Material Systems and Structures (Print), v. 25, p. 1-18, 2014a.
- MEDEIROS, R., FLOR, F.R., RIBEIRO, M.L., TITA., **Debonding Damage Identification In Metal-Composite Bonded Joint Using Vibration Testing** In: Congresso Nacional de Engenharia Mecânica - CONEM. São Paulo, Brasil, 2014b.
- MENDONÇA, P. T. R. **Materiais Compostos & Estruturas-Sanduiche: projeto e análise**. Barueri, SP: Manole, 2005.
- MICKENS, T., SCHULZ, M., SUNDARESAN, M., GHOSHAL, A., NASER, A. AND REICHMEIDER, R., **Structural health monitoring of an aircraft joint**. Mechanical Systems and Signal Processing, v. 17, No. 2, pp. 285 – 303, 2003.
- MIL-HDBK-5, **Metallic Materials and Elements for Aerospace Vehicle Structures**. Department of Defense, [S.l.]:[s.n.], 2003.
- ORUGANTI, K., M. MEHDIZADEH, S. JOHN, AND I. HERSZBERG., **Vibration-based Analysis of Damage in Composites**. In The 2nd Asia-Pacific Workshop on Structural health Monitoring (2APWSHM), edited by S. Galea, W. Chiu, and A. Mita. Institute of Materials Engineering, 2009.
- PANDEY, A. K., M. BISWAS, AND M. M. SAMMAN, **Damage detection from changes in curvature mode shapes**. Journal of sound and vibration 145, no. 2: 321-332, 1991.
- RAO, SINGIRESU S., FOOK FAH YAP. **Mechanical Vibrations**. Vol. 4. New York: Addison-Wesley, 1995.
- QING, XINLIN P. ET AL., **Effect of adhesive on the performance of piezoelectric elements used to monitor structural health**. International Journal of Adhesion and Adhesives, v. 26, n. 8, p. 622-628, 2006.

- QUAEGEBEUR, MICHEAU, P. MASSON, P., BELANGER, H., **Structural health monitoring of bonded composite joints using piezoceramics**. In: Proceedings of the International Workshop Smart Materials, Structures & NDT in Aerospace-CANSMART. Quebec, Canada, 2011.
- SARTORATO, M., **Desenvolvimento de um Elemento Finito para Análise de Compósitos Inteligentes: Formulação, Implementação e Avaliação**. 2013, 149p. Dissertação (mestrado) – Escola de Engenharia de São Carlos, Universidade de São Paulo, Programa de Pós-Graduação em Engenharia Mecânica, 149p, 2013a.
- SARTORATO, M., Marques, F.D., Vandepitte, D. and Tita, V. **Vibration-Based damage identification applied for composite plate: Numerical analyses**. In: 22nd International Congress of Mechanical Engineering – COBEM, Ribeirão Preto, Brazil, 2013b.
- SARTORATO, M., TITA, V., **A non-linear finite element for curved active composites with embedded piezoelectric layers**. In: 2ND Brazilian Conference on Composite Materials - BCCM 2. São José dos Campos, Brazil, 2014.
- SARTORATO, M., MEDEIROS, R., TITA, V. **A finite element formulation for smart piezoelectric composite shells: Mathematical formulation, computational analysis and experimental evaluation**. Composite Structures, v. 127, p. 185-198, 2015.
- SINGH, C.V. AND TALREJA, R., **Evolution of ply cracks in multidirectional composite laminates**. International Journal of solids and structures, v. 47. pp. 1338-1349, 2010.
- TITA, V. **Projeto e fabricação de estruturas em material composto polimérico**. Sao Carlos: EDUSP, 2006.
- VANTOMME, J., **Evaluation of structural joints in composites with modal parameters**, Composite Structures v. 22 no 4 pp 201–205, 1992.
- ZAGRAI, A., DOYLE, D., AND ARRITT, B., **Sensors and Smart Structures Technologies for Civil, Mechanical, and Aerospace Systems**, vol. 6932 of Proceedings of SPIE, San Diego, United States, March 9-13, 2008.

## 7. ATTACHMENTS

---

---

### 7.1. ATTACHMENT 1 - RELATED PUBLICATIONS

- ☑ MEDEIROS, R., FLOR, F.R., RIBEIRO, M.L., TITA. **Damage quantification in composite cylinders using a computational and experimental technique** In: CONGRESSO NACIONAL DE ENGENHARIA MECÂNICA - CONEM 2014, Uberlândia, São Paulo, Brasil, 2014.
- ☑ MEDEIROS, R., FLOR, F.R., RIBEIRO, M.L., TITA. **Debonding damage identification in metal-composite bonded joint using vibration testing** In: CONGRESSO NACIONAL DE ENGENHARIA MECÂNICA - CONEM 2014, Uberlândia, São Paulo, Brasil, 2014.
- ☑ FLOR, F.R. ; MEDEIROS, R; TITA, V. **Numerical and experimental damage identification in metal-composite bonded joints**. In: 2ª Conferência Luso-Brasileira de Adesão e Adesivos (CLBA 2014), Porto, Portugal, 2014.
- ☑ FLOR, F.R.; MEDEIROS, R; TITA, V. **Numerical and experimental damage identification in metal-composite bonded joints**. The Journal of Adhesion, v.91, p.863–882, 2015.

## 7.2. ATTACHMENT 2 - PYTHON CODE OF THE METRICS

```

def damageQ(property, element, Datas, rangef,altMetric = True):
"""
property: Can either be "Magnitude" or "Phase"
element: Refers to what output element is being used. For example: "A1"
Datas: Is the base variable for the python code I use. It's a dictionary that holds all the raw
datas. For example.
    Data["S1P0X"]["A1"]["Real"] returns a vector with all the real components of the
experimental data received from A1 at the specimen S1P0.
"""
    Intact_a, Damaged_a = Datas[0][element], Datas[1][element]

    i_i, i_f = getIndex(rangef[0], Intact_a['Frequency']), \
        getIndex(rangef[1], Intact_a['Frequency'])

    d_i, d_f = getIndex(rangef[0], Damaged_a['Frequency']), \
        getIndex(rangef[1], Damaged_a['Frequency'])

    i_df = Intact_a['Frequency'][5] - Intact_a['Frequency'][4]
    d_df = Damaged_a['Frequency'][5] - Damaged_a['Frequency'][4]

    # Now the program will make sure both vectors will have the same resolution via linear
interpolation

    k = 0
    Intact_b = {'Frequency': [], property: []}
    Damaged_b = {'Frequency': [], property: []}

    if i_df <= d_df: # Intact has better resolution
        delta_f = i_df
        while True:
            f = Intact_a['Frequency'][i_i + k]
            if f > rangef[1]:
                break
            Intact_b['Frequency'].append(f)
            Damaged_b['Frequency'].append(f)
            Intact_b[property].append(Intact_a[property][i_i + k])
            Damaged_b[property].append(interpValue(f,                    Damaged_a['Frequency'],
Damaged_a[property]))
            k += 1
    else:
        delta_f = d_df
        while True:
            f = Damaged_a['Frequency'][d_i + k]
            if f > rangef[1]:
                break

```

```
    Intact_b['Frequency'].append(f)
    Damaged_b['Frequency'].append(f)
    Damaged_b[property].append(Damaged_a[property][d_i + k])
    Intact_b[property].append(interpValue(f, Intact_a['Frequency'], Intact_a[property]))
    k += 1

if altMetric:
    cut_i, cut_d = getCut(Intact_b[property]), getCut(Damaged_b[property])

y = {"Frequency": [], "Damage": []}
Total_y = 0
for i in range(len(Intact_b['Frequency'])):
    pi = Intact_b[property][i]
    pd = Damaged_b[property][i]
    try:
        if altMetric:
            dy = abs((pi - pd) / max(pi,pd)) * (delta_f / (rangef[1] - rangef[0]))
            if pi < cut_i and pd < cut_d:
                dy = 0

        else:
            dy = abs((pi - pd) / pi) * (delta_f / (rangef[1] - rangef[0]))
    except ZeroDivisionError:
        dy = 0
    y["Frequency"].append(Intact_b['Frequency'][i])
    y["Damage"].append(dy)

    Total_y += dy

D = Total_y
return D, Intact_b['Frequency'], y

def getCut(vy,cut = 75, max_dif = 15):
    """
    getCut will return the value on the vy vector which is greater only to cut% of the total
    number elements
    in the vector
    :param vy: Vector for the y axis
    :param cut: % of cut.
    :return:
    """
    while True:
        temp = copy.copy(vy)
        temp.sort()

        i = int(len(temp)*cut/100)

        while abs(temp[i])/abs(temp[-1])*100 > max_dif and i>1:
            i = i-1
        return temp[i]
```

### 7.3 ATTACHMENT 3 – ELASTOMER INFLUENCE

A brief study was performed using elastomeric patches (25 x 12 mm) attached at different orientations on the skin of the undamaged sandwich structure in order to observe their influence in the dynamic behavior of these structures. The elastomeric patches were done using double-sided bonding tapes at fixed positions as shown in Figure 71.

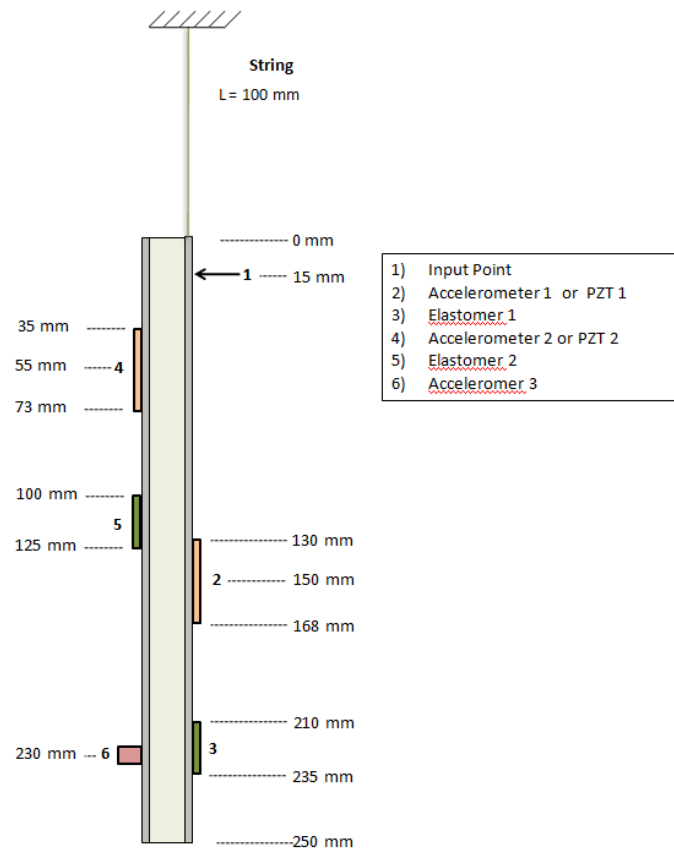


Figure 71. Test set-up of undamaged sandwich structure including elastomeric patches.

A total of five different setups were studied using different orientation of elastomeric patches. The relation between the adopted orientation and the Specimen ID is shown at Table 42.

Table 42. Specimen ID considering the orientation of elastomeric patch.

Specimen ID	Orientation
S#E0P#	No Elastometers
S#E1P#	E1 at 0°; E2 at 0°
S#E2P#	E1 at 0°; E2 at +45°
S#E3P#	E1 at -45°; E2 at 0°
S#E4P#	E1 at -45°; E2 at +45°

This investigation was only a preliminary study. The obtained results show that the elastomeric patches used had low influence on the dynamic behavior of the sandwich structure. This observation is confirmed by Figures 72 to 74.

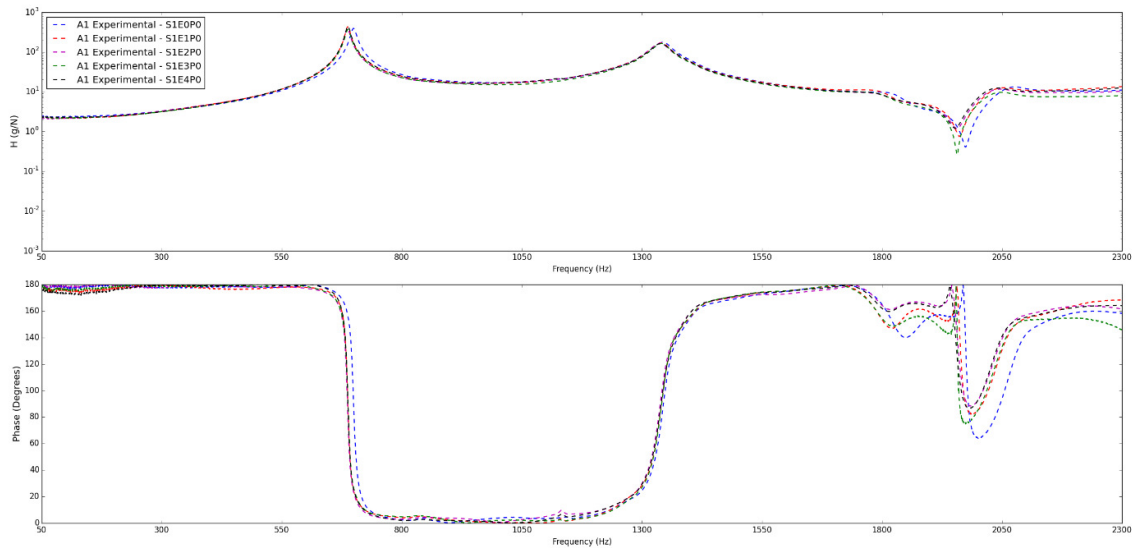


Figure 72. Elastomeric patches influence – measurements by Accelerometer 1 (Specimen S1P0).

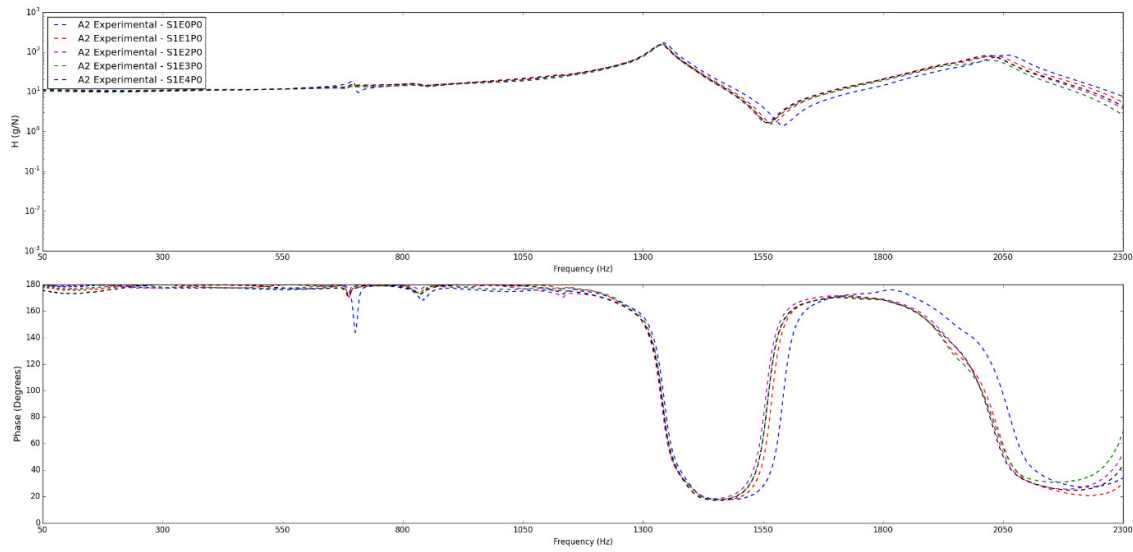


Figure 73. Elastomeric patches influence – measurements by Accelerometer 2 (Specimen S1P0).

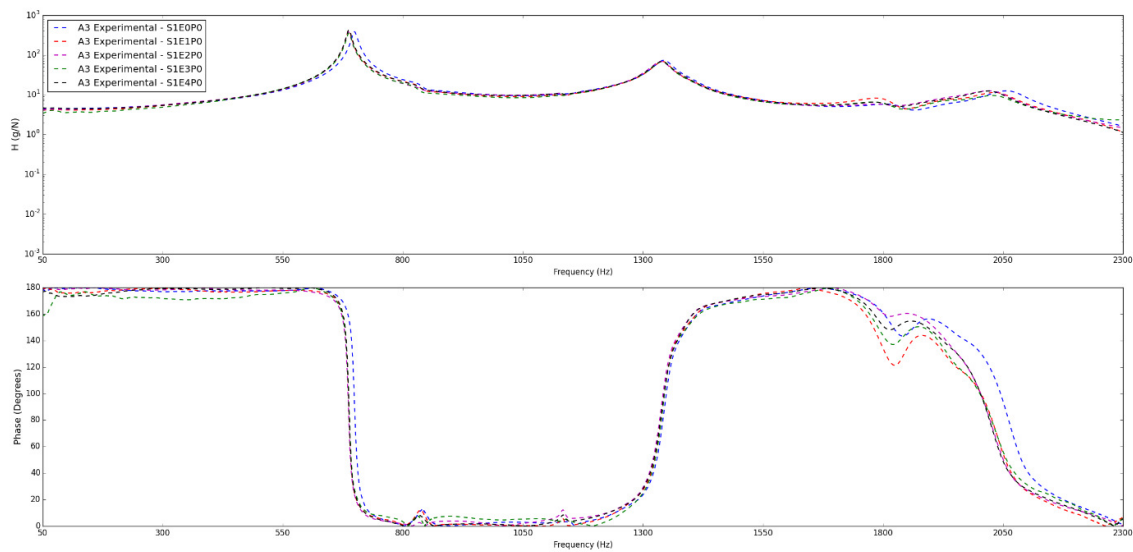


Figure 74. Elastomeric patches influence – measurements by Accelerometer 3 (Specimen S1P0).

Lastly, for future analysis, it is suggested to use stiffer elastomers in order to observe the influence of these elements in the dynamic behavior of the sandwich structures. In addition, it is strongly recommended to develop finite element models to investigate via computational analyses which parameters related to the elastomeric patches can more influence the dynamic response of the sandwich structures.